POLITECNICO DI TORINO

Master's degree in

Aerospace Engineering

Enhancing Active Flow Control Strategies for Delaying 2D Boundary Layer Transition

Supervisor:
Dr. **Jacopo Serpieri**

Candidate:
Li Causi Gaspare

Academic year 2023/2024

Contents

List of Figures

List of Tables

Abstract

Through research studies conducted over the years, it has been demonstrated that suction is an active flow control (AFC) technique that is highly effective in delaying the transition from laminar to turbulent flow.

This thesis focuses on utilizing a numerical framework to determine the optimal suction configuration, intending to maximize the extension of the laminar region within a steady, incompressible, and two-dimensional flat plate boundary layer.The computational approach involves integrating the boundary layer equations using an internally developed code (BLES), with suction effects introduced through the wall boundary condition. Validation is conducted by comparing BLES computed velocity field with the Blasius and openFOAM solutions. Linear Stability theory is used to asses the modal and local stability of the boundary layer flow. The Companion Matrix Method is used to solve the Orr-Sommerfeld equation and obtain the spatial evolution of the perturbation modes [5], while the e^N method is employed for transition modeling [35].

In order to maximize the tranisition delay, an optimization of the flow control parameters (suction strength and location) was carried out by means of the Bayesian optimization approach. The effect of suction configuration is evaluated both versus the transition position and the evolution of the skin friction coefficient over the flat plate. Results indicate a narrow range of optimal mass flow conducive to effective and efficient transition control, with the optimal suction region extention (d) ranging from 8% and 20% of the plate total length. Moreover, the location of the suction region significantly influences transition. It is shown that shifting the suction location, while fixing the mass flow, results in a displacement of transition.

A clear relationship between suction configuration and transition position was found. From this, a predictive AFC model is proposed. The output of the proposed model, tested against the results of the BLES-LST framework, agree within 1% accuracy. Further experimental validation of the derived observations is sought after. Towards this goal a wind tunnel model was designed and the experimental tests are planned.

Finally, future development of the optimization framework could include a non uniform suction velocity profile.

Chapter 1

Introduction

In an era marked by unprecedented connectivity and interdependence, the phenomenon of globalization has reshaped virtually every aspect of human society. From the flow of goods and services to the exchange of ideas and cultures, globalization has fostered a level of interconnectedness that transcends geographical boundaries and revolutionizes the way we perceive the world. Central to this transformative process is the phenomenon of air travel, which serves as a vital conduit for facilitating the exchange of people, goods, and ideas across vast distances.

As globalization continues to accelerate, so too does the demand for air transportation, resulting in a dramatic surge in air traffic volume worldwide. While this exponential growth in air travel has undoubtedly facilitated economic development, cultural exchange, and tourism, it has also raised significant concerns regarding its environmental impact, particularly in terms of greenhouse gas emissions and air pollution.

The exponential growth of air traffic volume is demonstrated through a detailed analysis of the Revenue Passenger Kilometer (RPK), which is calculated by multiplying the number of passengers by the distance flown per passenger. RPK has grown from 1 billion kilometers in the 1980s to approximately 3 billion kilometers in 2000, and currently stands at around 8 million kilometers, data readable from figure 1.1 [29]. As a result, it is unsurprising that aviation accounts for 2% of CO2 emissions and 13% of fossil fuel consumption in transportation [6].

CO2 emissions from aviation have steadily increased, except for specific periods such as the 1970s, 2009, and more recently during the pandemic. CO2 production in 2018 had quadrupled since 1966 and doubled since 1987, as highlighted in figure 1.2. While aviation is responsible for roughly 2.5% of global carbon dioxide (CO2) emissions, this is only a share of the contribution of aviation to climate change.

In addition to CO2, engine combustion also produces other byproducts such as nitrogen oxides, sulfur oxides, water vapor, hydrocarbons, and more [4]. When released, these substances interact with one another and the gases in the atmosphere, leading to changes in the upper troposphere and lower stratosphere. The chemical reactions caused by these byproducts can have both cooling and warming effects on the climate. Unfortunately, the warming effects tend to outweigh the cooling ones, which means that aviation plays a significant role in the issue of climate change.

As we shift our focus from environmental concerns to economics, it's worth noting that fuel costs make up a significant portion of airlines' operational expenses - ranging anywhere from 20% to 30% over time. While it's true that airlines are motivated to reduce fuel consumption in order to minimize their environmental impact, it's also worth acknowledging that profit maximization is a driving factor as well.

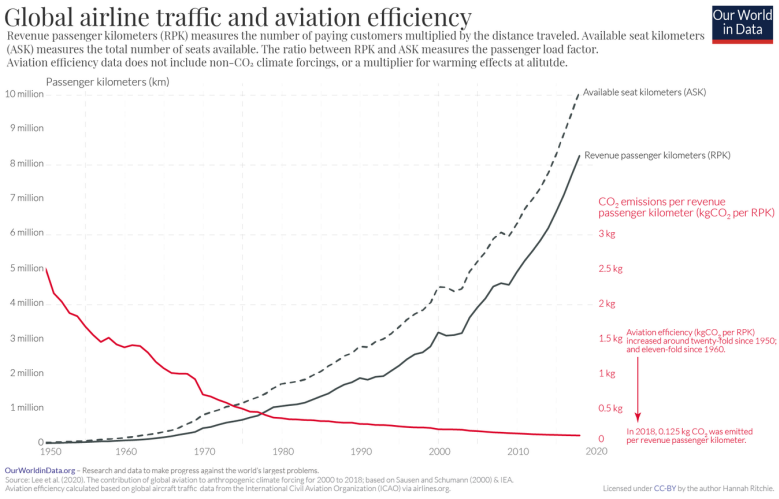

Figure 1.1: Revenue passenger kilometers and available passenger kilometers are plotted against the years. They serve as a measure of air traffic volume. In addition, the aviation efficiency, measured as kilograms of CO2 per RPK, is shown across the same years.

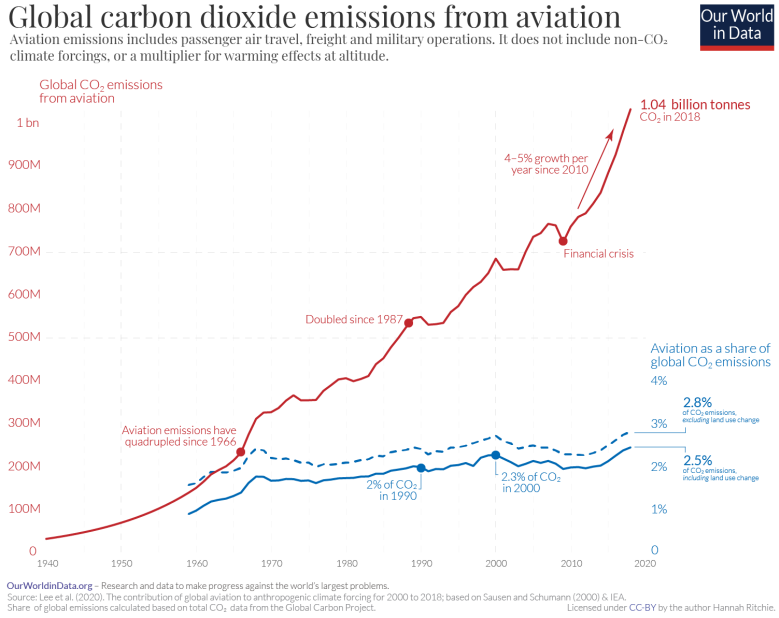

Figure 1.2: The CO2 emissions produced by aviation, both in absolute value and as a percentage of global CO2 emissions, tracked from 1940 to 2020.

To comply with regulations limiting aircraft pollutants, airplane manufacturers have made considerable efforts to ensure their planes and engines meet the latest standards. The impact of these regulations is evident by looking at the efficiency, measured as kilograms of C02 produced per RPK, in figure 1.1. Without any doubt, emissions have increased significantly over the last five decades due to the rapid increase in air traffic volume, but fortunately, the growth in

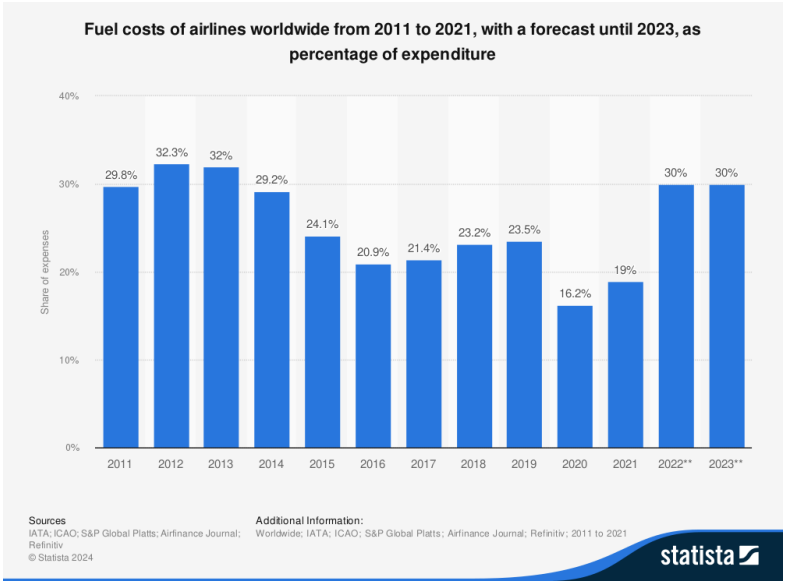

Figure 1.3: The share of fuel costs in airlines' expenditures from 2011 to 2021, with forecast until 2023.

the emission was slower than the growth in PRK thanks to the technological advances in the aeronautical sector. Since 1960, air transport emissions have risen by almost seven times, with a three-fold increase since 1970. In contrast, the number of revenue passenger kilometers flown has experienced exponential growth, increasing almost 300 times since 1950 and 75 times since 1960.

This reflects on aircraft efficiency, whose evolution is equally impressive. Since 1950, aviation efficiency has increased by a factor of 20. While much progress has been made recently, there is still room for improvement.

To mitigate the effects of pollution and the rising cost of airline fuels, two primary approaches are identified. Firstly, there is a focus on increasing the efficiency of the engine, aiming to produce the same amount of thrust while reducing fuel consumption. Secondly, efforts are directed towards the aircraft level, where novel concepts are introduced to reduce drag, which is balanced by thrust. The advantage of this approach is direct, as a reduction in drag readily translates to a reduction in thrust requirements and, consequently, lower fuel consumption.

Reducing drag can be achieved through various means, including the introduction of novel aircraft concepts such as Blended Wing Body and Closed Wing designs, the utilization of new and lighter materials, or the control of flow structures around key aircraft components.

Flow control features a wide range of applications such as separation and transition delay, lift increases, flow stabilization, flow reattachment, drag reduction, etc. For this purpose, different devices have been designed and employed which can be divided into three classes [33]:

- Passive: Passive devices involve surface geometrical modification or the addition of geometrical devices on the object's skin. The word passive refers to the absence of any source of mass, momentum or energy. Once they are applied to the body's skin they operate until they wear out. Examples of devices belonging to this group are riblets and vortex generators. Studies have demonstrated that surfaces with riblets can achieve a reduction of the total drag by 10%. On the other hand, a vortex generator produces vortices that promote the

mixing inside the boundary layer and make the flow close to the surface more energetic trying to delay separation and enhance the effectiveness of control surfaces.

- Semi-active: As the word active suggests, semi-active flow control involves sources of mass, momentum and energy that actively modify the boundary layer characteristics. For instance, suction removes the low momentum flow near the wall while tangential blowing aims to energize the lower region of the velocity profiles. The addition of the prefix active describes the operating strategy of these devices. Semi-active flow control features only two operating modes: on and off. Among semi-active flow control fall suction, blowing and plasma actuator

- Active: Active flow control involves the same actuation type of semi-active control (suction, blowing, and plasma). The only difference is that for active flow control devices, the actuation is a function of time.

One application of active flow control consists of trying to keep the flow in a laminar state (Laminar Flow Control LFC), also for Reynolds number at which flow is transitional or already turbulent without any control. Suction is often applied to achieve this task. Since laminar flows exhibit skin friction usually 90% lower than turbulent flow, by delaying transition we aim to reduce the skin friction drag and, in turn, the total drag [16]. This thesis aims to study numerically the suction control on a flat plate, trying to optimize the suction configurations in order to get the best gains out of the LFC.

In this thesis, chapter two lays the theoretical foundations of this thesis, scratching the surface of the boundary layer theory and linear stability theory. Chapter three describes the optimization algorithm invoked, while chapter four describes the numerical set-up used to estimate the extent of laminar flow on a flat plate. Chapter five describes directly the effect of suctions on different variables, while the following chapter analyzes and discusses the results of the optimization, concluding the chapter with a model allowing to predict the effect of the suction on the flow stability.

Chapter 2

Boundary Layer, Stability and Laminar-Turbulent transition

2.1 Boundary layer

2.1.1 Boundary layer concept

The Navier-Stokes equations possess the ability to model a wide range of situations in which fluids play a central role. These equations offer comprehensive and universally applicable descriptions of a vast array of phenomena spanning different scales, encompassing everything from oceanic currents and pipe flow to the evolution of fluids in turbomachinery stages.

For an incompressible and homogeneous fluid, the NS equations coupled with the continuity read [1]:

$$\begin{cases} \frac{\partial u_i}{\partial x_i} = 0 \\ \frac{\partial u_i}{\partial t} + u_j \frac{\partial u_i}{\partial x_j} = -\frac{1}{\rho}\frac{\partial p}{\partial x_i} + \nu \frac{\partial^2 u_i}{\partial x_j^2} \end{cases} \tag{2.1}$$

In certain situations, it can be more advantageous to express equations in their nondimensional form. This requires the identification of characteristic scales of length (L), velocity (V), and time ($T = L/V$) representative of the fluid system. The above quantities are used to normalize pressure and velocity fields, as well as independent variables such as the three spatial (x, y, z) coordinates and the time t. To distinguish dimensional quantities from their non-dimensional counterparts, the latter are denoted with a tilde $\widetilde{(\cdot)}$. The relationship between dimensional and non-dimensional quantities is explicitly stated below.

$$\widetilde{x} = \frac{x}{L}; \quad \widetilde{t} = \frac{t}{T}; \quad \widetilde{u_i} = \frac{u_i}{V}; \quad \widetilde{p} = \frac{p}{\rho V^2};$$

Finally, by substituting the new variables into the equation 2.1:

$$\begin{cases} \frac{\partial \widetilde{u_i}}{\partial \widetilde{x_i}} = 0 \\ \frac{\partial \widetilde{u_i}}{\partial \widetilde{t}} + \widetilde{u_j} \frac{\partial \widetilde{u_i}}{\partial \widetilde{x_j}} = -\frac{\partial \widetilde{p}}{\partial \widetilde{x_i}} + \frac{1}{Re}\frac{\partial^2 \widetilde{u_i}}{\partial \widetilde{x_j}^2} \end{cases} \tag{2.2}$$

Following a series of manipulations, the Reynolds number spontaneously appears as the coefficient of the viscous term.

$$Re = \frac{VL}{\nu} = \frac{Inertial\ forces}{Viscous\ forces} \tag{2.3}$$

This parameter can be considered one of the key parameters in fluid mechanics. Despite eq. 2.2 being a simple rewriting of the equations 2.1, it carries a significantly deeper meaning, leading to two fundamental concepts in fluid dynamics: similarity and boundary layer theory.

Indeed equation 2.2 immediately:

- introduces the concept of mechanically similar flows. Given two fluid systems that are geometrically similar (their geometries can be overlapped by applying a constant scaling factor), if these systems have the same Reynolds number, then they are said to be kinematically similar, meaning that corresponding points in the two systems possess the same values of non-dimensional variables [34]. The validity of this statement lies in the presence of a single control parameter as the coefficient of the non-dimensional equation. The consequence of this assertion is significant, as it implicitly suggests that knowing the evolution of pressure and velocity fields for a given geometry and Reynolds number allows for the prediction of the unknown fields for all systems in fluid dynamic similarity with the first one. Numerical and laboratory experiments heavily rely on this property.

- provides a direct and easy interpretation of the Reynolds number. As the Reynolds number increases, the contribution of the diffusive term in the momentum balance equation decreases. When the Reynolds number tends to infinity, the Navier-Stokes equations approach the inviscid Euler equations, which describe the motion of an ideal fluid. However, the approximation of inviscid flow under the assumption of a high Reynolds number cannot be universally applied. In the Euler equations, wall boundary conditions are typically defined as slip conditions; however, for the NS equation, even for Reynolds number tending to infinity, the no-slip condition at the wall must be applied. This is due to the fact that viscosity causes particles near the surface to adhere to it, thus enforcing a no-slip condition. In 1904, Prandtl resolved this dichotomy by introducing the concept of boundary layer.

2.1.2 Boundary Layer approximations

In 1904, during the third International Congress of Mathematicians held in Heidelberg, Germany, Prandtl presented the pioneering concept of boundary layer. Prandtl's work demonstrated that even at high Reynolds number conditions flow close to the walls is still affected by viscosity. In essence, when Reynolds numbers are significantly greater than one (Re»1), the velocity has approximately the same order of magnitude everywhere in the domain except for a thin layer near the walls. At the wall, fluid particles stick to the surface resulting in zero velocity relative to the object skin. This will further imply the existence of a thin region where quick velocity transitions occur (from fluid at rest on the wall to a velocity of the order characteristic flow velocity V, over a narrow distance δ). This thin region is known as *Boundary Layer* or *friction layer* [30].

The basic idea is to divide the fluid domain into two regions, with the boundary between them not sharply defined:

- A thin layer where the wall-normal velocity gradients $\partial u/\partial y$ are large, resulting in high frictional forces $\tau = \mu \partial u/\partial y$.

- The region external to the boundary layer where gradients are smoothed and viscosity effects are quiescent.

Within the boundary layer, there is a perfect balance between inertial, viscous, and pressure forces. By analyzing the differential operators related to the inertial and viscous forces in the

NS equations, it is feasible to determine the relative magnitude of these two forces. For example

$$u_j \frac{\partial u_i}{\partial x_j} \sim \nu \frac{\partial^2 u_i}{x_j^2} \rightarrow \frac{V^2}{L} \sim \nu \frac{V}{\delta^2} \rightarrow \frac{\delta}{L} \sim Re^{-\frac{1}{2}} \tag{2.4}$$

Where L is the length scale for the inertial force and δ is the length scale for the viscous force.

$$Re \gg 1 \rightarrow \frac{\delta}{L} \ll 1 \tag{2.5}$$

Making explicit the equation 2.2 for a 2D flows:

$$\underset{1}{\frac{\partial \widetilde{u}}{\partial \widetilde{x}}} \quad \underset{1}{+\frac{\partial \widetilde{v}}{\partial \widetilde{y}}} = 0 \tag{2.6}$$

$$\underset{1}{\frac{\partial \widetilde{u}}{\partial \widetilde{t}}} \quad \underset{1}{+\widetilde{u}} \quad \underset{1}{\frac{\partial \widetilde{u}}{\partial \widetilde{x}}} \quad \underset{\delta}{+\widetilde{v}} \quad \underset{\frac{1}{\delta}}{\frac{\partial \widetilde{u}}{\partial \widetilde{y}}} = \underset{}{-\frac{\partial \widetilde{p}}{\partial \widetilde{x}}} \quad \underset{\delta^2}{+\frac{1}{Re}} \quad \underset{1}{\left(\frac{\partial^2 \widetilde{u}}{\partial \widetilde{x}^2}\right.} \quad \underset{\frac{1}{\delta^2}}{\left.+\frac{\partial^2 \widetilde{u}}{\partial \widetilde{y}^2}\right)} \tag{2.7}$$

$$\underset{\delta}{\frac{\partial \widetilde{v}}{\partial \widetilde{t}}} \quad \underset{1}{+\widetilde{u}} \quad \underset{\delta}{\frac{\partial \widetilde{v}}{\partial \widetilde{x}}} \quad \underset{\delta}{+\widetilde{v}} \quad \underset{1}{\frac{\partial \widetilde{v}}{\partial \widetilde{y}}} = \underset{}{-\frac{\partial \widetilde{p}}{\partial \widetilde{y}}} \quad \underset{\delta^2}{+\frac{1}{Re}} \quad \underset{\delta}{\left(\frac{\partial^2 \widetilde{v}}{\partial \widetilde{x}^2}\right.} \quad \underset{\frac{1}{\delta^2}}{\left.+\frac{\partial^2 \widetilde{v}}{\partial \widetilde{y}^2}\right)} \tag{2.8}$$

Jumping back to the dimensional form, the three main equations are:

$$\begin{cases} \frac{\partial u}{\partial x} + \frac{\partial v}{\partial y} = 0 \\ \frac{\partial u}{\partial t} + u\frac{\partial u}{\partial x} + v\frac{\partial u}{\partial y} = -\frac{1}{\rho}\frac{\partial p}{\partial x} + \nu\frac{\partial^2 u}{\partial y^2} \\ \frac{\partial p}{\partial y} = 0 \end{cases} \tag{2.9}$$

Following these simplifications, several important considerations arise. The most relevant pertains to the considerable simplification of the momentum equation along the y-direction. Pressure within the boundary layer is independent of y. The imposition of pressure as a boundary condition outside the boundary layer is sufficient for a unique definition of the pressure within and allover the BL. Thus, the pressure throughout the boundary layer is determined by the boundary conditions, resulting in a reduction of variables from 3 (u, v, p) to 2 (u, v). The continuity equation remains unchanged, while the momentum equation in the x-direction loses a diffusive term. Additionally, the mathematical nature of the system changes. While the original equations are elliptic, the boundary layer equations take on a parabolic nature.

2.1.3 Flat-plate Boundary Layer

In this section, the equations describing a uniform flow impinging on a flat plate will be derived. This will also provide the opportunity to introduce and define several quantities used throughout the following discussions, such as boundary layer thickness, displacement thickness, momentum thickness, or even the friction coefficient. These parameters play an integral role in the characterization of fluid flow behavior and contribute to a deeper understanding of the underlying physical mechanisms.

A theoretical approach is adopted thus an infinitely long plate is studied. The velocity profile inside the BL constitutes a self-similar solution usually referred to as the Blasius solution. As the term self-similar implies, by suitably scaling the dependent and independent variables, (i.e. the velocity profile (u) and the distance from the plate (y) respectively) the normalized velocity profiles (u/U_∞) at different x stations can be collapsed onto a single curve. In other words u/U_∞

is only a function of the normalized distance $\eta = y/\delta$, where δ represents a measure of the BL thickness.

By considering the dimensional nature of the involved quantities and relying on a certain degree of physical intuition, it is possible to derive a relationship for the boundary layer thickness δ as a function of the coordinate x, representing the direction aligned with the free stream velocity.

Boundary Layer(BL) thickness δ can be defined as the fluid region where the viscous effects are significant, therefore BL development must somehow depend on the kinematic viscosity ν, involved in modeling viscous phenomena. By combining the variables ν and δ, it is possible to obtain a velocity called U_ν that represents the velocity component, normal to the wall, at which particles move away from it due to viscous transport.

$$U_\nu = \frac{\nu}{\delta} \tag{2.10}$$

A particle that begins its journey through the flat plate, starting from the leading edge (x, y)=(0, 0), will be advected in a streamwise direction by a Δx over a time interval estimated as $\Delta t = \frac{\Delta x}{U_\infty}$. During this time, the particle will also undergo a vertical displacement $\Delta y = \delta = U_\nu \Delta t$. These relations can be used to estimate the evolution of BL thickness.

$$\frac{\Delta x}{U_\infty} = \frac{\delta}{U_\nu} \tag{2.11}$$

Having imposed that at $t = t_0$, $x_0 = 0$ it follows that $\Delta x = x$.

$$\frac{x}{U_\infty} \sim \frac{\delta^2}{\nu} \Longrightarrow \delta \sim \sqrt{\frac{\nu x}{U_\infty}} \tag{2.12}$$

The parameter $\delta(x)$, often referred to as the boundary layer thickness, may not be unambiguously defined due to the lack of a clear boundary between BL and the outflow. However, it can be regarded as a measure of the thickness up to a certain factor that multiples the square root in eq. 2.12. For convenience:

$$\delta(x) = \sqrt{\frac{2\nu x}{U_\infty}} \tag{2.13}$$

Where the factor $\sqrt{2}$ is arbitrary and it was chosen to simplify some coefficients in the final equation.

A stream function can be introduced

$$\Psi = \sqrt{2\nu x U_\infty} f(\eta) \tag{2.14}$$

Where $f(\eta)$ is the normalized stream function. From Ψ, the velocity components are readily resumed by differentiating the stream function.

$$u = \frac{\partial \Psi}{\partial y} = \frac{\partial \Psi}{\partial \eta}\frac{\partial \eta}{\partial y} = U_\infty f'(\eta) \tag{2.15}$$

$$v = -\frac{\partial \Psi}{\partial x} = -\left(\frac{\partial \Psi}{\partial x} + \frac{\partial \Psi}{\partial \eta}\frac{\partial \eta}{\partial x}\right) = \sqrt{\frac{\nu U_\infty}{2x}}\left(\eta f' - f\right) \tag{2.16}$$

The equations governing the boundary layer development are expressed by Equation 2.1. For a flat plate, these equations are further simplified assuming a zero external pressure gradient. Writing down the x-momentum boundary layer equation for a flat plate yields:

$$u\frac{\partial u}{\partial x} + v\frac{\partial u}{\partial y} = \nu\frac{\partial^2 u}{\partial y^2} \tag{2.17}$$

Upon substitution of equations 2.15 and 2.16 in 2.17 it ends up in the Blasius equation:

$$f''' + ff'' = 0 \tag{2.18}$$

With boundary conditions:

$$\begin{aligned} y = 0: \quad & u = 0 \quad v = 0; \\ y \to \infty \quad & u = U_\infty \end{aligned}$$

Introducing the normalized stream function then BC will transform into:

$$\begin{aligned} \eta = 0: \quad & f = 0 \quad f' = 0; \\ \eta \to \infty \quad & f' = 1 \end{aligned}$$

There is no closed solution to the Blasius BL equation. However, it is possible to solve them by numerical integration.

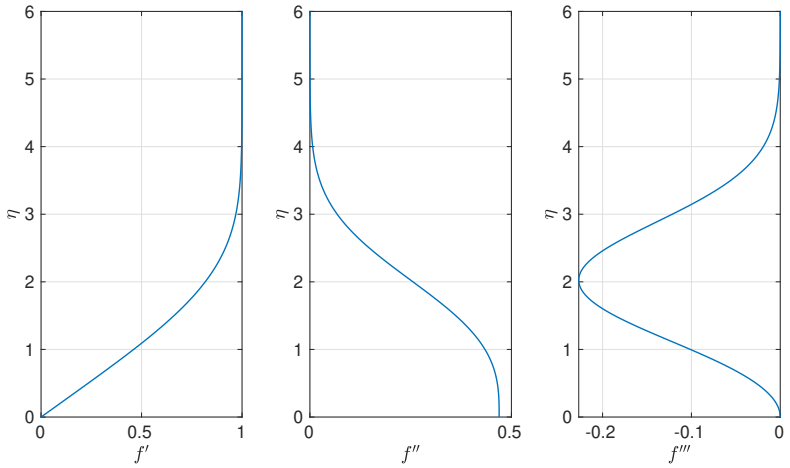

Figure 2.1: Blasius solution: normalized stream function derivatives profiles, with respect to η, as functions of η. The derivatives are indicated by the dash.

Boundary layer characteristic quantities

The lack of any sharp boundary between the boundary layer and the flow leads to different definitions of boundary layer thickness:

- **Boundary layer thickness** δ_{99}: it is the distance from the wall where the velocity reaches the 99% of the BL external velocity:

$$u(\eta_{99}) = 0.99U_e; \quad \eta_{99} = 3.6 \tag{2.19}$$

$$\delta_{99} \simeq 5.0\sqrt{\frac{\nu x}{U_e}} \tag{2.20}$$

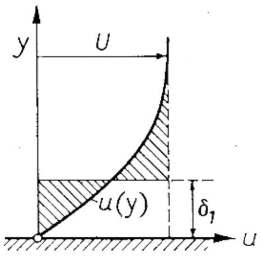

Figure 2.2: Visual representation of interpretation about the displacement thickness δ_1. The shaded regions have the same area [30].

- **Displacement thickness** δ_1. It represents the displacement in the wall's normal direction such that the volume flux of a uniform profile, equal to the BL edge velocity is equal to the BL flux(figure 2.2).

$$\delta_1 U_e = \int_0^\infty \big(U_e - u\big) dy$$
$$\delta_1 = \int_0^\infty \left(1 - \frac{u}{U_e}\right) dy$$

  Applying that definition to the Blasius solution:

$$\delta_1 = 1.7208\sqrt{\frac{\nu x}{U_e}} \tag{2.21}$$

- **Momentum thickness** δ_2:The momentum thickness refers to the perpendicular distance to a reference plane, which signifies the lower boundary of an idealized inviscid fluid with uniform velocity U_e. This ideal fluid is conceptualized to possess an equivalent momentum flow rate to that observed in the actual fluid within the boundary layer.

$$\rho U_e^2 \theta = \rho \int_0^\infty u\,(U_e - u)\,dy \tag{2.22}$$

$$\theta = \int_0^\infty \frac{u}{U_e}\left(1 - \frac{u}{U_e}\right) dy \tag{2.23}$$

  For Blasius BL

$$\theta = 0.664\sqrt{\frac{\nu x}{U_\infty}} \tag{2.24}$$

- **Shape factor** H: ratio between the displacement thickness and the momentum thickness

$$H = \frac{\delta_1}{\theta} \tag{2.25}$$

  For Blasius BL $H = 2.59$

The only type of drag that acts on a flat plate is the friction drag, which is defined as follows:

$$\frac{D}{b} = \int_0^L \tau_w(x) dx \tag{2.26}$$

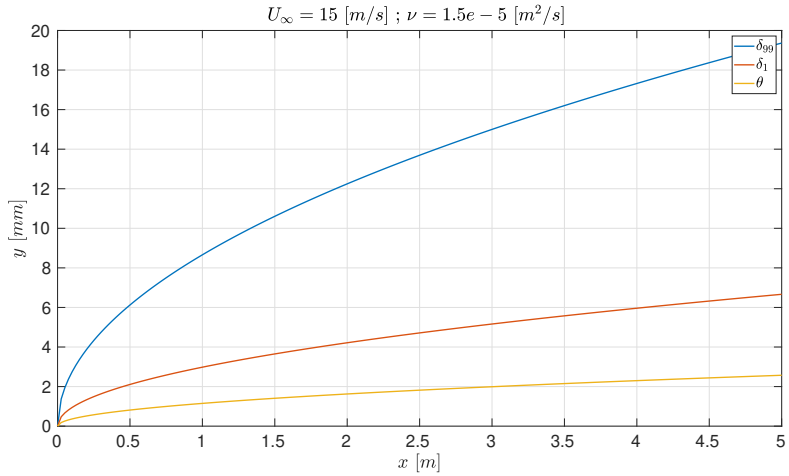

Figure 2.3: Development of boundary layer δ_{99}, displacement δ_1 and momentum thickness θ for a flat plate with $U_\infty = 15\ [m/s]$ and $\nu = 1.5 \times 10^{-5}[m^2/s]$.

Where b is the plate depth (the plate is a rectangle of $b \times L$), L is the plate length and $\tau_w(x)$ is the wall shear stress

$$\tau_w(x) = \tau(x, y = 0) = \mu \frac{\partial u}{\partial y}\bigg|_{y=0} \tag{2.27}$$

The skin friction coefficient is the adimensional version of the wall shear stresses:

$$c_f = \frac{\tau_w}{\frac{1}{2}\rho U_\infty^2} \tag{2.28}$$

For the Blasius

$$\tau_w(x) = 0.332 \mu U_\infty \sqrt{\frac{U_\infty}{\nu x}}; \quad c_f = 0.664 \sqrt{\frac{\nu}{U_\infty x}} \tag{2.29}$$

2.2 Linear Stability Theory

In certain circumstances, particularly those marked by a high Reynolds number regime, fluids have a propensity to deviate from the laminar state and transition towards a turbulent state. This phenomenon, commonly referred to as laminar-turbulent transition or onset of turbulence, is of great significance in the fluid mechanics field. As such, it has emerged as a key area of study and interest among the scientific community.

The main goal of Liner Stability Theory (LST) lies in finding the condition under which small perturbations, inherently included inside any real fluid system, will be damped or magnified, leading to defining the conditions of existence of laminar flow.

It is worth reserving some words about the phenomenology of turbulence, which also allows to understand the reason for its arising. The problem will be taken with a mathematical approach, studying the mathematical properties of the NS equations.

In turbulent flows, velocity and pressure fields are defined as random. Without conferring any additional meaning to the word random, the right interpretation of the characteristics that this term takes on can be expressed as follows.: "in a turbulent flow, the velocity or pressure

Laminar	Turbulent
layered, regular	disordered
smooth	fluctuating
ordered	chaotic

Table 2.1: Difference between laminar and turbulent flow

fields are random because experimental measurement of these fields in the same point in space and at the same time, in repeated experiments, will lead to a non unique measure" [27].

NS are deterministic equations. Theoretically, this means that given the NS with appropriate initial and boundary conditions, it is possible to follow the evolution of physical quantities as functions of time. The above statement seems to come up against the random behavior of the flow fields.

During the 19th century, the mathematician Hadamard introduced the concept of a well-posed problem. A problem is considered well-posed when the solution to a system of differential equations satisfies the following conditions [39]:

- **existence**: a solution exists;
- **uniqueness**: there is one and only one solution to the problem;
- **stability**: small perturbations of initial conditions (ICs)and boundary conditions (BCs)lead to small variations of the solution;

The first two conditions represent a deterministic view of the universe. The third condition distinguishes between the ideal and the real world. Mathematically speaking, if we know the ICs & BCs with infinity accuracy, the solution is completely known. Given the proper, ICs & BCs it is possible to predict the state of a system exactly at any time in the future. The reality is different as ICs & BCs are known with only finite accuracy, therefore the uncertainty associated with them makes impossible the detailed prediction of the system evolution.

In order to better understand the impact of uncertainty of ICs and BCs on differential equations and their solutions, it is often helpful to consider a classical example. By doing so, one can experience firsthand the direct effects of such uncertainties on the resulting solutions. Recalling the Lorenz problem, which consists of a system of three ordinary differential equations:

$$\begin{cases} \frac{dx}{dt} = \sigma(y - x) \\ \frac{dy}{dt} = \rho x - y - xz \\ \frac{dz}{dt} = -\beta z + xy \end{cases} \tag{2.30}$$

With $\sigma = 10$, $\beta = \frac{8}{3}$ and $\rho = 28$. To illustrate the sensitivity upon the initial conditions it is convenient to define two sets of them.

$$[x_0,\ y_0,\ z_0]_A = [0.1,\ 0.1,\ 0.1] \tag{2.31}$$

$$[x_0,\ y_0,\ z_0]_B = [0.100001,\ 0.1,\ 0.1] \tag{2.32}$$

In the beginning, the two systems, A and B, characterized by the different initial conditions, are nearly the same, but close to 30s, they start diverging from one another. This illustrative example serves to demonstrate that, in the case of an ill-posed problem, even small uncertainties or perturbations in the initial conditions can render any predictions about the system's state impractical and meaningless. In the context of the example, where the initial state is unknown

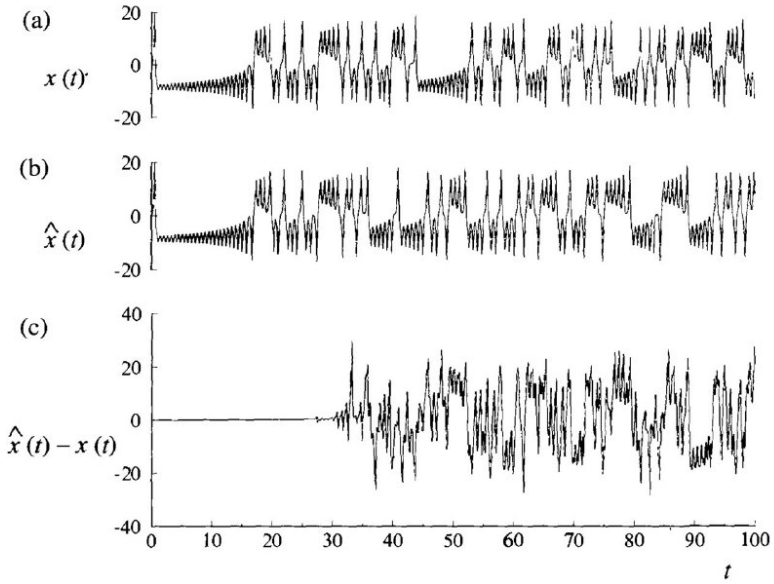

Figure 2.4: Time evolution of x variable from the Lorentz system. Here x represents the evolution of the system subject to A initial condition, while $\hat{x}$ is the time history that follows the B initial condition.

to within 10^{-6}, the difference between system A and B is substantial (2.4 (c) shows that the difference becomes large from about $t > 30s$).

The behavior of differential equations is heavily influenced by their coefficients. Interestingly, a parallel can be made between the Lorentz equation and the NS equations, as they both exhibit a critical parameter value that demarcates the threshold between two different types of solutions. In the Lorenz equation, if ρ takes a value below $\rho^* = 24.74$, the system will converge to a stable fixed value. However, if ρ is greater than ρ^*, the variables will exhibit chaotic behavior. ρ is a control parameter for the Lorenz equation as Re does it for the NS equations. In a low Reynolds number regime is very likely that flow is laminar but if the Reynolds number increases too much the arisen of turbulent flow, coming with the randomness associated with it, becomes more and more probable.

Therefore, now the answer to the debate between deterministic equation-random solutions should be clear. It is twofold and closely related to the well-posed problem.

- Any turbulent flow is unavoidably subject to perturbation in initial conditions, boundary conditions and material properties. These perturbations can arise from various sources, such as the vibration of mechanical systems, temperature inhomogeneities, impurities in the flow, surface roughness, and perturbations in the initial conditions.

- Turbulent flow exhibits an acute sensitivity to these perturbations. Perturbations are also present in laminar flows, however their stability result in minimal impact on the solution.

This introduction emphasizes the importance of studying stability and its role in generating turbulence.

2.2.1 Stability in parallel flow- Orr Sommerfeld equation

The fundamental pillar of linear stability theory (LST) lies in examining minor disturbances that are applied to a smooth, undisturbed, steady base laminar flow. As highlighted in the preceding chapter, perturbations play a crucial role, especially in the transition process. Consequently, the LST aims to determine the circumstances in which these perturbations are either amplified (leading to unstable flow conditions) or dampened (resulting in stable flow conditions).

The flow can be decomposed in its mean part(capital letters) and the fluctuating part due to the perturbations ($(\cdot)'$):

$$u = U + u' \quad v = V + v' \quad w = W + w' \quad p = P + p' \tag{2.33}$$

Base, laminar flow satisfies the governing equations (NS or BL equations). Assuming a 2D, steady, incompressible and locally parallel flow, the mean field can be written as

$$U = U(y) \quad V = W = 0 \quad P = P(x, y) \tag{2.34}$$

Although this assumption accurately describes the flow in a channel or pipe with a constant cross-section, it is not entirely precise for boundary layer flow. This is because the BL velocity field changes with x, moreover, the component V is not equal to zero. Nonetheless, this assumption remains a reasonable approximation for BL flow since the dependence of U on x is much lesser than on the y direction, and the velocity component V is significantly smaller than U [30].

The perturbations are function of space and time and can be regarded as small compared to the velocity U.

$$u' = u'(x,\ y,\ t) \quad v' = v'(x,\ y,\ t) \quad w' = w'(x,\ y,\ t) \tag{2.35}$$

$$u',\ v',\ w' \ll U \tag{2.36}$$

Upon substituting the decomposed variables 2.33 into the Navier-Stokes (NS) equation, the product between fluctuating velocities will emerge. If the original perturbation possesses a frequency ω, the multiplication of two perturbations can be deconstructed into the sum of one perturbation with zero frequency and another with a frequency 2ω. Consequently, the nonlinear interaction alters the mean flow, a mechanism often denoted as mean flow distortion, and introduces higher harmonics [8]. Nonetheless, it is feasible to neglect any product between two or more perturbations appearing in the governing equations (either NS or boundary layer equations), as these terms are negligible compared to a single perturbation. By retaining the first order perturbations, the nonlinear governing equations have been linearized.

The greatest advantage coming from the linearization consists in the validity of the superposition principle, one of the most important properties that linear systems feature.

If two perturbations are solutions of the stability equation, any linear combination of those two will still satisfy it. Consequently, given any perturbations, it is possible to conduct a Fourier decomposition. Each elementary wave that composes the original perturbation will evolve independently of the others, enabling the evaluation of the stability of each wave separately. The aforementioned reason justifies the *normal mode approach*. The solenoidal nature of perturbations allows for the introduction of a stream function Ψ.

$$u' = \frac{\partial \Psi}{\partial y};,\ v' = -\frac{\partial \Psi}{\partial x}; \tag{2.37}$$

The ansatz used for one mode is the following:

$$\Psi(x, y, t) = \phi(y) e^{i(\alpha x - \omega t)} \tag{2.38}$$

$i = \sqrt{-1}$ is the immaginary unit; $\alpha = 2\pi/\lambda$ is the wave number and λ is the wave length; $\omega = 2\pi/T$ is the angular frequency and T is the period. The previous quantities characterize each mode that constitutes a perturbation. ϕ is the amplitude of the disturbance and it is only a function of y as the base flow is also solely a function of y. Therefore, the stream function is an implicit function of y but an explicit function of x and t.

$$u' = \frac{\partial \Psi}{\partial y} = \phi'(y) e^{i(\alpha x - \omega t)} \tag{2.39}$$

$$v' = -\frac{\partial \Psi}{\partial x} = -i\alpha\phi(y) e^{i(\alpha x - \omega t)} \tag{2.40}$$

Defining $c = \frac{\omega}{\alpha}$

$$c = c_r + ic_i \tag{2.41}$$

c_r is the phase velocity while c_i is the amplification factor. Having contextualized what is behind the Orr-Sommerfeld equation it is now possible to introduce the equation

$$(U - c)\left(\phi'' - \alpha^2\phi\right) - U''\phi = -\frac{i}{\alpha Re}\left(\phi'''' - 2\alpha^2\phi'' + \alpha^4\phi\right) \tag{2.42}$$

The dash represents the derivation with respect to the variable $\eta = y/\delta_1$, while the Reynolds number is:

$$Re = \frac{U_e \delta_1}{\nu} \tag{2.43}$$

U_e is the boundary layer edge velocity. The boundary conditions, needed to close the differential problem, are based on the idea that perturbations vanish at the wall and outside the boundary layer:

$$\begin{array}{lllll} y = 0: & u' = v' = 0 & \rightarrow & \phi = 0 & \phi' = 0; \\ y \rightarrow \infty: & u' = v' = 0 & \rightarrow & \phi = 0 & \phi' = 0; \end{array} \tag{2.44}$$

OS equation is a homogeneous ODE with homogeneous boundary conditions, therefore it constitutes an eigenvalue problem. Given a general profile $U(y)$, its second derivatives $U''(y)$ and α / ω (temporal/ spatial approach), eq. 2.42 establishes a functional relation among Re-α-ω.

2.2.2 Spatial and temporal approach

Using a normal mode approach it is possible to jump from a partial differential equation to a 4th order, ordinary differential equation in the unknown ϕ (eq. 2.42). This simplification doesn't come without complications. Two different parameters (ω and α have been introduced) resulting in more unknowns [8]. To handle the problem and hence reduce the number of unknowns one can assume that disturbance may growth or be damped in space or in time leading to a temporal or spatial approach.

- **temporal approach**: it assumes that perturbations, at a fixed point can change their amplitude as time goes by. The wave number α is a real number while $\omega = \omega_r + i\omega_i$ is complex.

$$\Psi(x, y, t) = \phi(y) e^{i(\alpha x - \omega t)} = \phi(y) e^{\omega_i t} e^{i(\alpha x - \omega_r t)} \tag{2.45}$$

- **spatial approach**: it assumes that perturbations, at a fixed time can change their amplitude moving with space. The wave number $\alpha = \alpha_r + \alpha_i$ is a complex number while ω is real.

$$\Psi(x, y, t) = \phi(y) e^{i(\alpha x - \omega t)} = \phi(y) e^{-\alpha_i x} e^{i(\alpha_r x - \omega t)} \tag{2.46}$$

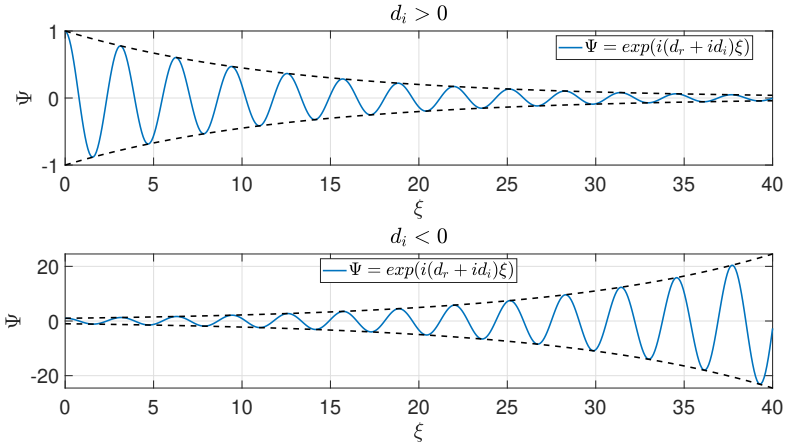

Figure 2.5: Evolution of the auxiliary model (of the stream function) as a function of the support variable ξ. The top figure shows a stable mode while the bottom an unstable one

Both equations 2.45 and 2.46 represent a sinusoidal function which amplitude is modulated by an exponential function.

To summarize, the effect that the real and imaginary parts of the wave parameters have on the stream function, without loss of generality, we utilize auxiliary variable ξ and parameters(d_r, d_i), assuming an initial perturbation of unit amplitude.

$$\Psi = 1 \cdot e^{i(d_r + id_i)\xi} \tag{2.47}$$

The spatial or temporal approach can be recovered from equation 2.47 substituting the corresponding quantities in the table 2.2.

	Growth with	Damped	Amplified
Auxiliary model	ξ	$d_i > 0$	$d_i < 0$
Spatial approach	x	$\alpha_i > 0$	$\alpha_i < 0$
Temporal approach	t	$\omega_i < 0$	$\omega_i > 0$

Table 2.2: Relations among auxiliary model, spatial and temporal approach

If the real part of the exponential is greater than zero, the mode is unstable and the magnitude of the perturbation will grow. On the contrary stable modes have a negative real exponential coefficient such that the perturbation vanishes as time goes by or moving in downstream direction.

Temporal stability analysis was developed in the 19th century and utilized by prominent scientists such as Helmholtz, Kelvin, and Rayleigh. Spatial stability analysis, on the other hand, emerged more recently, as it was introduced only in the 1950s. In recent times, spatial stability analysis has garnered increasing significance compared to temporal stability. It has been observed that for parallel laminar flow, transition occurs primarily through the amplification of disturbances in the streamwise direction [22]. In light of the growing recognition of the importance of spatial amplification, this thesis adopts a spatial approach.

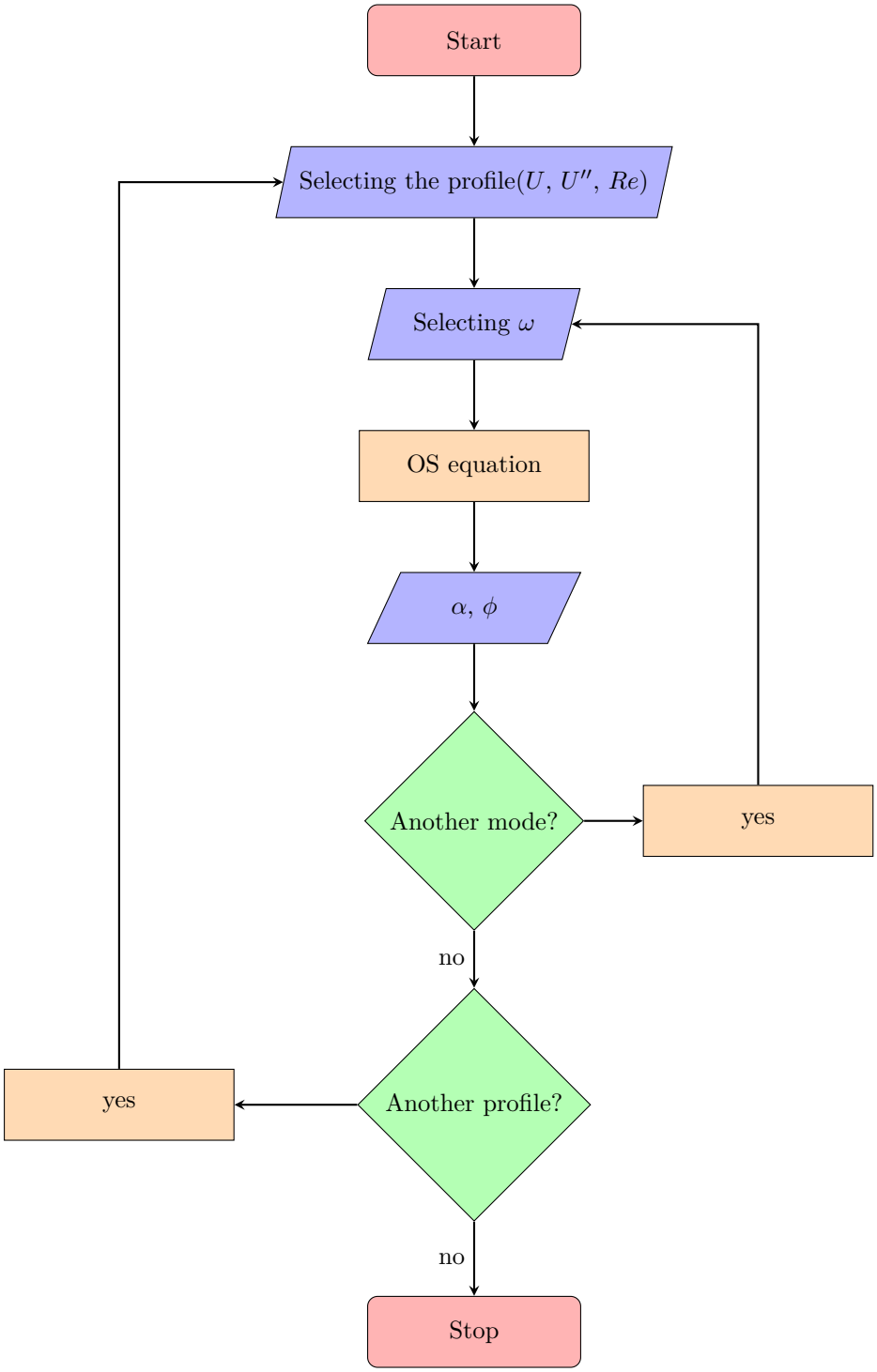

Stability calculation involves the following steps:

- Choosing a station x and extracting the velocity profile;

- Select a mode by choosing the angular frequency ω;
- Solve the Orr-Sommerfeld equation;
- Repeat the previous steps;

2.2.3 Stability diagrams

The results of the LST can be summarized in the stability curves.

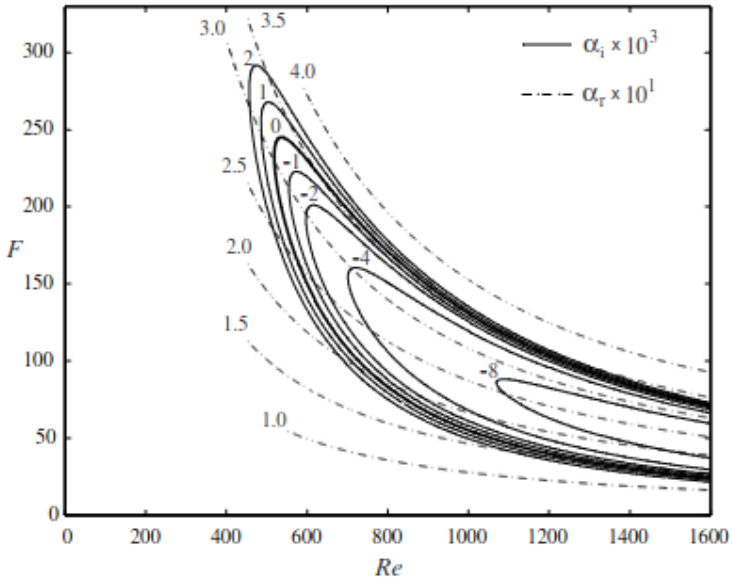

Figure 2.6: Spatial stability curve for Blasius boundary flow. layer [11]

In the x axis of figure 2.6 the Reynolds number is computed with the displacement thickness δ_1 ($Re = U_\infty \delta_1 / \nu$), while the y axes display a dimensional frequency F.

$$F = \frac{\nu \omega}{U_\infty^2} \times 10^6 \tag{2.48}$$

Solid lines are iso-α_i along which imaginary parts of the wave number is constant and dotted lines are iso-α_r representing the constant real parts of α.

The bold solid line $\alpha_i = 0$ denotes the marginal or neutral stability curve, as modes along this curve neither dampen nor amplify. The region enclosed by the marginal stability curve features unstable perturbations ($\alpha_i < 0$), thus defined as the unstable region. Conversely, the area exterior to the neutral stability curve is stable to any perturbations. Therefore, the marginal stability curve serves as the boundary between stable and unstable regions. Figure 2.7 shows the continuum variation of $-\alpha_i$ encompassed by the neutral stability curve.

Each Reynolds number corresponds to one velocity profile, such as different F refer to different modes. In the stability plane, each point is defined by the Reynolds number-angular frequency pair ($Re - F$). A wave number, composed of its real and imaginary part, can be associated with each point. Cutting the stability diagram with a vertical line (Re=constant) is equivalent to discussing the stability of a single velocity profile. For a low enough Reynold number the

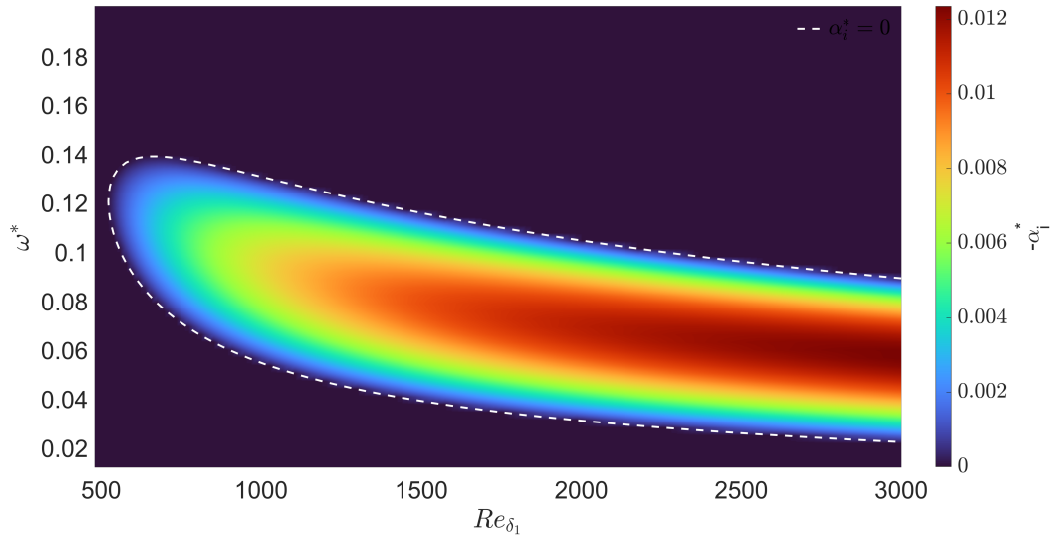

Figure 2.7: Stability diagram for Blasius profile. The white dashed line represents the neutral stability curve. To highlight the unstable region lower value of $-\alpha_i^*$ was saturated to 0

iso-Re line doesn't intersect the marginal stability curve, therefore the profile is stable to any perturbation. There will be a certain Reynolds number for which its iso line will intercept the neutral curve in one point (vertical line tangent to the neutral curve). The Reynolds number for which this condition is verified is called indifference Reynolds number (Re_{ind}). Profiles with $Re < Re_{ind}$ are stable but profiles with $Re > Re_{ind}$ are unstable. For $Re > Re_{ind}$ vertical lines cut the unstable region, showing a frequency range of unstable perturbations.

2.2.4 Rayleigh equation

It is possible to understand some important stability properties by looking at Rayleigh's stability equation, sometimes referred to as the inviscid stability problem.

$$(U - c)\left(\phi'' - \alpha^2\phi\right) - U''\phi = 0 \tag{2.49}$$

$$B.C.\ \ y = 0 \Longrightarrow \phi = 0;\ \ y \to 0 \Longrightarrow \phi = 0; \tag{2.50}$$

One of the most important results coming from this equation is called *Point of inflection criterion* which states: *"Velocity profiles with point of inflection are unstable"*

Rayleigh proved that point of inflection within the domain is a necessary condition for the presence of amplified waves[30].

Later on, this will be a powerful means to understand the stabilizing effect of the suction on the laminar profile.

2.3 Transition prediction method: e^N method

In 1956 Van Ingen [36] and Gamberoni & Smith [32] came out with a robust method allowing for transition prediction.

It has been previously noted that downstream of the indifference Reynolds number, a specific range of frequencies experience amplification. Employing the spatial approach entails that the amplitude a of a given mode of the stream function (see eq. 2.46) will vary with the coordinate x. The ratio of the disturbance's amplitude between locations x and $x + dx$ can be expressed as follows:

$$\frac{a + da}{a} = \frac{e^{-\alpha_i(x+dx)}}{e^{-\alpha_i x}} = e^{-\alpha_i dx} \tag{2.51}$$

$$-\alpha_i dx = ln(a + da) - ln(a) = d\big(ln(a)\big) \tag{2.52}$$

Integrating the above equation:

$$n(x, \omega) = ln\left(\frac{a}{a_0}\right) = \int_{x_0}^{x} -\alpha_i(x, \omega)dx \tag{2.53}$$

n is called amplification factor, $-\alpha_i$ is known as amplification rate and e^n is the amplification ratio [35]. x_0 is the point where the disturbance with frequency ω first becomes unstable.

The steps needed to build the n curves are shown in figure 2.8, where the quantities denoted as $(\cdot)^*$ are dimensionless parameters.

$$\alpha_i^* = \alpha_i \delta_1; \quad \omega^* = \frac{\omega \delta_1}{U_e} \tag{2.54}$$

To simplify the representation of the iso-ω curves in the stability map, it was decided to use the dimensionless angular frequency ω^* rather than ω on the ordinate. It is easy to see that, in this plane, the curves with fixed ω values are lines passing through the origin, whose slope F depends on the dimensional frequency ω.

$$\frac{\omega^*}{Re_{\delta_1}} = \frac{\omega \delta_1}{U_e} \frac{\nu}{U_e \delta_1} = \frac{\nu \omega}{U_e^2} = F(\omega) \tag{2.55}$$

Given the angular frequency ω we define for simplicity:

$$n_\omega(x) = n(x, \omega = const) \tag{2.56}$$

To draw $n_\omega(x)$ the following steps are required:

1. Compute the slope of the curve $F(\omega)$ and draw the curve in the stability diagram (figure 2.8a).

2. Sample $-\alpha_i$ along this line ((figure 2.8b)) to have $-\alpha_i(x, \omega = const)$.

3. Integrate $-\alpha_i(x, \omega = const)$

$$n_\omega(x) = \int_{x_0}^{x} -\alpha_i(x, \omega)dx \tag{2.57}$$

   x_0 is the intersection point between the lower branch of the neutral stability curve and the line $\omega^* = F(\omega) Re_{\delta_1}$.

By computing the amplification factor for a specific range of frequencies, it becomes feasible to represent the envelope of the amplification factor, hence called the *maximum amplification factor* N (2.9).

$$N = \max_{\omega} \left[n(\omega,\ x)\right] \tag{2.58}$$

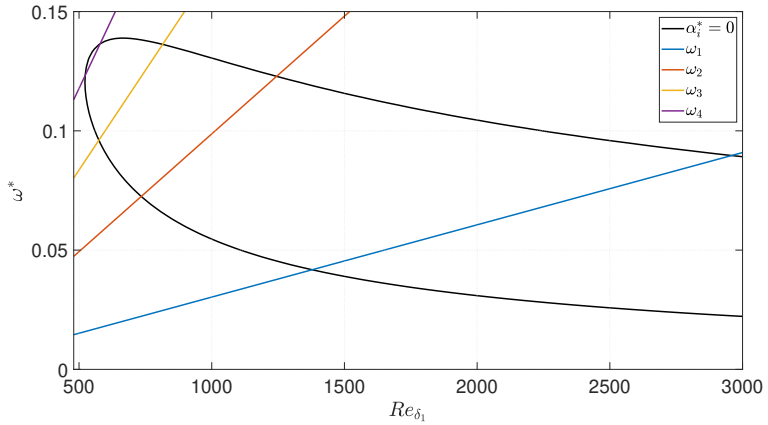

(a) Figure shows the neutral stability curve in black in the ω^*-Re_{δ_1} plane. The four lines are the locus of points with constant angular frequency.

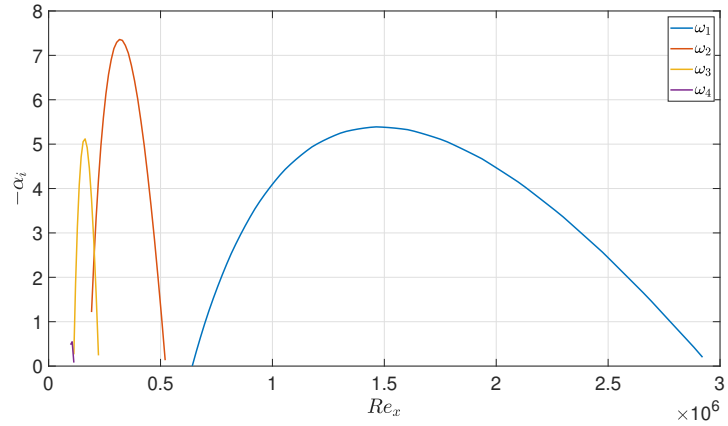

(b) Amplification rate $-\alpha_i$ expressed as function of Re_x. Along each curve ω is constant.

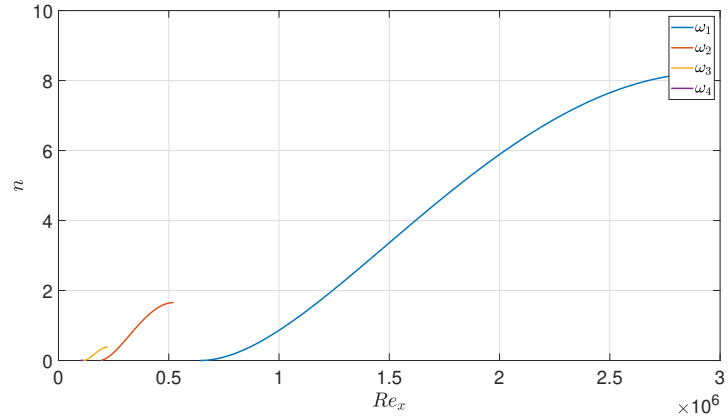

(c) Amplification factor for each mode($\omega = const$).

Figure 2.8: Post processing of the stability curves

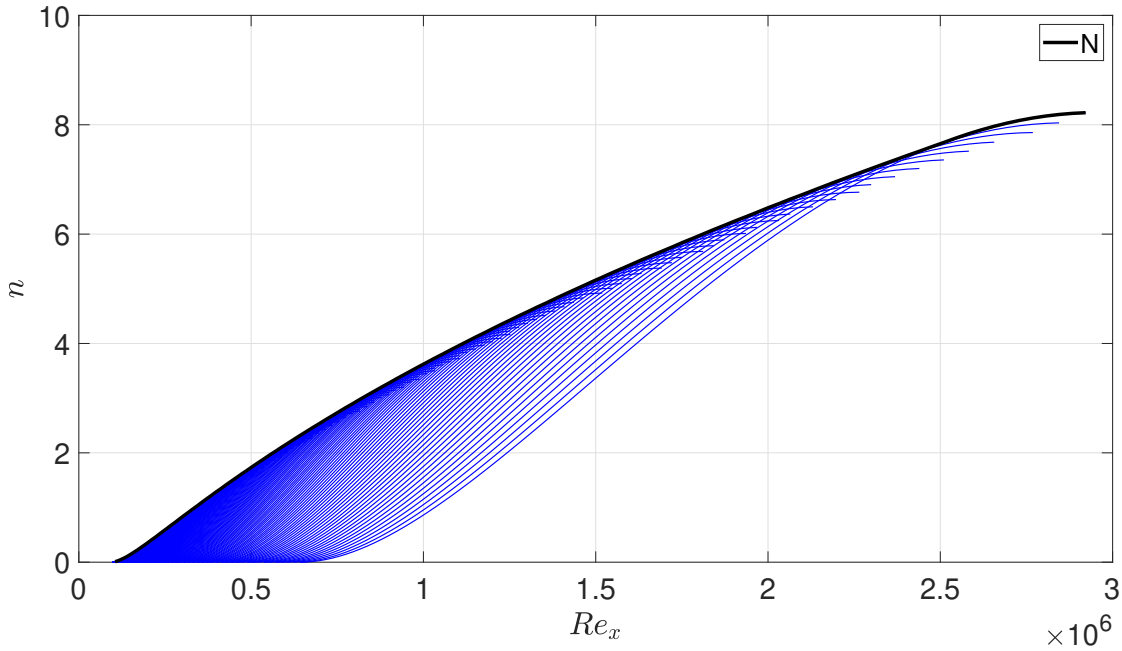

Figure 2.9: Maximum amplification factor is plotted in black along with the amplification rates, in blue color, that generate it

Van Ingen was guided by the flat plate experiment conducted by Schubauer and Skramstad, which revealed that transition occurs within a range of Re_{δ_1} between 2.8×10^6 and 3.9×10^6, corresponding to a $7.8 \leq N \leq 10$. Thus, as the N interval suggests, the transition requires a certain spatial extension before the flow, from laminar, turns to fully turbulent. It is important to note that the method of e^N is sometimes mistaken with e^9, but the choice of the exponent $N = 9$ as a reference value for transition was made by Smith in his experiments on the airfoil boundary layer transition, where the transition occurs over a small portion of the chord due to the adverse pressure gradient. For wind tunnels with low turbulence intensity ($Tu < 0.1\%$), transition location is no longer influenced by the free stream turbulence (FST); thus, $N = 9$ serves adequately for facilities designed for transition characterization and studies.

When turbulence intensity is high, it becomes possible to tailor the amplification factor at which transition occurs to accommodate the influence of free-stream turbulence. Empirical relationships propose that the N value at which transition initiates and concludes are:

$$N_1 = 2.13 - 6.18 log_{10}(Tu) \tag{2.59}$$

$$N_2 = 5 - 6.18 log_{10}(Tu) \tag{2.60}$$

Another relation available is the following:

$$N = -8.43 - 2.4 ln(T) \tag{2.61}$$

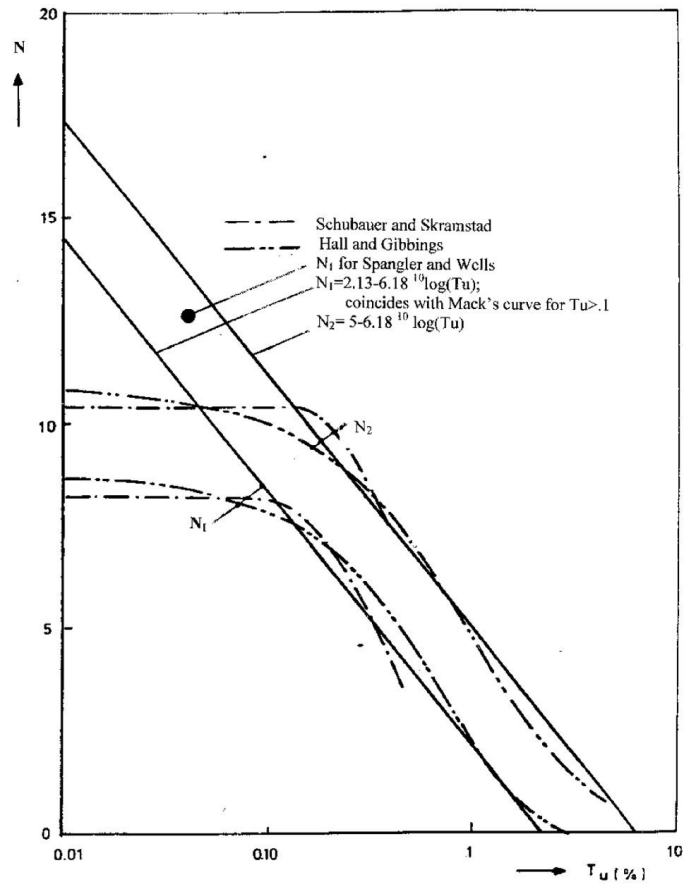

Figure 2.10: N factors for different flat plate experiments as function of turbulent intensity. [35]

2.4 Laminar-Turbulent transition

7 In the previous section, it was explained the reasons leading to turbulence from a mathematical perspective leveraging the ill and well posed problem. Leaving the mathematical world, a physical approach is now adopted.

The on set turbulent transition features three main stages [18], sketched in figure 2.11:

1. **Receptivity**: this field of study explores how external disturbances such as acoustic, vortical, temperature, and vibration perturbations penetrate at first inside the boundary layer. The leading edge shape is a critical feature in a flat plate when it comes to transitions study due to its high receptivity characteristics [31]. Leading Edge (LE) receptivity is one of the main mechanisms through which free stream disturbances are transformed in TS waves [17].

2. **Linear stability**: It was extensively treated in the previous section.

3. **Non linear breakdown**: It starts when the amplitude of the TS waves can no longer be considered small (e.g. perturbations are higher than 1% or 2% of the stream velocity U_∞) hence the hypothesis of the LST loses its validity. Despite this phase occurring over

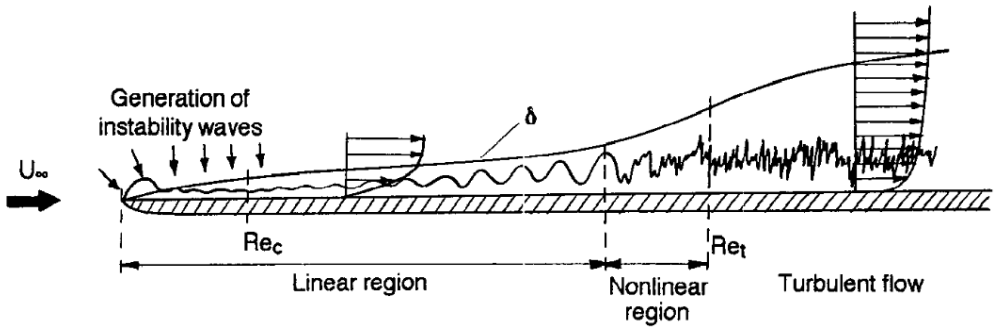

Figure 2.11: Flat plate boundary layer transition representation [17].

a short distance, it is arguably the most crucial stage as it involves the metamorphosis of the flow from a laminar, ordered, and deterministic state to a three-dimensional, unsteady, and chaotic turbulent flow.

2.4.1 Non linear breakdown

In addition to its inherent complexity, governed by nonlinear couplings, the phenomenon of nonlinear breakdown can manifest in various forms, often referred to as regimes. The two most significant regimes are the k-regime (named after Klebanov) and the N regime. Extensive studies of nonlinear breakdown began in the late 1950s and have continued until the present day, with a peak of interest observed between 1970 and 1980. During this period, significant progress was made in understanding the phenomenology involved in this process.

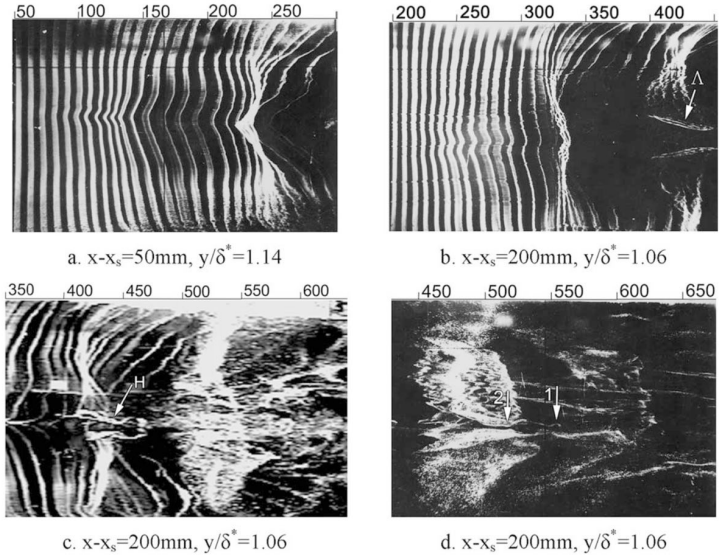

Figure 2.12: Flow structures in laminar-turbulent transitions

k regime

For scenarios characterized by low free stream turbulence and small initial perturbation magnitudes, the transition process unfolds through distinct phases, each characterized by unique flow structures. These phases are depicted in Figure 2.12, where the hydrogen bubble visualization technique has been employed.

In the initial stage, as depicted in Figure 2.12a, the perturbation represented by hydrogen bubbles exhibits 2D characteristics, primarily consisting of Tollmien-Schlichting (TS) waves. However, as a small perturbation begins to amplify and its amplitude increases, downstream generation of three-dimensional effects manifests. This amplification gives rise to the formation of the Λ vortex [14].

The subsequent evolution of the Λ vortex leads to the formation of the Ω vortex, also known as hairpin vortex, as shown in Figure 2.12c. The hairpin vortex is a vortical structure composed of two legs close to the ground and one head farther from the ground. These hairpin vortices are fundamental structures for the development of turbulent flow. They can either give rise to turbulent spots, as depicted in Figure 2.12b, or secondary hairpin vortices.

A turbulent spot consists of an ensemble of structures that entrain the neighboring flow. Consequently, a turbulent spot grows over time until the flow becomes fully turbulent.

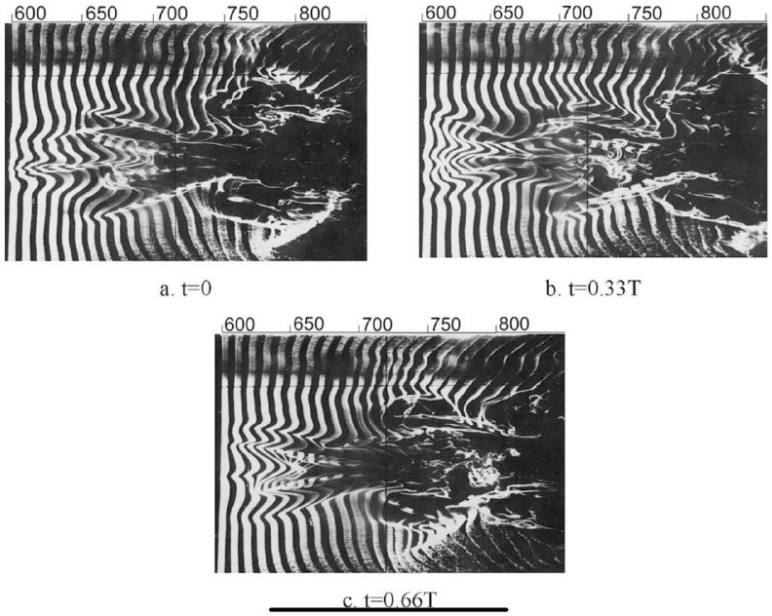

Figure 2.13: Turbulent spot structures

The artificial introduction of a 2D disturbances into the boundary layer by Klebanoff et al. resulted in the observation of a spanwise modulation of the wave front, characterized by regions with peaks and valleys of streamwise fluctuations, as illustrated in Figure 2.14.

Klebanoff found that the beginning of the breakdown process is marked by the presence of powerful and high-frequency flashes of perturbations called spikes on the streamwise-velocity oscilloscope traces. These spikes can double, or triple downstream (figure 2.15). The study concluded that these spikes play a crucial role in causing the final laminar-boundary-layer breakdown and flow randomization. Later was discovered that the spikes are the result of the

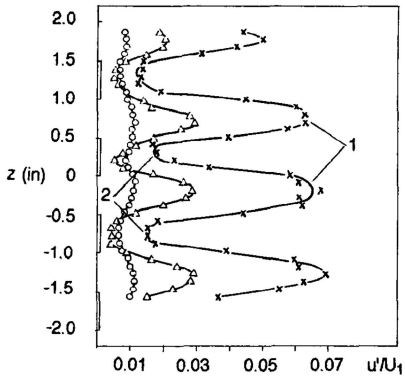

Figure 2.14: Spanwise modulation of 2D perturbation

induced velocity by ring vortex [2].

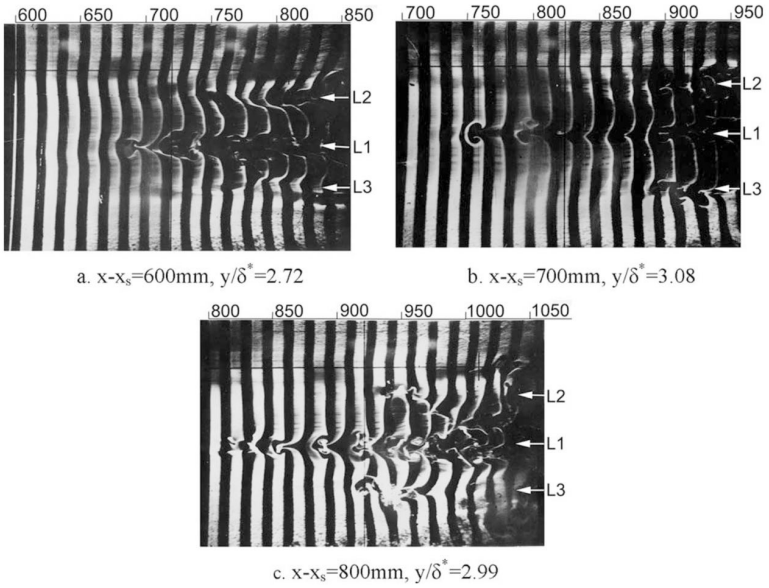

Figure 2.15: Hairpin vortex evolves downstream generating second hairpin vortex

2.5 Stability & suction: state of the art

Throughout the years, studies have proven suction to be an effective laminar flow control (LFC) technique mostly us ed to delay laminar-turbulent transition. The main objective of using LFC techniques for transition control is to maintain laminar flow over a region whose extension needs to be maximized. Given the fact that half of the total drag is caused by skin friction, this approach results in reducing the total amount of friction drag that an object experiences whenever there is relative motion between the body and the fluid surrounding it.

In his analysis, Marec provides a detailed breakdown of the sources of drag that airplanes encounter during the flight [24]. He pointed out that almost half of the total drag is caused by skin friction. He also presents an overview of the drag reduction project currently taking place in major industries such as Airbus, as well as research centers like ONERA and DLR, aimed at mitigating the effects of skin friction drag.

Laminar flow control technology for aircraft was first tested in wind tunnels in the late 1930s in the US [3]. Research efforts continued in both the US and Europe until the early 1960s, after which interest in this area declined. However, with the imposition of the oil embargo by OPEC in the 1970s and the subsequent sharp rise in fuel prices, research into laminar flow control systems experienced a resurgence. Successful flight tests, like Boeing 757 HLFC flight tests (1990–1991) reported a net drag saving by using micro-perforated titanium skin mounted on the nose of the wing [21]. The in-flight test showed that for a Mach number of 0.8, it was possible to save 8% of the fuel and have a drag reduction of 6%. Motivated by the excellent results of suction effects, GE attempted to apply HLFC (Hybrid Laminar Flow Control) to the nacelles of a large bypass turbofan jet engine. The HLFC concept proved to be extremely effective, resulting in laminar flow to 43 % engine nacelle length, independent of altitude[21]. To provide a more in-depth understanding of HLFC (Hybrid Laminar Flow Control), we recommend reviewing the following articles([21], [3]). The second article [21] delves into the history of laminar flow control research from the 1930s to 1999, with a specific emphasis on flight testing. The first article provides a comprehensive overview of the suction implementation system, with particular attention given to the characteristics of the porous medium, piping, and preliminary compressor design. Since experimental evidences have demonstrated the effectiveness of such a powerful technique, wind tunnel tests and theoretical studies have been performed for almost 50 years. The first experiment of which the author is aware dates back to 1977 when Kozlov et Al. carried out a wind tunnel investigation to explore boundary layer stability employing suction slots [20]. They aimed to analyze the effects of the suction through a solitary slot on a flat plate regarding mean flow and disturbance measurements. The outcomes highlighted a notable reduction in disturbance amplitude in the vicinity of the slot.

Nevertheless, the first experiment that paved the way for wind tunnel transition analysis was conducted by Reynolds and Saric in 1982 [28]. Using a wind tunnel with a turbulent intensity of 0.02% they studied the evolution of perturbation generated by a vibrating ribbon over a flat plate with and without suction. Different suction configurations were investigated with a fixing mass flow, assured by a sonic chocking nozzle. The plate was equipped with two porous panels, each composed of 16 spanwise flutes, allowing both continuous suction when all the flutes are active and local suction in the case of only a few suction strips opened. From figure 2.16 it is worth noting that despite the variegate suction configurations, the disturbance amplitude always slightly differs from one case to the other. Lingering any further on figure 2.16 it is remarkable that a single strip results as effective as 30 strips all together, under the assumption of equal mass flow.

In more recent years, an experiment on boundary layer transition over a flat plate was performed by Corelli [7]. At first, the effect of the porous panels at different Reynolds number was investigated. As predicted, the presence of the porous medium destabilizes the boundary layer. The reason for the earlier transition, when porous panel are employed, can be found in a combination of three causes:

- The presence of micro-holes has a similar effect to a rougher wall;
- Blowing through the porous wall, driven by the pressure difference between the two sides of the porous panel;

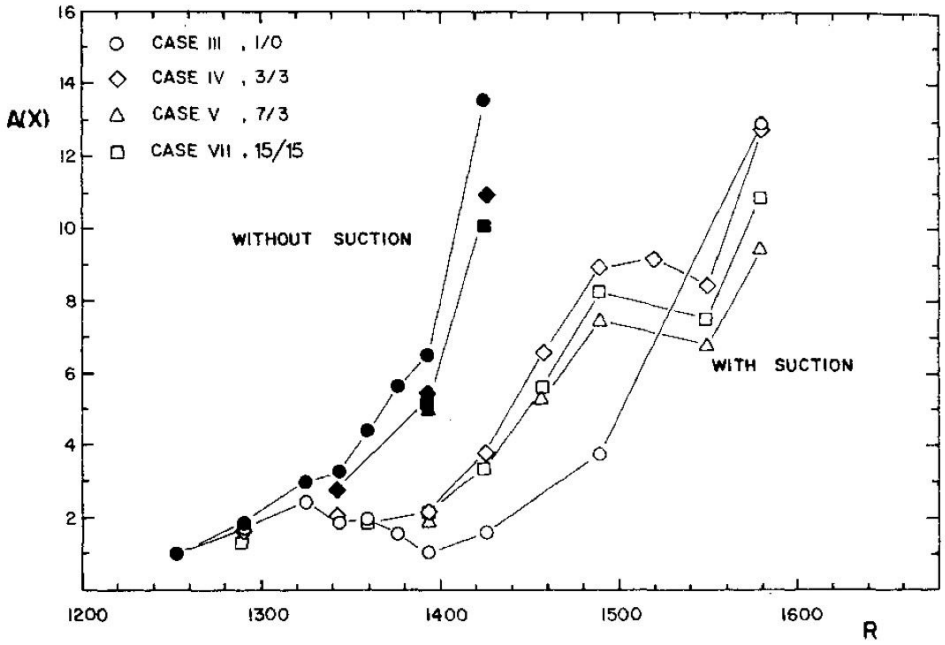

Figure 2.16: Disturbance amplitude A(x) vs $R = \sqrt{Re_x}$, the square root of $Re_x = U_\infty x/\nu$. The number on the side of each case (up-left corner) are referred to the number of flutes of the first slot and second slot(e.g. case V features 7 strips on the first panel and 3 on the second)[28]

- The volume of air inside the suction chamber can act as resonant cavity and magnify the perturbation amplitude.

Methel et Al. [25] show how the premature transition process is mainly triggered by the blowing effect. In figure 2.17 the velocity fluctuation as a measure of transition location is reported against both the Re_x and the stream-wise location x. As it is shown in the same figure, the velocity fluctuations start increasing earlier compared to the solid panel(no perforated). Covering the porous panel with the tape prevents the arisen of any vertical velocity components and, by measurements, it is proven that this little deed brings transition back again to the point of natural transition. This proves that the vertical velocity component is the main mechanism responsible for the earlier rising of the velocity fluctuations.

Figure 2.18 illustrates two important phenomena. The first is that increasing the free stream velocity U_∞, holding constant all the other parameters such as porosity, suction coefficient etc., causes the transition to move upstream. The second and most important result is that there is a limit on transition delays for a fixed slot location. That means that starting without any wall-normal velocity component, small increments of suction velocity will result in a remarkable shifting of the transition point. At the time when $C_Q = \frac{v_w}{U_\infty}$ is greater than the critical value, the increments of the suction mass flow will not be as effective as for the case with C_Q lower than this value, which can be traced back to the knee of the curves $C_Q - X_{TR}/L_{ref}$ (figure 2.18).

Linear Stability Theory (LST) is a widely accepted approach for analyzing disturbances in fluid dynamics. However, its applicability is limited to scenarios where the flow field variations occur at a length scale significantly larger than the characteristic wavelength of the inherent instability modes. In cases of abrupt distortions, where the distortion length is comparable to or

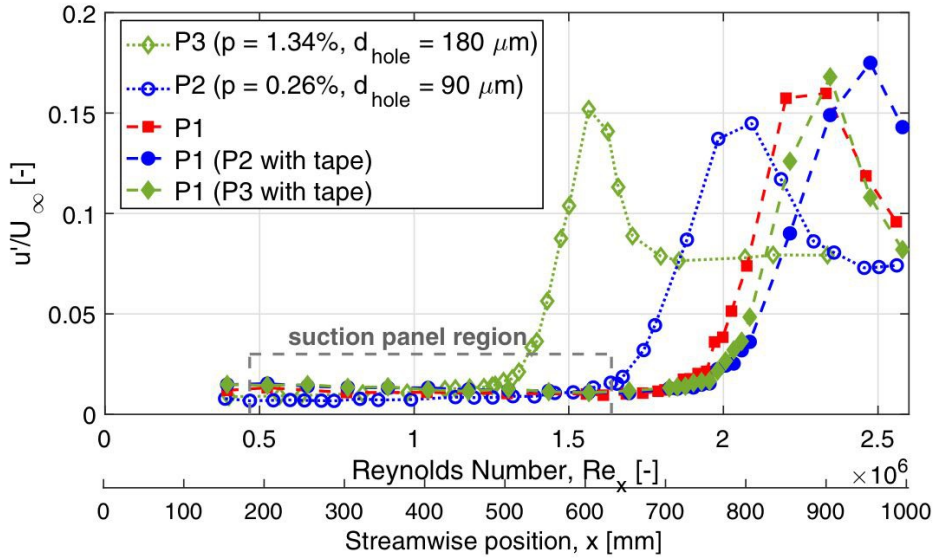

Figure 2.17: Streamwise velocity fluctuation vs Re_x for porous and solid walls. The effect of the tape on the velocity fluctuation is highlighted [25].

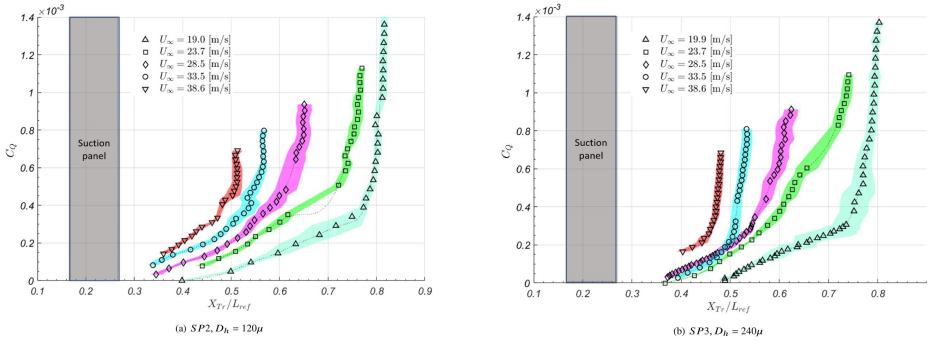

Figure 2.18: Suction coefficient $C_Q = v_w/U_\infty$ vs transition location. v_w is the suction velocity. Different Reynolds numbers have been considered [7]

shorter than the inherent instability mode's characteristic length, the conventional representation of the disturbance as a product of a slowly varying shape function and a rapidly oscillating carrier wave becomes invalid. Consequently, the normal-mode assumption, which is fundamental to both LST and the Parabolized Stability Equation (PSE), loses accuracy. Therefore, it becomes imperative to explore alternative methods for analyzing disturbances in such scenarios, as both LST and PSE rely on assumptions of slow variation of the mean flow and normal-mode.

Nevertheless, even in the case of localized suction (suction region extends over a small fraction of the body chord), under the condition of low velocity and mass flow sucked, the variation of the flow velocity field along the mean flow (stream wise) direction is gradual [15]. Recovering the Reynolds experimental data, Huang and Wu focused on case 3 of Reynolds experiment [28], which features a 16 mm slot with a mean suction velocity of $v_w/U_\infty = 5.7 \times 10^{-3}$. Whenever there is a rapid mean flow change, the effects of this distortion are reflected on stability through

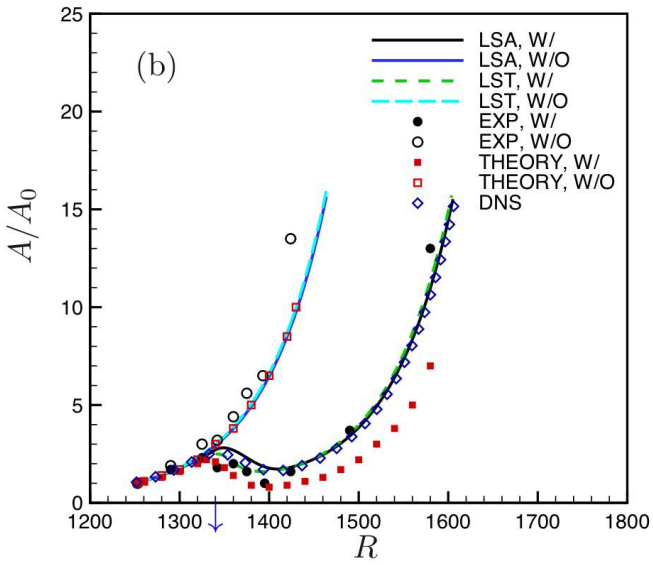

Figure 2.19: Comparison between the perturbation amplitude of LST, DNS, experiment and LSA

a scattering problem[41]. Wu and Dong proposed a method, called Local Scattering Approach (LSA) that tackles the stability in the nearby of the abrupt mean flow changes location by using a local scattering approaches [40]. Huang and Wu showed that even for localized suction with abrupt flow modification, LST is in a good agreement with the more sofisticated LSA theory(see figure 2.19)

Chapter 3

Optimization algorithms

Human nature drives individuals to seek the best possible outcomes in their lives. Optimization, therefore, is an inherent trait bestowed upon us by nature, one that we often employ, sometimes even unconsciously. Optimization manifests in various degrees of complexity. For instance, as we experience in everyday situations, stressed by time, people select the quickest route. Conversely, a farmer who wants to determine the most profitable crops to cultivate has to make careful considerations and strategic planning. While optimization may be a desired pursuit in personal life, it is an absolute necessity in the industrial world.

Optimization problems vary widely in complexity, requiring appropriate optimization algorithms to tackle them effectively. At its simplest level, optimization involves a known, concave and unconstrained objective function. In such cases, leveraging the knowledge about the function enables rapid convergence towards the optimal solution, often achieved through gradient-based optimization algorithms.

However, optimization becomes more challenging when dealing with functions that are non-concave or either constrained by complex relationships. In such scenarios, the mathematical properties of the function may impede optimization, requiring the application of more sophisticated algorithms and techniques.

Occasionally, situations arise where optimization objectives lack a closed-form formulation. Shape optimization of a structural component is one of them. Complex FEM calculations are required to ensure that the object will possess structural rigidity while maintaining lightweight characteristics. Similar examples can concern fluid dynamics problems as could be the airfoil's profile optimization constrained by some lift or drag requirements. In such cases, although gradient-based methods remain applicable, they can be cumbersome.

To address the challenges posed by the absence of closed-form formulations in optimization problems, diverse algorithms and strategies have been developed over the past fifty years. One such strategy is stochastic optimization, which introduces structured randomness during the search for optimal solutions. Many stochastic optimization methods take inspiration from natural processes [10]. For example, Genetic Algorithms (GA) emulate evolution by favoring the survival of the fittest individuals, thus preserving advantageous characteristics over successive generations. While evolution is indeed effective in selecting the most suitable individual for life, it operates on a timescale spanning thousands of years. Similarly, Genetic optimization algorithms exhibit a comparable trend, often characterized by slow convergence.

The Artificial Bee Colony (ABC) algorithm draws inspiration from the organizational structure of bees. In the ABC model, the colony comprises three primary bee groups: employed bees, onlookers, and scouts. Employed bees exploit known areas to gather nectar, which in the

algorithmic context represents the fitness value of the function. Onlookers observe the findings of employed bees and select the most promising nectar sources, reflecting the process of selecting the best design points. Meanwhile, scouts explore uncharted regions of the design space, analogous to searching for new sources of nectar, to continually optimize the algorithm. This model effectively captures the essence of natural bee behavior and applies it to the optimization process.

Among the various optimization algorithms available, one of the most efficient yet complex is Bayesian optimization.

3.1 Bayesian optimization

Considering a continuous optimization problem:

$$\begin{cases} \max_{\boldsymbol{x}} f(\boldsymbol{x}) & s.t. \\ g_i(\boldsymbol{x}) \leq 0 & i = 1, 2, \ldots m \\ h_i(\boldsymbol{x}) = 0 & i = 1, 2, \ldots p \end{cases}$$

$f(\boldsymbol{x})$ represents the function subject to the optimization process, while $\boldsymbol{g}(\boldsymbol{x})$ and $\boldsymbol{h}(\boldsymbol{x})$ denote the inequality and equality constraints that have to be fulfilled by the design vector variables $\boldsymbol{x} \in \Omega \subseteq \mathbb{R}^d$.

Bayesian optimization is suitable when[12]:

- The problem dimension is not too large, $d \leq 20$;
- Ω is simple set, for instance an hyper-rectangle $l_i \leq x_i \leq u_i$ (l_i: lower boundary, u_i: upper boundary);
- f is a continuous function, a necessary condition for Gaussian Process (GP) regression;
- f is costly to evaluate (typically from tens of minutes to a couple of hours);
- f being a black box function implies that its value can be queried at a given point without possessing any knowledge about its derivatives. Consequently, traditional optimization methods like gradient descent, Newton's method, or quasi-Newton methods cannot be applied due to the lack of derivative information.
- We aim to find the *global optimum* rather than the local optima.

Bayesian Optimization (BO) harnesses the power of the Gaussian Process (GP), serving as a statistical representation of the objective function, acting as a surrogate model. This surrogate model is leveraged by the algorithm to intelligently select the next evaluation point through the acquisition function.

BO is comprised of two primary processes: Modeling the objective function using Gaussian Process and determining the sampling policy, which dictates how the algorithm selects the next point for evaluation [13].

3.2 Gaussian process

Through a Bayesian approach, during the optimization process, unknown design points are considered to be random variables. This decision has far-reaching implications, as it permits each variable's value to be represented in a probabilistic manner, resulting in a cloud of potential values

that reflects the uncertainty inherent in the surrogate model. Not all values within this cloud have the same likelihood of manifestation, which is why the surrogate model is accompanied by a belief about the objective function's behavior that is supported by probabilistic considerations. This belief isn't static and established once and for all; instead, it can be refined when new evidence emerges from observations. The concept is expressed through the idea of a prior and a posterior distribution in the field of probabilistic inference. The prior distribution encapsulates our initial expectations or beliefs about the model, while the posterior distribution represents the updated belief after new evidence has been incorporated. This iterative process of refining beliefs based on observed data is the essence of Bayesian inference, enabling continuous learning and adaptation during the optimization process.

To have a better understanding it is convenient to begin with Gaussian distribution and then move towards Gaussian Process.

Univariate Gaussian distribution is uniquely defined by mean μ and the standard deviation σ.

$$P(x;\mu,\sigma^2) = \frac{1}{\sqrt{2\pi}\sigma} exp\left(-\frac{(x-\mu)^2}{2\sigma^2}\right) \tag{3.1}$$

In the case of multivariate Gaussian distribution, the expected or mean value is a vector $\boldsymbol{\mu}$ while the standard deviation σ is replaced by the covariance matrix $\boldsymbol{\Sigma}$. Consider a vector $\boldsymbol{x}$ of random variables.

$$\boldsymbol{x} = \begin{bmatrix} x_1 \\ x_2 \\ \vdots \\ x_d \end{bmatrix} \sim \mathcal{N}(\boldsymbol{\mu}, \boldsymbol{\Sigma}) \tag{3.2}$$

$\boldsymbol{x}$ follows a normal distribution with the joint probability given by

$$P(\boldsymbol{x};\boldsymbol{\mu},\boldsymbol{\Sigma}) = \frac{1}{(2\pi)^{\frac{d}{2}} \|\boldsymbol{\Sigma}\|} exp\left(-\frac{1}{2}(\boldsymbol{x}-\boldsymbol{\mu})^T \boldsymbol{\Sigma}^{-1}(\boldsymbol{x}-\boldsymbol{\mu})\right) \tag{3.3}$$

Where d is the dimension of the system, $\boldsymbol{x}$, $\boldsymbol{\mu} \in \mathbb{R}^d$ and $\boldsymbol{\Sigma} \in \mathbb{R}^{d\times d}$ while $\|\boldsymbol{\Sigma}\|$ is the norm of the covariance matrix.

To better explain the meaning of the entries in the covariance matrix, various examples may be illustrated, as depicted in Figure 3.1. The covariance matrix, denoted as $\boldsymbol{\Sigma}$, is a symmetric, positive definite square matrix. Each off-diagonal element $\Sigma_{i,j}$ stands for the correlation between the random variables x_i and x_j. A value of $\Sigma_{i,j} = 0$ indicates that x_i and x_j are uncorrelated, while $\Sigma_{i,j} \neq 0$ suggests a correlation between the two variables; the higher the value of $\Sigma_{i,j}$, the stronger the correlation between the random variables. $\Sigma_{i,i}$ is associated with the standard deviation of x_i. Therefore, the greater the value of $\Sigma_{i,i}$, the less knowledge or equivalently the greater the uncertainty we have about the variable x_i.

Gaussian distribution is said to be closed under conditioning, marginalization and summation. Being closed means that the resulting distribution from these operations is also Gaussian. Usually, it is said: *"Once Gaussian always Gaussian"*.

To explain some properties it is convenient to split the variable $\boldsymbol{x}$, the mean $\boldsymbol{\mu}$ and the covariance $\boldsymbol{\Sigma}$

$$\boldsymbol{x} = \begin{bmatrix} \boldsymbol{x_a} \\ \boldsymbol{x_b} \end{bmatrix};\ \boldsymbol{\mu} = \begin{bmatrix} \boldsymbol{\mu_a} \\ \boldsymbol{\mu_b} \end{bmatrix};\ \boldsymbol{\Sigma} = \begin{bmatrix} \boldsymbol{\Sigma_{aa}} & \boldsymbol{\Sigma_{ab}} \\ \boldsymbol{\Sigma_{ba}} & \boldsymbol{\Sigma_{bb}} \end{bmatrix} \tag{3.4}$$

The properties of the distribution are:

1. Normalization:
$$\int P(\boldsymbol{x};\boldsymbol{\mu},\boldsymbol{\Sigma})d\boldsymbol{x} = 1 \tag{3.5}$$

2. Marginalization
$$P(\boldsymbol{x_a}) = \int_{\boldsymbol{x_b}} P(\boldsymbol{x_a},\boldsymbol{x_b};\boldsymbol{\mu},\boldsymbol{\Sigma})d\boldsymbol{x_b} \tag{3.6}$$
$$P(\boldsymbol{x_b}) = \int_{\boldsymbol{x_a}} P(\boldsymbol{x_a},\boldsymbol{x_b};\boldsymbol{\mu},\boldsymbol{\Sigma})d\boldsymbol{x_a} \tag{3.7}$$
$$\boldsymbol{x_a} \sim \mathcal{N}(\boldsymbol{\mu_a},\boldsymbol{\Sigma_a}) \tag{3.8}$$
$$\boldsymbol{x_b} \sim \mathcal{N}(\boldsymbol{\mu_b},\boldsymbol{\Sigma_b}) \tag{3.9}$$

3. Summation: If $\boldsymbol{x} \sim \mathcal{N}(\boldsymbol{\mu},\boldsymbol{\Sigma})$ and $\boldsymbol{x'} \sim \mathcal{N}(\boldsymbol{\mu'},\boldsymbol{\Sigma'})$
$$\boldsymbol{x} + \boldsymbol{x'} \sim \mathcal{N}(\boldsymbol{\mu} + \boldsymbol{\mu'},\boldsymbol{\Sigma} + \boldsymbol{\Sigma'}) \tag{3.10}$$

4. Conditioning: It returns the probability of $\boldsymbol{x_a}$ given the $\boldsymbol{x_b}$.
$$P(\boldsymbol{x_a}|\boldsymbol{x_b}) \sim \mathcal{N}(\boldsymbol{\mu_a} + \boldsymbol{\Sigma_{ab}}\boldsymbol{\Sigma_{bb}}^{-1}(\boldsymbol{x_b} - \boldsymbol{\mu_b}), \boldsymbol{\Sigma_{aa}} - \boldsymbol{\Sigma_{ab}}\boldsymbol{\Sigma_{bb}}^{-1}\boldsymbol{\Sigma_{ba}}) \tag{3.11}$$
$$P(\boldsymbol{x_a}|\boldsymbol{x_b}) = \frac{P(\boldsymbol{x_a},\boldsymbol{x_b};\boldsymbol{\mu},\boldsymbol{\Sigma})}{\int_{\boldsymbol{x_a}} P(\boldsymbol{x_a},\boldsymbol{x_b};\boldsymbol{\mu},\boldsymbol{\Sigma})d\boldsymbol{x_a}} \tag{3.12}$$

   The first important consideration is that the covariance matrix resulting from conditioning is not influenced by the observed value. Conversely, the new mean value is affected by nearly all components except $\boldsymbol{\Sigma_{aa}}$.When variables are uncorrelated ($\boldsymbol{\Sigma_{ab}} = \boldsymbol{0}$), both the mean and covariance remain unaffected by any observation.

Marginalization and conditioning are closely related to Bayesian inference. For the sake of simplicity, we can explain the above property for $d = 2$. This simplification enhances intuition by facilitating direct coupling between understanding and observations. Therefore considering a vector $\boldsymbol{x}$
$$\boldsymbol{x} = \begin{bmatrix} x_a \\ x_b \end{bmatrix};\ \boldsymbol{\mu} = \begin{bmatrix} \mu_a \\ \mu_b \end{bmatrix} = \begin{bmatrix} 0 \\ 0 \end{bmatrix};\ \boldsymbol{\Sigma} = \begin{bmatrix} \Sigma_{aa} & \Sigma_{ab} \\ \Sigma_{ba} & \Sigma_{bb} \end{bmatrix} \tag{3.13}$$
Three different covariance matrices were investigated:
$$\boldsymbol{\Sigma}^{(a)} = \begin{bmatrix} 1 & 0 \\ 0 & 1 \end{bmatrix};\ \boldsymbol{\Sigma}^{(c)} = \begin{bmatrix} 1 & 0.3 \\ 0.3 & 1 \end{bmatrix};\ \boldsymbol{\Sigma}^{(e)} = \begin{bmatrix} 1 & 0.8 \\ 0.8 & 1 \end{bmatrix}; \tag{3.14}$$
Figure 3.1 illustrates the joint probability for each of the above cases.

For case (a), where the variables are uncorrelated, $P(x_b) = P(x_b|x_a)$ (see Figure 3.1(b)), showing that what happens to one variable doesn't affect the other.

In case (c), where x_a and x_b are mildly correlated, knowing system a contributes to a more confident belief in system b, as evident by a narrower probability distribution. The mean value of the conditioned system, $\mu_{b|a}$, is linearly related to x_a.

This relationship is further amplified in case (e), where a greater correlation translates to a better understanding of system b given a. A tighter distribution increases the confidence of finding the real value of x_b close to μ_b.

Now that we have defined the basic properties of multivariate Gaussian distributions, Gaussian Processes become straightforward. In a Gaussian process, every point is considered a random variable. The only remaining challenge is how to construct the mean and the covariance matrix.

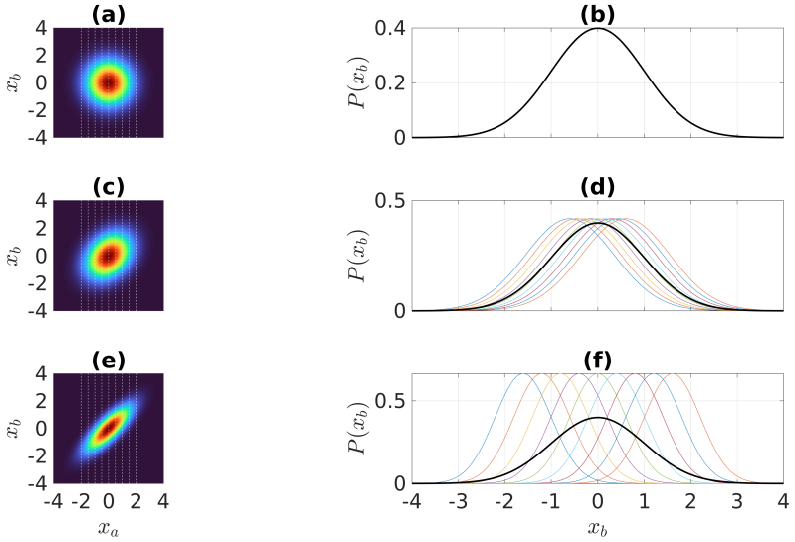

Figure 3.1: In the left column, the multivariate Gaussian distributions for three different covariance matrices are illustrated. On the right, the probability of x_b is presented. The black curve is associated with the univariate Gaussian distribution with $\sigma = \Sigma_{bb}$ and $\mu = \mu_b = 0$. The colored lines represent the conditioning probability of x_b given x_a. $P(x_b|x_a)$ is equivalent to sampling the multivariate Gaussian Distribution with a line of constant x_a. The sampling lines are the dotted white lines on the right

It is possible to simplify the expression of conditioning by setting the average to 0, which is a common practice. However, any arbitrary value can be chosen since it does not significantly impact the Gaussian Process (GP). On the other hand, building the covariance matrix $\mathbf{\Sigma}$ is the defining characteristic of the GP.

$\mathbf{\Sigma}$ is built from the covariance function, also known as the kernel of the GP. Different types of kernels exist, each suitable for fitting functions with certain characteristics. Understanding the geometric features of the fitted curve and choosing the kernel wisely can notably affect the regression process.

One of the most commonly used kernel functions is the Radial Basis Function kernel (RBF).

$$k_{RBF}(\boldsymbol{x}, \boldsymbol{x}') = \sigma_k^2 exp\left(-\frac{\|\boldsymbol{x} - \boldsymbol{x}'\|}{2l^2}\right) \tag{3.15}$$

The interpretation of the hyperparameter involved is simple. l sets the correlation length, meaning that the greater is l the more distance takes fot the correlation to fade out. If l is small two points close to each other are most probably very low correlated.

$$\Sigma_{i,j} = \sigma_k^2 exp\left(-\frac{\|\boldsymbol{x_i} - \boldsymbol{x_j}\|}{2l^2}\right) \tag{3.16}$$

$$\Sigma_{i,i} = \sigma_k^2 \tag{3.17}$$

It is clear now that the kernel function determines our prior belief regarding the function, taking into account our assumptions about the correlation length l and the uncertainty around the function values.

Marginalization and conditioning now come in handy. Calling $\boldsymbol{x_a}$ the testing points and $\boldsymbol{x_b}$ the sampling points, by conditioning the prior ($\boldsymbol{\mu} = 0$) with the sampling data we have the posterior probability:

$$P(\boldsymbol{x_a}|\boldsymbol{x_b}) \sim \mathcal{N}(\boldsymbol{\Sigma_{ab}}\boldsymbol{\Sigma_{bb}}^{-1}\boldsymbol{x_b}, \boldsymbol{\Sigma_{aa}} - \boldsymbol{\Sigma_{ab}}\boldsymbol{\Sigma_{bb}}^{-1}\boldsymbol{\Sigma_{ba}}) \tag{3.18}$$

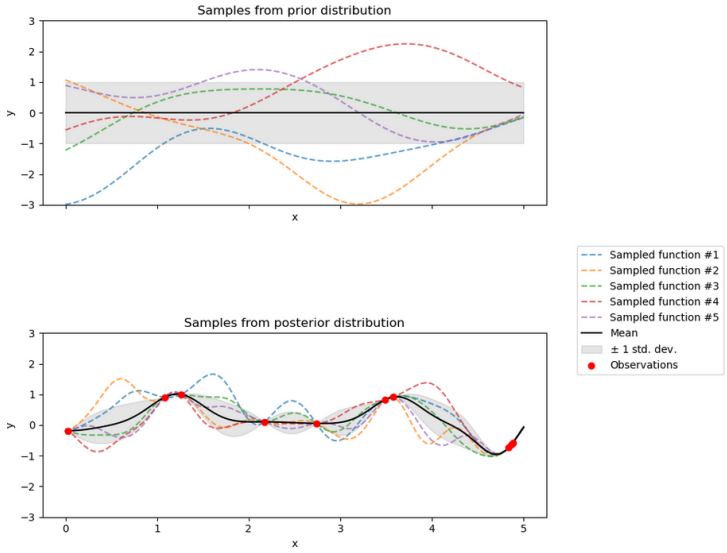

Figure 3.2: The figure above illustrates the prior distribution with some samples. The initial average value is set to zero, and the variance is homogeneous. Acquiring knowledge about the system, by points sampling, modifies both the mean and the standard deviation distributions depicted in the bottom figure.

3.3 Acquisition function

Given our belief about the objective function through the surrogate model, the next question to address is how to choose the next point where evaluate the function. Two strategies are available: exploration and exploitation.

Exploration focuses on discovering unknown regions of the design space, potentially leading to better solutions than those already found. Exploitation involves leveraging known information or exploiting regions of the design space believed to contain good solutions.

Both approaches have pros and cons. An exploration-oriented algorithm may be slow to converge while being overly focused on exploitation can lead to premature convergence.

An optimal search strategy dynamically adjusts the balance between exploration and exploitation. This adaptability allows the algorithm to explore new regions while also exploiting known information to converge efficiently toward the optimal solution.

During each iteration of the optimization process, an optimization policy examines the available data and selects a point where the next observation will be made. To accomplish this, another function called the acquisition function is introduced. The next point to evaluate the objective function is chosen to maximize the acquisition function.

Optimizing the objective function translates into subsequent maximization of the acquisition function, with one significant difference: while the objective function is known only at discrete points where it has been evaluated, the acquisition function is known everywhere in the domain and is much easier and less expensive to optimize.

There are numerous acquisition functions available, but three common ones include:

- Upper Confidence Bound (UCB);
- Probability of improvement (PI);
- Expected improvement (EI);

3.3.1 Upper Confidence Bound

The simplest acquisition function that can be built is the Upper Confidence Bound (UCB).

$$\alpha_{UCB}(x) = \mu(x) + \lambda\sigma(x) \tag{3.19}$$

By tuning λ is it possible to balance between exploration and exploitation.

3.3.2 Probability of Improvement

The fundamental idea is to focus on areas where there is the greatest potential for improving the objective function, regardless of the extent of the improvement.

Gaussian Process (GP) enables us to describe the function $f(x)$ in terms of normal distribution with a mean of μ and standard deviation of σ.

$$f(x) \sim \mathcal{N}(\mu(x), \sigma^2(x)) \tag{3.20}$$

This implies that f can assume different values, with some more likely than others.

Defining a new function $I(x)$ as:

$$I(x) = max(f(x) - f(x^*), 0) \tag{3.21}$$

$f(x^*)$ is the best solution found so far. $I(x)$ makes feasible the definition of the acquisition function $\alpha_{PI}(x)$:

$$\alpha_{PI}(x) = P(I(x) > 0) \tag{3.22}$$

Calling with z_0

$$z_0 = \frac{f(x^*) - \mu(x)}{\sigma(x)} \tag{3.23}$$

$$\alpha_{PI}(x) = P(f(x) > f(x^*)) = 1 - \Phi(z_0) = \Phi(-z_0) = \Phi\big(\frac{\mu(x) - f(x^*)}{\sigma(x)}\big) \tag{3.24}$$

Where $\Phi(z)$ is the cumulative distribution function.

It is possible to gain an understanding of the meaning of equation 3.24 by referring to Figure 3.3. Drawing a horizontal line at the level of $f(x^*)$, the next point to sample is the point with the most shaded region above the horizontal line. As depicted, near the sampled points where the uncertainty is close to zero, the acquisition function is also zero.

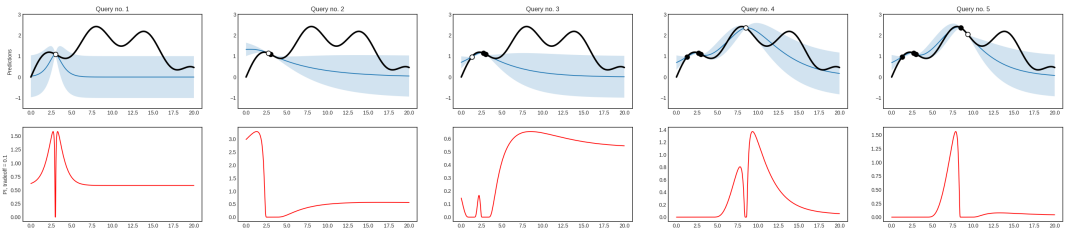

Figure 3.3: 5 steps of BO iterations with PI as acquisition function.

3.3.3 Expected improvement

It has been previously mentioned that PI accounts only for an improvement, not necessarily the best improvement. To take into account also the magnitude of this improvement, a modification of the acquisition function is required.

$$\alpha_{EI}(x) = \mathbb{E}[I(x)] = \int_{-\infty}^{+\infty} I(x)\varphi(z)dz \tag{3.25}$$

Where $\varphi(z)$ is the normal distribution $\varphi(z) \sim \mathcal{N}(0,1)$.

$$\varphi(z) = \frac{1}{\sqrt{2\pi}} exp\left(-\frac{z^2}{2}\right) \tag{3.26}$$

$$\alpha_{EI}(x) = \int_{-\infty}^{+\infty} max(f(x) - f(x^*), 0)\varphi(z)dz \tag{3.27}$$

Exploiting the additive integral properties:

$$\alpha_{EI}(x) = \underbrace{\int_{-\infty}^{z0} max(f(x) - f(x^*), 0)\varphi(z)dz}_{since\ I(x) = 0} \overset{=0}{\rightarrow} + \int_{z0}^{+\infty} max(f(x) - f(x^*), 0)\varphi(z)dz$$

$$\alpha_{EI}(x) = \int_{-\infty}^{z0} (f(x) - f(x^*))\varphi(z)dz \tag{3.28}$$

Recalling that $f(x)$ can be expressed as $f(x) = \mu(x) + \sigma(x)z$, after some algebraic manipulations

$$\alpha_{EI}(x) = \underset{(1)}{(\mu(x) - f(x^*))\Phi\left(\frac{\mu(x) - f(x^*)}{\sigma(x)}\right)} + \underset{(2)}{\sigma(x)\varphi\left(\frac{f(x^*) - \mu(x)}{\sigma(x)}\right)} \tag{3.29}$$

The interpretation of the above equation is crucial to understand the essence of the expected improvement policy. EI assumes high values when:

- $\mu(x) \gg f(x^*)$ because the first term (1) equation 3.29 is the product between two monotonic function of $\mu(x) - f(x^*)$. It is also important that the uncertainty σ is low because for a fixed $(\mu(x) - f(x^*))$, $\Phi\left(\frac{\mu(x) - f(x^*)}{\sigma(x)}\right)$ increases as $\sigma(x)$ decreases.

- The mean value is close to the best found up to that iteration $\mu(x) \simeq f(x^*)$ and the standard deviation σ is high. Under this circumstance term (1) is close to zero, but φ is close to its maximum value (bell curve with a maximum close to the mean). Therefore the second term (2) rules the equation 3.29 since it is the product between σ and φ.

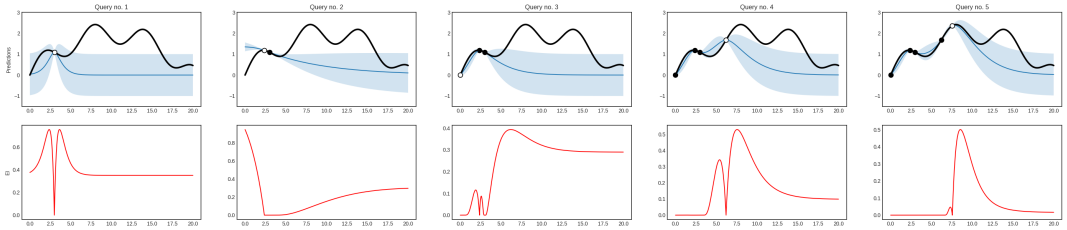

Figure 3.4: 5 steps of BO iterations with EI as acquisition function.

3.4 High dimensional data post-processing: classical Multi Dimensional Scaling (cMDS)

As data structures become increasingly complex, new techniques are needed to interpret the gathered information. In recent years, dimensional reduction techniques have gained popularity due to their ability to represent data in lower dimensions (typically 2D or 3D) while preserving the key intrinsic characteristics of the original data [23].

MDS offers a valuable advantage by representing complex data structures as geometrical images, making it an effective tool for data visualization. One of its many applications is identifying quantitative or qualitative similarities among points within a dataset [37]. For example, in 1968, 18 students were asked to rate the similarities between various countries. An MDS analysis (depicted in figure 3.5) revealed the unconscious criteria that influenced the students' judgments. As shown in the figure, two lines can be drawn that divide the countries based on two criteria: developed vs. developing nations and pro-Western vs. pro-Communist countries. Countries within the same quarter marked by the dotted line share the same two characteristics.

While it is feasible to define similarity or dissimilarity qualitatively, like in the previous example, engineering applications focus heavily on quantitative comparisons. Additionally, if the data belong to Euclidean space, classical Multidimensional Scaling (MDS) proves suitable for dimensional scaling. Within Euclidean space, dissimilarity is quantified by the distance between two points, while similarity is assessed via the inner product.

The task of MDS can be summarized as follows: given a data set $\mathscr{H} = \{\boldsymbol{x_1}, ..., \boldsymbol{x_n}\} \in \boldsymbol{\chi} \subset \mathbb{R}^D$ find an embedding $F : \boldsymbol{\chi} \to \mathbb{R}^d$ with $d \leq D$ such that

$$\|\boldsymbol{x_i} - \boldsymbol{x_j}\| = \|F(\boldsymbol{x_i}) - F(\boldsymbol{x_j})\| \tag{3.30}$$

This statement ensures that the Euclidean distance between any pair of original data points $\boldsymbol{x_i}$ and $\boldsymbol{x_j}$ is preserved in the lower-dimensional space defined by $F(\boldsymbol{x})$.

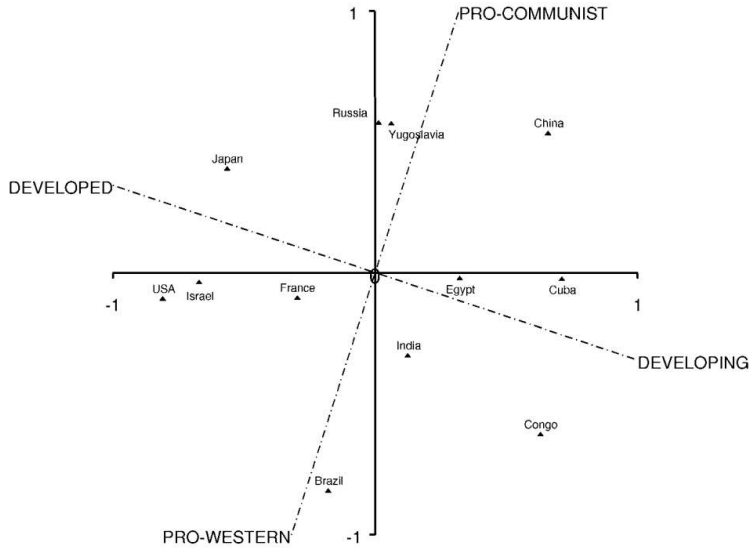

Figure 3.5: Similarity and dissimilarities among countries, deduced from a questionnaire, after MDS

3.4.1 cMDS

Defining the Euclidean distance between two points $\boldsymbol{a}$ and $\boldsymbol{b}$ with $\boldsymbol{a}, \boldsymbol{b} \in \mathbb{R}^D$ as

$$d_2(\boldsymbol{a}, \boldsymbol{b}) = \|\boldsymbol{a} - \boldsymbol{b}\| = \sqrt{\sum_{k=1}^{D} (a_k - b_k)^2} \tag{3.31}$$

Given the data set $\mathscr{H} = \{\boldsymbol{x_1}, ..., \boldsymbol{x_n}\} \in \boldsymbol{\chi} \subset \mathbb{R}^D$ the inter-points distance matrix is defined

$$\boldsymbol{D} = [D_{ij}] = [d_2(\boldsymbol{x_i}, \boldsymbol{x_j})] \tag{3.32}$$

And the Euclidean square distance matrix

$$\boldsymbol{S} = \left[d_2^2(\boldsymbol{x_i}, \boldsymbol{x_j})\right] \tag{3.33}$$

The distance between two points remains invariant under shifting and rotation of the frame of reference. Consequently, the matrices $\boldsymbol{D}$ and $\boldsymbol{S}$ are symmetric and also invariant to rotation and shifting. These matrices serve as measures of dissimilarities between points, whereas similarities can be gauged using the inner product.

$$\langle \boldsymbol{a}, \boldsymbol{b} \rangle = \sum_{k=1}^{D} a_k b_k \tag{3.34}$$

The inner products of the points within the data set $\mathscr{H}$ are stored in $\boldsymbol{G}$, which represents the Gram matrix.

$$\boldsymbol{G} = [G_{ij}] = [\langle \boldsymbol{x_i}, \boldsymbol{x_j} \rangle] \tag{3.35}$$

Using the law of cosine a relation between the distance matrix and the Gramm Matrix can be found:

$$D_{ij} = \sqrt{G_{ii} + G_{jj} - 2G_{ij}} \tag{3.36}$$

The Gram matrix is not shifting invariant. To establish a stronger and more stable relationship between $\boldsymbol{G}$ and $\boldsymbol{D}$, it is advantageous to choose a frame of reference such that the origin coincides with the center of $\mathscr{H}$.

$$\overline{\boldsymbol{x}} = \frac{1}{n}\sum_{i=1}^{n} \boldsymbol{x_i} \tag{3.37}$$

The hat denotes the vector in a centered frame of reference $\hat{\boldsymbol{x_i}} = \boldsymbol{x_i} - \overline{\boldsymbol{x}}$ and $\hat{\mathscr{H}}$ is the *center data set*. If we denote with $\boldsymbol{X}$ a data matrix which columns are the data $\boldsymbol{x_i}$

$$\boldsymbol{X} = [\boldsymbol{x_1}, ..., \boldsymbol{x_n}] \tag{3.38}$$

It is possible to go from $\boldsymbol{X}$ to $\hat{\boldsymbol{X}} = [\hat{\boldsymbol{x_1}}, ..., \hat{\boldsymbol{x_n}}]$ by a matrix multiplication

$$\hat{\boldsymbol{X}} = H\boldsymbol{X} \tag{3.39}$$

Where H is known as the centering matrix:

$$\boldsymbol{H} = \boldsymbol{I} - \frac{1}{n}\boldsymbol{E} \tag{3.40}$$

$\boldsymbol{I}$ is the identity matrix and $\boldsymbol{E}$ is a matrix filled with one ($E_{ij} = 1$). Similarly, the Gram matrix expressed in a centered frame of reference $\boldsymbol{G^c}$

$$\boldsymbol{G^c} = \boldsymbol{HGH} \tag{3.41}$$

Euclidian square distance Matrix $\boldsymbol{S^c}$ and the centering Gram matrix $\boldsymbol{G^c}$ are related by the following equation

$$\boldsymbol{G^c} = -\frac{1}{2}\boldsymbol{S^c} \tag{3.42}$$

It can be proven that if $\boldsymbol{G^c}$ has rank r, then there exists a centered vector set $\mathscr{Y} = \boldsymbol{y_1}, ..., \boldsymbol{y_n} \subset \mathbb{R}^r$ such that

$$d_2(\boldsymbol{x_1}, \boldsymbol{x_2}) = d_2(\boldsymbol{y_1}, \boldsymbol{y_2}) \tag{3.43}$$

This implies that it is possible to represent the data set in a low-dimensional space without altering the inter-point distances if the embedded space has a dimension larger or equal to r. However, if $r \gg 3$, visualizing the data set remains challenging, and thus, no substantial benefits can be drawn from this transformation. At times, we must compromise the need for visualization by forgoing the exact representation of the inter-point distances. When $\mathscr{Y} = \{\boldsymbol{y_1}, ..., \boldsymbol{y_n}\} \subset \mathbb{R}^d$ with $d < r$, inevitably

$$d_2(\boldsymbol{x_1}, \boldsymbol{x_2}) \neq d_2(\boldsymbol{y_1}, \boldsymbol{y_2}) \tag{3.44}$$

To measure how distorted is the embedded space, compared with the original space, a loss function $\eta(\mathscr{Y})$ is introduced:

$$\eta(\mathscr{Y}) = \sum_{i=1}^{n}\sum_{j=1}^{n}\left(d_2^2(\boldsymbol{x_1}, \boldsymbol{x_2}) - d_2^2(\boldsymbol{y_1}, \boldsymbol{y_2})\right) \tag{3.45}$$

It is evident that the loss function must be minimized to reduce the distance distortion introduced by reducing the dimension of the data set. Therefore, denoting $\boldsymbol{Y} = [\boldsymbol{y_1}, ..., \boldsymbol{y_n}]$ as the reduced data set, $\boldsymbol{Y}$ is the solution of the optimization problem when:

$$\boldsymbol{Y} = \arg\left[\min \eta\left(\mathscr{Y}\right)\right] \tag{3.46}$$

For classical Multidimensional Scaling (cMDS), it can be proven that the solution to the minimization problem is given by the spectral decomposition of the Gram matrix. Let $\lambda_1, \lambda_2, ..., \lambda_d$ denote the d largest eigenvalues of the Gram matrix $\boldsymbol{G}$, and $\boldsymbol{u_1}, \boldsymbol{u_2}, ..., \boldsymbol{u_d}$ represent the corresponding eigenvectors. These eigenvalues and eigenvectors are collected in two matrices.

$$\boldsymbol{\Lambda}_d = \left[\sqrt{\lambda_i}\delta_{ij}\right] \tag{3.47}$$

$$\boldsymbol{U}_d = [\boldsymbol{u_1}, \boldsymbol{u_2}, ..., \boldsymbol{u_d}] \tag{3.48}$$

$$\boldsymbol{Y} = \boldsymbol{\Lambda}_d \boldsymbol{U'}_d \tag{3.49}$$

$\boldsymbol{\Lambda}_d \in \mathbb{R}^{d\times d}$, $\boldsymbol{U}_d \in \mathbb{R}^{n\times d}$, $\boldsymbol{Y}_d \in \mathbb{R}^{d\times n}$ and δ_{ij} Kronecker delta.

A closed formulation of the loss function is also available for cMDS:

$$\eta\left(\mathscr{Y}\right) = \sum_{i=d+1}^{r} \sigma_i^2 \tag{3.50}$$

Where σ_i is obtained by the Singular Value Decomposition SVD of the Matrix $\hat{\boldsymbol{X}}$.

$$\hat{\boldsymbol{X}} = \boldsymbol{V}\boldsymbol{\Sigma}^*\boldsymbol{W} \tag{3.51}$$

$\boldsymbol{\Sigma}^* = [\sigma_i\delta_{ij}]$, $\sigma_i > \sigma_j$ $i, j = 1, ..., r$ and $i < j$

Chapter 4

Numerical Set-up

This chapter is dedicated to presenting the numerical tools employed for the subsequent calculations. The numerical framework comprises four blocks in series, meaning that the output of one block serves as the input for the next, as figure 4.1 shows.

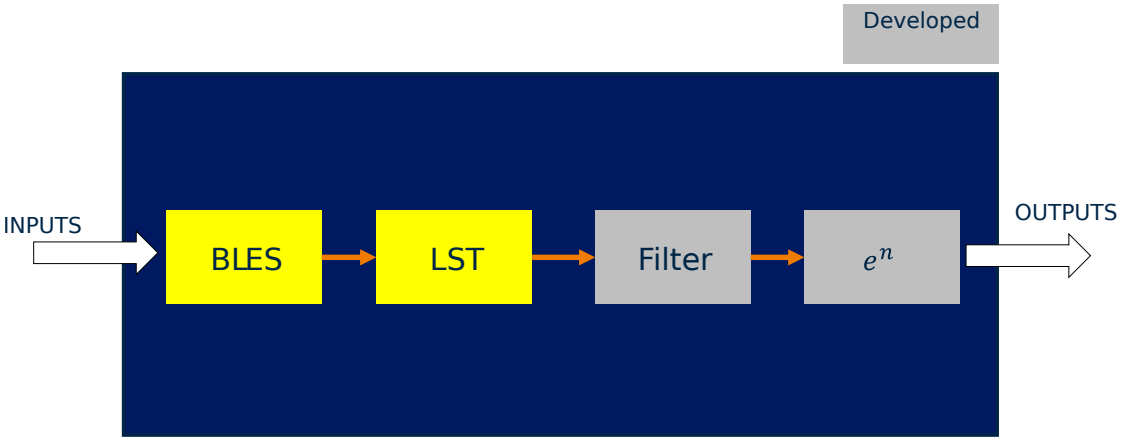

Figure 4.1: Blocks for computing the transition location. BLES computes the velocity fields, LST uses them as input to solve the OR equation. The filter selects the dominant roots while e^N is the transition prediction method selected to estimate the transition point.

4.1 Boundary Layer Equation Solver BLES

It is invoked to solve the boundary layer equations described in the previous chapter. BLES takes as input:

- Geometry: This includes the height of the computational domain (H) and the length of the plate (L).
- Number of grid points: N_x grid points in the stream-wise (x) direction and N_y grid points in the wall-normal (y) direction, resulting in a total of $N_x \times N_y$ nodes.
- Boundary conditions:

- Inflow BC. It starts the marching from a Falker-Skan velocity profile with an equivalent Hartree parameter to the local external velocity;
- Wall boundary condition: No-slip velocity ($u(x, y = 0) = 0$) is enforced, with an option for a permeable wall to implement suction ($v(x, y = 0) = v_w$).
- BL edge boundary condition: $U_e(x)$ is obtained from external or inviscid calculations.

- Fluid properties: Kinematic viscosity (ν) and fluid density (ρ);
- Free stream velocity: U_∞

The outputs include the velocity field and its derivatives up to the second order. The main quantities of interest are u, v, $\frac{\partial u}{\partial y}$, and $\frac{\partial^2 u}{\partial y^2}$.

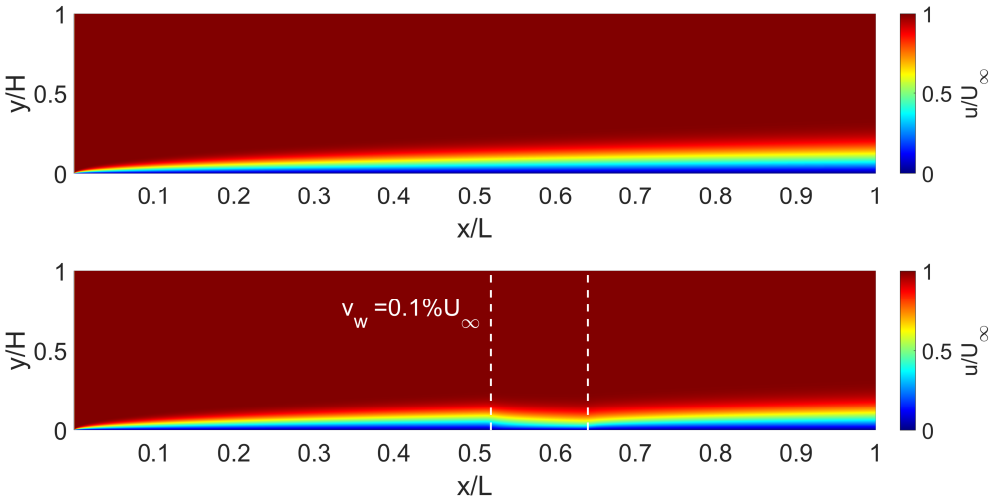

Figure 4.2: Output of BLES. The dotted lines define the boundary of the suction region while the suction velocity is illustrated in the figure below and it is equal to 0.1% of the free stream velocity.

In the y direction, the grid points feature a Chebyshev distribution, while in the x direction, the grid is equally spaced. The scheme in the y direction is N_y^{th} order accurate, whereas, in the x direction, it is only second-order accurate. The nonlinear momentum equation is solved using a simple algorithm, with an implemented check for laminar separation inside the code. An example of the BLES velocity field is shown in Figure 4.2, where the x component u of the velocity is represented. The boundary layer (BL) is identified as the region where colors change rapidly, indicating high-velocity gradients. In the top figure, a natural boundary layer evolution is depicted, while the bottom figure illustrates the effect of suction. In the region where suction is applied, there is a noticeable reduction in the BL thickness or a local acceleration of the flow.

4.2 Linear Stability Theory (LST) solver method

The Orr-Sommerfeld equation is commonly used to study the hydrodynamic stability. It is a nonlinear eigenvalue equation in the parameter α. Mathematically, this parameter represents the

eigenvalue of the OS equation, while from a physical standpoint, it denotes the wavenumber of the perturbation under consideration. To solve nonlinear eigenvalue problems, two main methods have been developed over the years. The first is the "shooting method" with ortho-normalization, as described by Keller [19]. This method is effective when a good initial approximation of the solution is available, and it involves an iterative algorithm to integrate the approximated solution over the entire domain until the boundary conditions coincide with those imposed. However, the convergence of this method heavily depends on the quality of the initial estimate.

In situations where such an estimate is unavailable, the method introduced by Bridges and Morris [5], commonly known as the companion matrix method, is preferred. This method is, in fact, independent of the initial solution estimate. As our code implements this method, we will proceed with a detailed description.

Firstly, it is essential to discretize the eigenfunctions by utilizing Chebyshev nodes. This initial step is imperative in approximating the differential operators through matrix-vector products - a crucial aspect in the progression of the solving methodology. By utilizing a spectral approach, the accuracy of the approximate solution is further improved, surpassing the less precise finite differences method. Let us now delve into the Orr-Sommerfeld equation.

$$\begin{cases} \left(\left(\frac{d^2}{dy^2} - \alpha^2 \right)^2 - i\,Re \left[(\alpha U - \omega) \left(\frac{d^2}{dy^2} - \alpha^2 \right) - \alpha U'' \right] \right) \phi = 0 \\ \phi = 0 \ ; \ y = 0, y \to \infty \\ \phi' = 0 \ ; \ y = 0, y \to \infty \end{cases} \tag{4.1}$$

Observing equation (4.1), one notices the increased complexity associated with the spatial approach compared to the temporal approach. While the temporal approach treats the Orr-Sommerfeld equation as a linear eigenvalue equation in ω, the spatial approach delves into the spatial evolution of disturbances characterized by given frequencies ω, resulting in a nonlinear eigenvalue equation in the eigenvalues α. In this spatial context, the appearance of α with a fourth power adds difficulties in the solution process, making it non-trivial.

The companion matrix method is applied having first discretized the coordinate y by introducing Chebyshev nodes.

$$\eta_j = cos((j-1)\frac{\pi}{N_c - 1}) \ ; \ -1 \leq \eta \leq 1 \ ; \ j = 1, 2, ...N_c; \tag{4.2}$$

With N_c the number of Chebichev nodes. Since the coordinate y is upper-unbounded, a transformation capable of mapping the interval [0, y_∞] to [-1, 1] is required. Motsa and Makukula have proposed the following transformation [26]:

$$y = y_\infty \frac{1+\eta}{2} \tag{4.3}$$

The function ϕ can be approximated using Chebyshev polynomials $T_k(\eta)$.

$$\phi(\eta) = \sum_{k=0}^{N} a_k T_k(\eta) \tag{4.4}$$

with

$$a_k(\eta) = \frac{2}{N b_k} \sum_{m=0}^{N} \frac{1}{b_m} T_k(\eta_m) \phi(\eta_m) \tag{4.5}$$

$$\begin{cases} b_k = 1 \quad k = 1, 2, ..., N_c - 1 \\ b_0 = b_N = 2 \end{cases} \tag{4.6}$$

Having placed the nodes according to the Chebyshev distribution, it becomes possible to express derivatives using the Chebyshev differentiation matrix, which possesses a well-known structure.

$$\boldsymbol{\phi^{(1)}} = \boldsymbol{D}\boldsymbol{\phi} \tag{4.7}$$

$$\boldsymbol{\phi^{(2)}} = \boldsymbol{D^{(2)}}\boldsymbol{\phi} \tag{4.8}$$

The derivatives in equation (4.1) are with respect to y, whereas the differentiation matrices express derivatives with respect to the variable η. It is necessary to rescale the derivatives before discretizing them with the differentiation matrices.

$$\frac{d\phi}{dy} = \frac{d\phi}{d\eta}\frac{d\eta}{dy} = \frac{2}{y_\infty}\frac{d\phi}{d\eta} \tag{4.9}$$

By introducing $\tilde{\boldsymbol{D}}$

$$\tilde{\boldsymbol{D}} = \frac{2}{y_\infty}\boldsymbol{D} \tag{4.10}$$

$$\left(\left(\tilde{\boldsymbol{D}^2} - \alpha^2\boldsymbol{I}\right)^2 - i\,Re\left[(\alpha U\boldsymbol{I} - \omega\boldsymbol{I})\left(\tilde{\boldsymbol{D}^2} - \alpha^2\boldsymbol{I}\right) - \alpha U''\boldsymbol{I}\right]\right)\boldsymbol{\phi} = 0 \tag{4.11}$$

Rearranging and grouping the terms appropriately, we get:

$$\boldsymbol{C_4}\alpha^4 + \boldsymbol{C_3}\alpha^3 + \boldsymbol{C_2}\alpha^2 + \boldsymbol{C_1}\alpha + \boldsymbol{C_0} = 0 \tag{4.12}$$

$$\begin{cases} \boldsymbol{C_4} &= \boldsymbol{I} \\ \boldsymbol{C_3} &= iReU\boldsymbol{I} \\ \boldsymbol{C_2} &= -(i\omega Re\boldsymbol{I} + 2\tilde{\boldsymbol{D}^2}) \\ \boldsymbol{C_0} &= \tilde{\boldsymbol{D}^4} + iRe\omega\tilde{\boldsymbol{D}^2} \end{cases} \tag{4.13}$$

All matrices are of size $N_c \times N_c$.

The roots of Equation (4.12) are the eigenvalues of the companion matrix introduced by Bridges and Morris.

$$\left[\begin{pmatrix} -\boldsymbol{C_1} & -\boldsymbol{C_2} & -\boldsymbol{C_3} & -\boldsymbol{C_4} \\ \boldsymbol{I} & \boldsymbol{0} & \boldsymbol{0} & \boldsymbol{0} \\ \boldsymbol{0} & \boldsymbol{I} & \boldsymbol{0} & \boldsymbol{0} \\ \boldsymbol{0} & \boldsymbol{0} & \boldsymbol{I} & \boldsymbol{0} \end{pmatrix} - \alpha\begin{pmatrix} -\boldsymbol{C_0} & \boldsymbol{0} & \boldsymbol{0} & \boldsymbol{0} \\ \boldsymbol{I} & \boldsymbol{0} & \boldsymbol{0} & \boldsymbol{0} \\ \boldsymbol{0} & \boldsymbol{0} & \boldsymbol{I} & \boldsymbol{0} \\ \boldsymbol{0} & \boldsymbol{0} & \boldsymbol{0} & \boldsymbol{I} \end{pmatrix}\right]\begin{pmatrix} \alpha^3\phi \\ \alpha^2\phi \\ \alpha\phi \\ \phi \end{pmatrix} = \begin{pmatrix} 0 \\ 0 \\ 0 \\ 0 \end{pmatrix} \tag{4.14}$$

4.2.1 LST solver

The method utilized by the solver and described in the previous paragraph requires dimensionless variables and parameters as input. These variables are denoted with a star $(\cdot)^*$ to distinguish them from their dimensional counterparts. The following quantities are the required inputs:

- $Re = \frac{U_e(x)\delta_1(x)}{\nu}$: The Reynolds number at station x where stability is evaluated. Here, δ_1 represents the displacement thickness while U_e denotes the velocity outside the boundary layer.
- $u^*(x,y) = \frac{u(x,y)}{U_e(x)}$: the velocity profile normalized by the external velocity.
- $\left(\frac{d^2U(x,y)}{dy^2}\right)^* = \frac{d^2U(x,y)}{dy^2}\frac{\delta_1^2(x)}{U_e(x)}$: the second derivative of the velocity profile with respect to y, normalized accordingly.

- $y^* = \frac{y}{\delta_1(x)}$: the normalized y coordinate.
- $\omega^* = \frac{\omega \delta_1(x)^2}{U_e(x)}$: the dimensionless disturbance frequency.

The solver will provide a set of N_c eigenvectors stored in a $(N_c \times N_c)$ matrix. Each vector is associated with its dimensionless eigenvalue. The value of N_c is equal to the size of the vector y i.e. N_c is the number of Chebyshev grid points.

Some of the solutions obtained may be deemed spurious, representing purely numerical artifacts devoid of any physical significance. Among the N_c solutions, only a subset will be compatible with the velocity perturbation inside the boundary layer, which we refer to as physical solutions. To apply the e^N method effectively, we require only the dominant root, corresponding to the wave number associated with the least damped stable mode or the most amplified unstable mode. It becomes evident from this discussion that a filtering process is necessary, initially to distinguish between numerical and physical solutions, and subsequently to select the most relevant physical solution for the transition.

4.3 Filter

In order to assess the velocity profile stability, it is necessary to couple the solver with a filtering function at least for discarding spurious solutions.

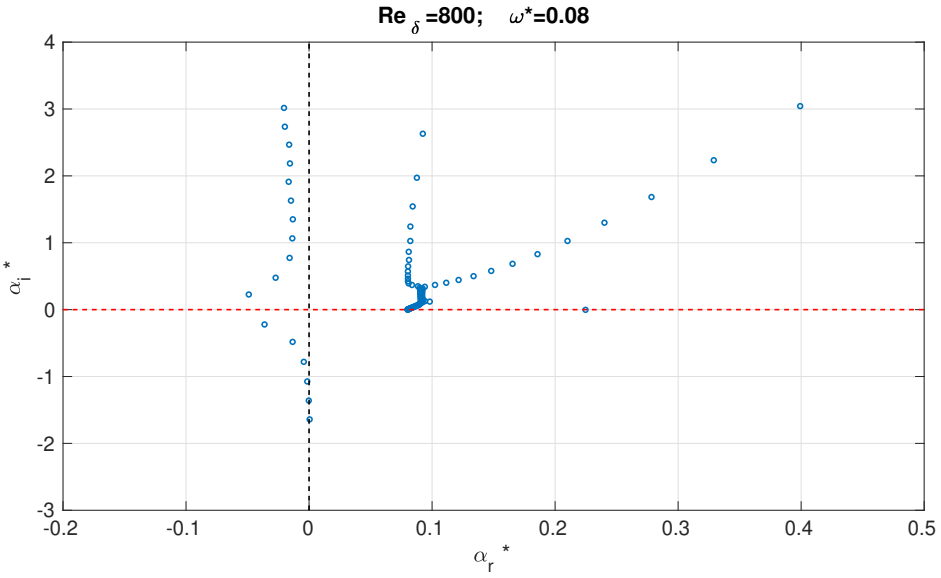

Figure 4.3: Spectrum of Blasius profile with $Re_{\delta_1} = 800$, $\omega^* = 0.08$ and $N_c = 100$. The vertical line divides upstream and downstream traveling perturbations, while the horizontal line splits the spectrum into stable and unstable modes

To begin, it's important to choose the eigenvalues with real parts greater than zero, $\alpha_r^* > 0$. The real part of the eigenvalue is directly connected to the phase velocity c_r^*. $\alpha_r^* >$ implies that $c_r^* > 0$, causing perturbations to move from the leading edge to the trailing edge of the flat plate. Figure 4.3 illustrates this concept, with the spectrum divided by a vertical line into

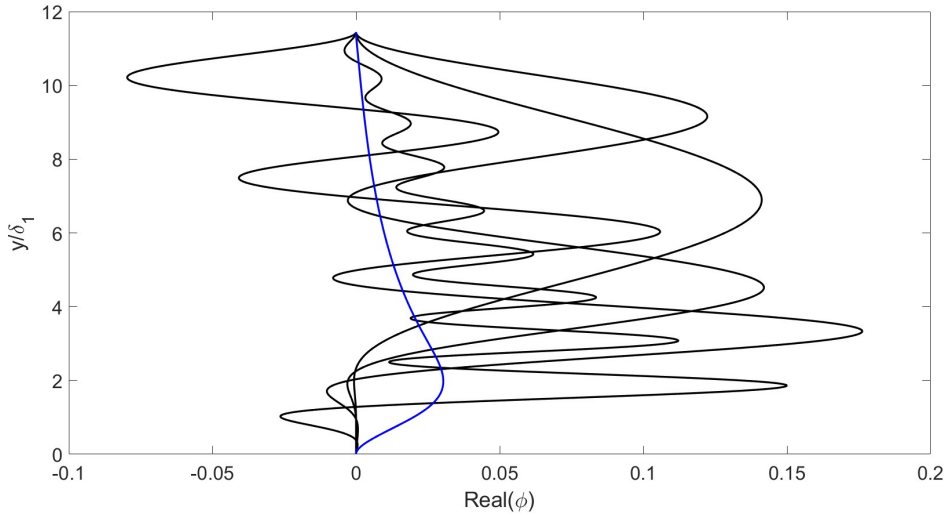

Figure 4.4: Figure shows the real part of 5 out of the N_c eigenfunctions that LST provides. The black curves are spurious solutions, the blue curve corresponds to the physical solution.

downstream-traveling perturbations on the right and upstream-traveling perturbations on the left.

The filter method originally implemented was based on cross-correlations between the eigenvector from the LST and a base reference function. However, this cross-correlation filter carries two disadvantages:

- The effectiveness of the method heavily relies on the choice of the base shape utilized in cross-correlations. When tested against various Falkner-Skan profiles, the method failed in most cases, particularly when the Hartree parameter deviated from zero (a value that corresponds to the flow for which the base reference function is computed).
- The cross-correlation operation is computationally expensive. For accurate stability analyses the stability of a substantial number of profiles is reviewed, and tested against perturbations densely spread inside a broad frequency range. Looking at the stability plane, the above statement immediately translates into having a very fine grid that discretizes $Re_{\delta_1} - \omega$ space. The other parameter that operates is the number of Chebyschev nodes directly involved in the OS equation. It is obvious that once accuracy is required the filtering process becomes time demanding, up to the point when it is as expensive as the LST solver. The next example will provide a direct perception of how things can escalate in a blink of an eye. Suppose stability curves are desired over an evenly spaced interval of Reynolds numbers ranging from $400 \leq Re \leq 3000$ and frequencies ranging from 50 to 400 rad/s, typical values for a flat plate, with N_{Re} and N_ω points used to discretize these intervals, respectively. The number of cross-correlations performed is $N_c \times N_{Re} \times N_\omega$. For instance, using $N_c = 100$, $N_{Re} = 100$, and $N_\omega = 100$, the number of cross-correlations to be performed is on the order of a million.

Therefore, efforts were made to address these difficulties by creating a filter that leverages the geometric properties of eigenfunctions, aiming to be independent of any base shape and thus assume a universal validity.

Among the N_c solutions from the stability solver, the filter's task is to select only the correct eigenvalue. Observing eigenfunctions across various spectra led to the conclusion physical solutions:

- Exhibit one and only one maximum of $Real(\phi)$ for $y/\delta_1 < 3$.
- Have $Real(\phi) > 0$.

To give a hint about what the real part of the eigenvectors, directly taken from LST, could possibly look like, some of them (5 out of the 98 eigenvalues) are shown in figure 4.4. It is evident that, among those depicted, there is only one physical that is colored in blue. For the sake of clarity, each group of N_c modes has more than one physical solution.

This paradigm shift, from cross correlations to eigenfunctions geometrical characteristics, allowed the filter to be 10 times faster than the original one. However, challenges arise when ω drops too low. In this scenario, the shape of the eigenfunction deviates from the classical one, and wiggling in the eigenfunctions begins to occur, giving a hard time for the filter to operate.

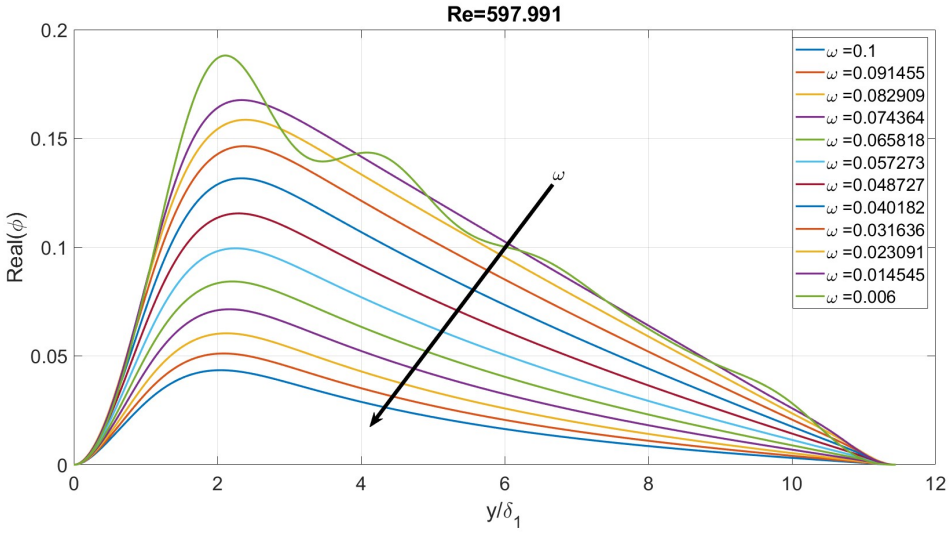

Figure 4.5: Eigenfunctions associated with different value of ω for $Re_{\delta_1} \simeq 598$. The one with the lowest angular frequency shows some wrinkles.

Generally speaking, the geometrical filter can always be applied when the point we query for stability lies inside the unstable region of the stability map. When we step outside of the unstable region, the geometrical filter may fail. In this case, a cross correlation is used. Since for one Re_{δ_1}, or equivalently x station, the stability of multiple modes is investigated it is possible to combine both approaches. Indicating with

$$\omega_{LB} = \arg\left[\min_{\omega}\left(\alpha_i(\omega, Re_{\delta_1}) = 0\right)\right] \tag{4.15}$$

LB stands for Lower Branch and Re_{δ_1} is fixed.

$$\begin{cases} \omega \geq \omega_{LB}; & Geometrical\ filter\ works \\ \omega < \omega_{LB}; & Geometrical\ filter\ may\ not\ work \end{cases} \tag{4.16}$$

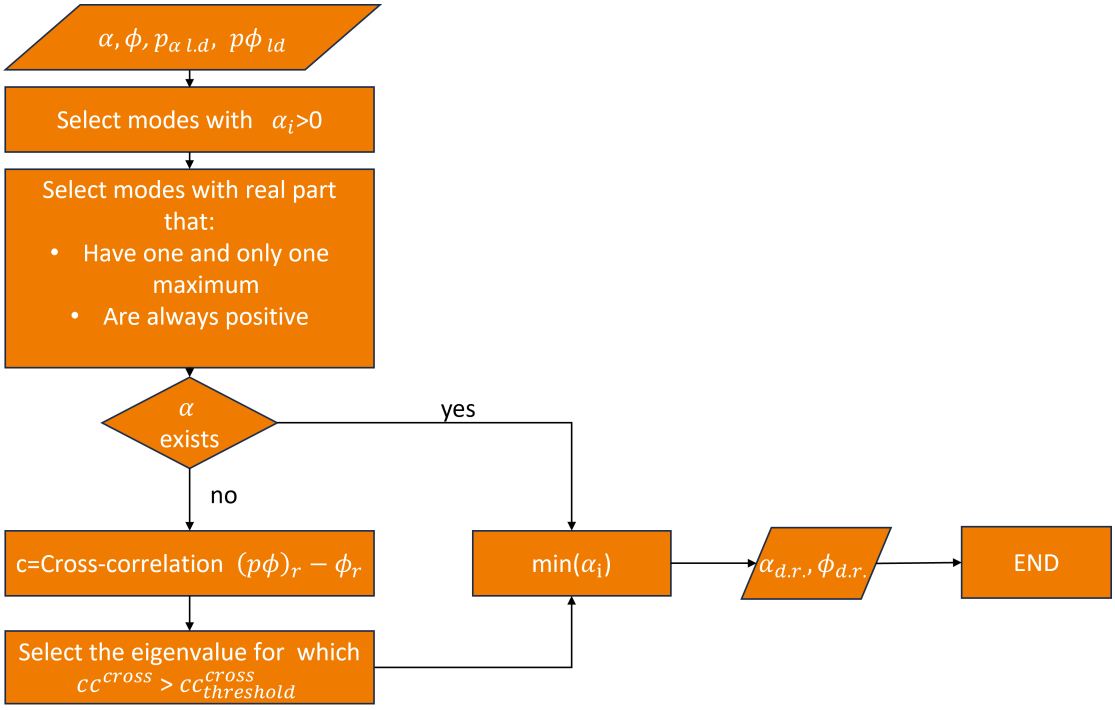

Figure 4.6: Flow chart that summarizes the filtering operations

The strategy applied for the filter is explained in figure 4.6. Given a velocity profile and a set of angular frequencies

$$\boldsymbol{\omega^*} = [\omega_1^*, \omega_2^*, ..., \omega_{N_\omega}^*]; \quad \omega_i^* > \omega_j^*, \ i > j, \ 1 \leq i, j \leq N_\omega \tag{4.17}$$

The filter starts to analyze the modes with the highest angular frequency to be sure that the application of the geometrical filter is feasible. For each current ω_i, it stores the eigenfunction associated with the dominant root (the letter p ahead of α and ϕ means previous). When the filter moves to the following angular frequency, it starts applying the geometrical filter. If a solution is found the eigenfunction and eigenvalue stored are updated. Otherwise, when the geometrical filter fails a cross correlation between the stored eigenfunction, related to the previous ω^*, and the N_c eigenfunctions of the current ω^* is performed. To be chosen are those which have a cross correlation coefficient above a threshold value, and then, only the one with the lowest imaginary part of the wave number is selected and stored.

Essentially, the filter always tends to apply the geometric criterion. In cases where this criterion fails, the filter degrades from the geometric criterion to cross-correlation, using the real part of the eigenfunction calculated in the previous step as the base shape. This solution provides the filter with both speed and robustness, inheriting the best from each approach.

4.3.1 Filter Validation

The LST solver and the filter were validated by comparing the results delivered with reference literature solutions.

The LST solver was further assessed by examining Falkner-Skan profiles across varying Hartree parameters, aiming to validate its performance under adverse (Figure 4.8) and favorable

Re_{δ_1}	ω^*	Jordison	Danabasoglu	LST
336	0.1297	0.3084+i0.0079	0.3086+i0.0079	0.3082+i0.0079
598	0.1201	0.3079+i0.0019	0.3080+i0.0018	0.3078-i0.0018
998	0.1122	0.3086-i0.0057	0.3087-i0.0056	0.3085-i0.0056

Table 4.1: Validation of LST+filter. Comparison between the dominant roots for three different combinations of $Re_{\delta_1} - \omega^*$ [9]

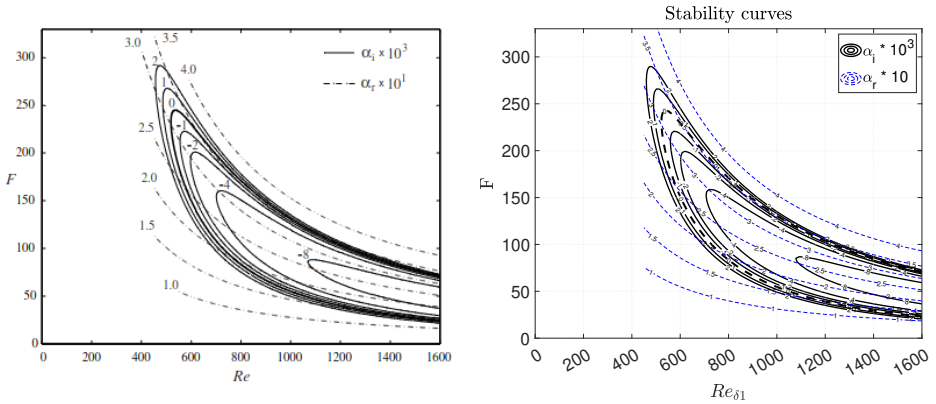

Figure 4.7: Stability curves for Blasius boundary layer. On the left figure provided by Frasson [11] while on the right stability curves calculated with LST + filter. F is the dimensionless angular frequency defined by the equation 2.48

(Figure 4.9) pressure gradient conditions [38]. This rigorous evaluation ensures the reliability and applicability of the solver to evaluate the stability of an airfoil BL .

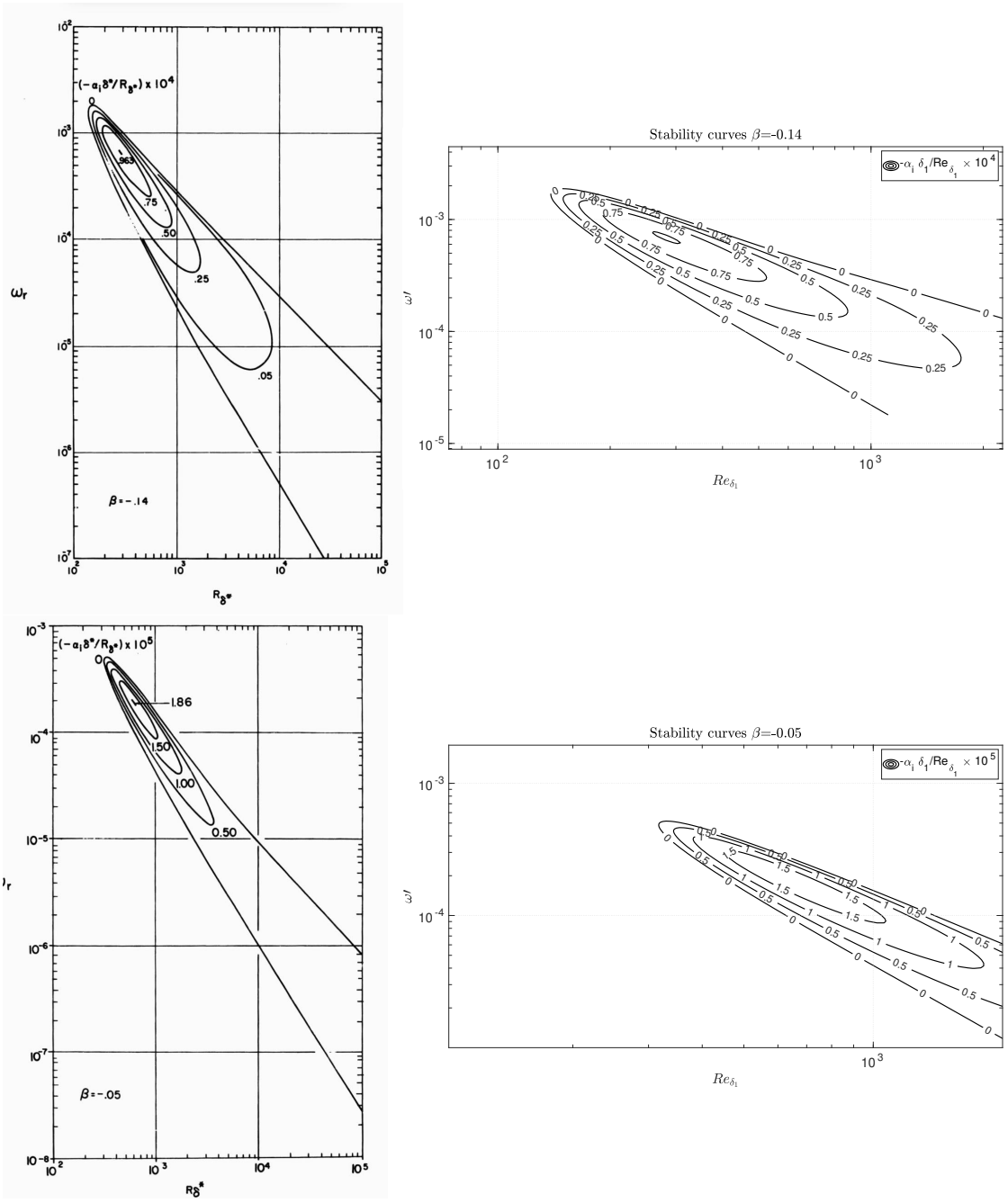

Figure 4.8: Stability curves of constant spatial amplification rate for Falkner-Skann BL and adverse pressure gradient. Left from literature [38], right computed with LST+filter. In the y axis the dimensionless angular frequency $\omega' = \omega\nu/U_e^2$

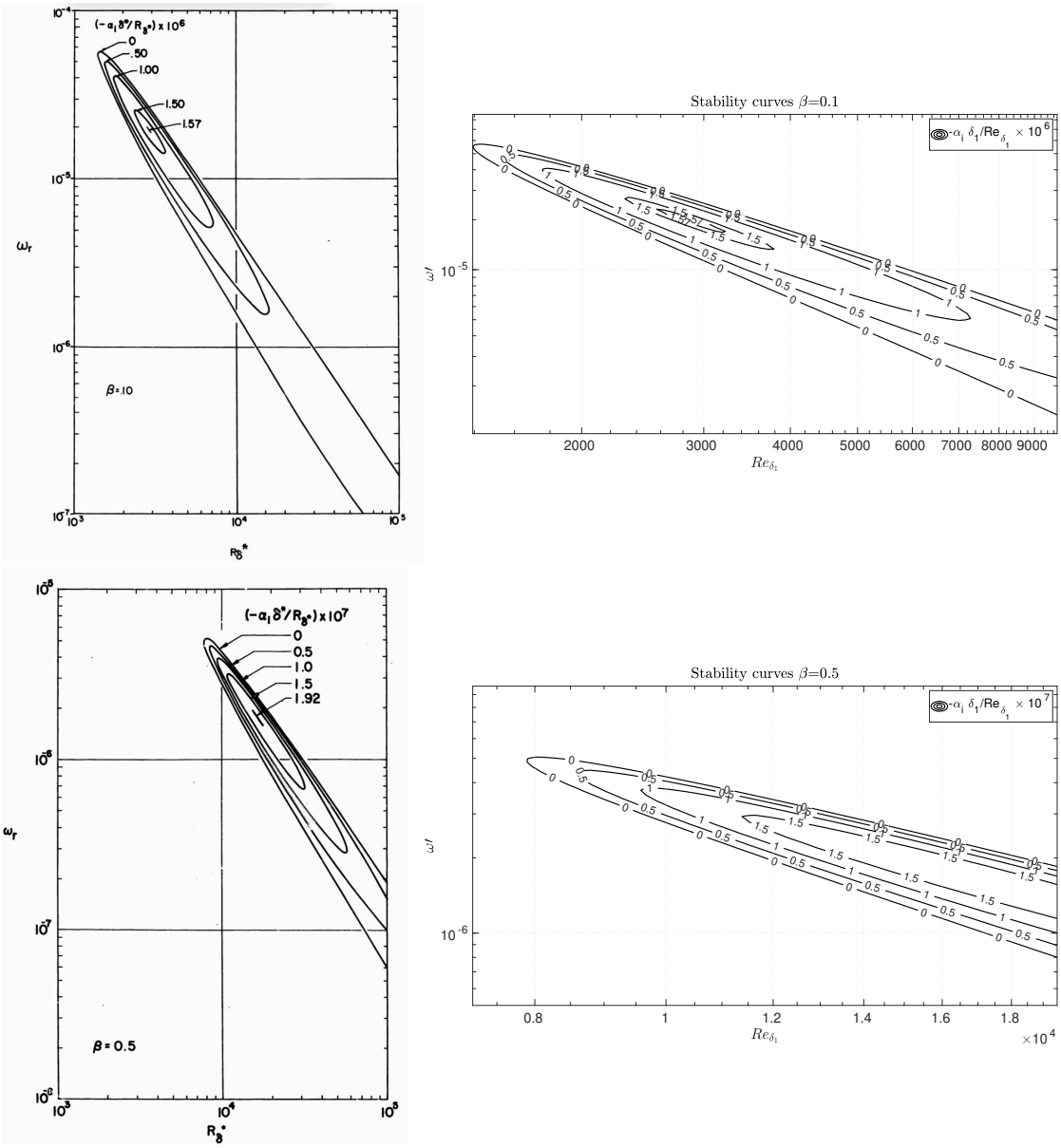

Figure 4.9: Stability curves of constant spatial amplification rate for Falkner-Skann BL and favorable pressure gradient. Left from literature [38], right computed with LST+filter. In the y axis the dimensionless angular frequency $\omega' = \omega\nu/U_e^2$

Chapter 5

Optimal LFC implementation

The initial section of this chapter clarifies the impact of suction on various quantities. The subsequent section is geared towards establishing an efficient numerical framework necessary for proceeding to the optimization phase.

5.0.1 LFC control of suction

Consider a flat plate immersed within a flow with a free stream velocity U_∞. At a distance x_s from the leading edge (LE), a porous panel allows for uniform suction with velocity v_w. The suction region extends over a length d until the solid wall begins again to form x_e (see Figure 5.1).

Suction is characterized by three parameters, $[x_s, x_e, v_w]$, referred to as suction variables henceforth.

From a pragmatic standpoint, removing air near the wall effectively eliminates low-momentum flow, consequently reducing boundary layer thickness. Another perspective on this effect involves examining the trajectory of a fluid particle within the flow. It was previously mentioned that a fluid particle, starting from the leading edge, is advected along the x by the bulk velocity, while a "virtual" friction velocity allows the particle to move also in the wall normal direction y. The displacement of the fluid particle in the y-direction serves as a measure of boundary layer thickness, or at least represents the rate of boundary layer growth.

In steady flows, the trajectory of fluid particles coincides with streamlines, which are depicted in figure 5.2

Figure 5.2 contains a wealth of information regarding both the equation used to model the physics and the physics itself. The gray color represents the natural evolution of the boundary layer (BL), while the blue lines depict the BL with suction control. Initially, before entering the shaded regions, all lines overlap. This holds for most of the region upstream of the slot, although the effects of suction right upstream of the slot are present. Unfortunately, considering BL equations with a parabolic nature do not allow for the inclusion of this effect. Shortly after the suction begins, the streamlines deviate, indicating that particles in the suction region move closer to the wall. It is reasonable to assume, therefore, that the BL thickness will decrease between the starting and ending points of the suction. This reduction is further confirmed by Figure 5.3, which demonstrates an overall reduction in BL thickness. Another significant aspect is how the profiles become fuller and hence more energetic.

The cause of this phenomenon is also evident from Figure 5.2. Fluid particles farther from the wall possess greater velocity. When these particles are drawn towards the wall by the suction,

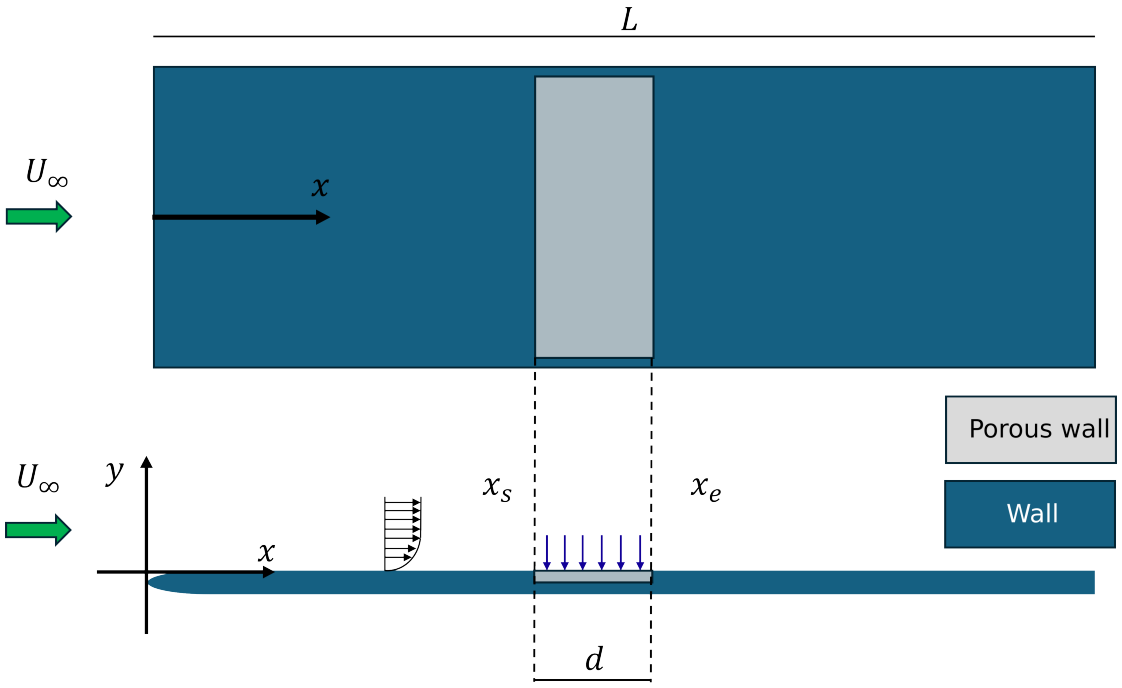

Figure 5.1: Sketch of the geometry and suction configuration. x_s and x_e indicate the boundaries of the porous panel or, alternatively, the location where suction starts and ends. Suction here is represented by vertical arrows above the porous panel as expression of the suction velocity v_w

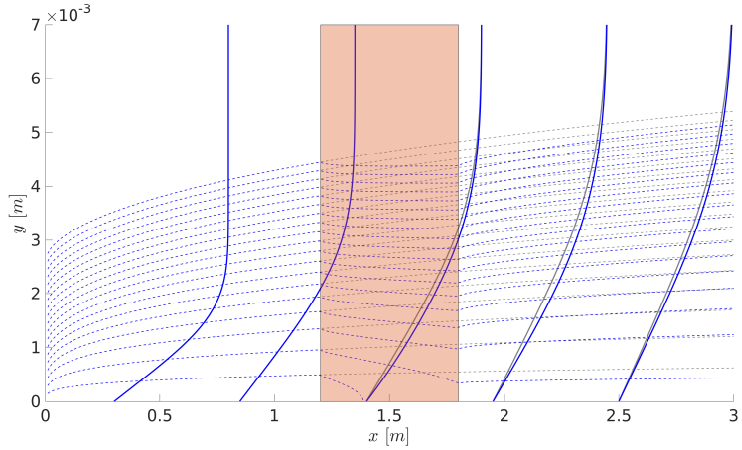

Figure 5.2: Comparison between the enforced laminar flow and LFC with suction($x_s = 1.2$ $[m]$, $x_e = 1.8$ $[m]$ $v_w/U_\infty = -0.02/100$). The gray lines refer to laminar base flow, while the blues to the LFC. Dotted lines represent the stream lines while continuous lines the velocity profiles

they carry their original momentum with them. Consequently, the lower region in the boundary layer (BL) is enriched by the higher momentum originating from the upper region of the BL.

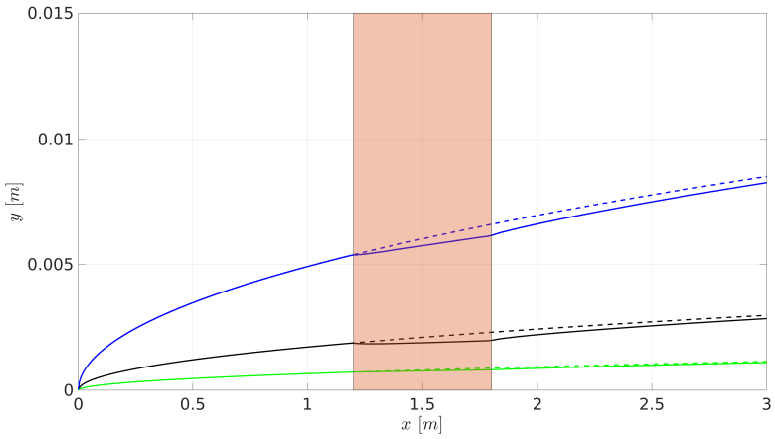

Figure 5.3: Comparison between the enforced laminar flow(dotted lines) and LFC with suction(continuous line).Suction configuration: $x_s = 1.2\ [m]$, $x_e = 1.8\ [m]$ $v_w/U_\infty = -0.02/100$. Black lines represent the displacement thickness δ_1, blue lines the BL thickness δ_{99} and the gray line the momentum thickness θ

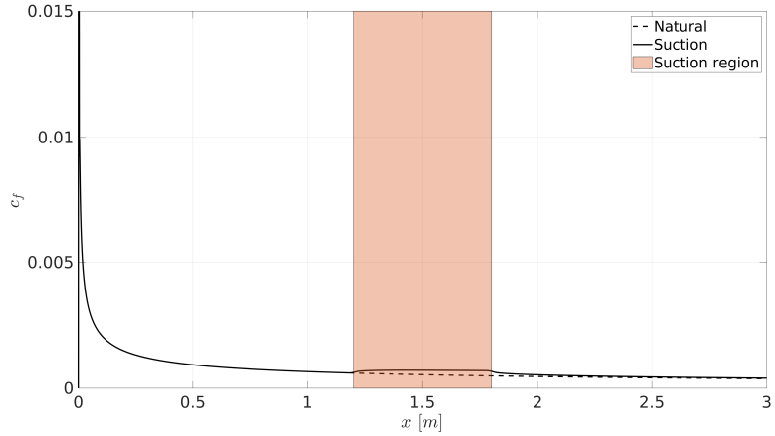

Figure 5.4: Comparison between the friction coefficient of the enforced laminar flow (dotted lines) and LFC with suction (continuous line). Suction configuration: $x_s = 1.2\ [m]$, $x_e = 1.8\ [m]$ $v_w/U_\infty = -0.02/100$.

One consequence of this more energetic boundary layer is the increase in skin friction coefficient or wall shear stresses compared to the case where laminar flow is enforced across the entire flat plate (Figure 5.4).

The effects of suction on stability are widely recognized, as a solution for a boundary layer with uniform and continuous suction was already derived by Prandtl. Suction makes the boundary layer more stable and therefore less susceptible to transition by removing low-energy fluid from it.

Suction enhances the stability of the profile by acting on two fronts: reducing the boundary layer thickness, as previously mentioned. A thinner boundary layer is less prone to transition;

producing a laminar velocity field that has a higher indifference Reynolds number [30].

Figure 5.5 serves as a summary of the preceding discussion and introduces further analysis. The top two figures illustrate the fuller profile previously depicted and explained in Figure 5.2. The two middle figures represent the increase in velocity derivatives $\partial u/\partial y$ at the wall, resulting in higher friction drag. The third row of figures is closely related to stability considerations.

The wall compatibility condition reads:

$$\nu \frac{\partial^2 u}{\partial y^2} = v_w \frac{\partial u}{\partial y} + \frac{1}{\cancel{\rho}} \frac{dP_{e\cancel{(x)}}}{dx} \tag{5.1}$$

Rayleigh's inviscid stability analysis led him to propose the inflection point criterion, which states that the presence of an inflection point in velocity profiles is a necessary condition for the onset of instabilities. However, it's important to note that the Orr-Sommerfeld equation for viscous fluids is more complex than the inviscid equation solved by Rayleigh. Therefore, while Rayleigh's results are not considered definitive, they can still serve as a useful rule of thumb.

Suction/blowing and pressure gradient act on the stability in the same manner.

- **Blowing**. $v_w > 0$ and this leads to a negative curvature at the wall. Somewhere in the upper BL region, the curvature is positive in order to allow the velocity to blend with the external boundary layer velocity. Due to Hilbert's Nullstellensatz the second derivatives must have at least one zero in the middle of the domain allowing the profile to be unstable
- **Solid wall** $v_w = 0$: the inflection point is at the wall.
- **Suction**. $v_w < 0$: the lack of an inflection point is the cause for a more stable profile according to the inflection point criterion.

We can understand why the suction has only a local influence on the stability. As long as suction is applied over some regions, velocity profiles have no inflection points, pushing away the threat of instability. However, soon after, where $v_w = 0$, the inflection point comes back at the wall and with it, the possibility of having instability.

Both Figure 5.6 and 5.7 depict the concept clearly. Upon applying suction, the area of application attains stability, causing the stability map to divide into two parts (as illustrated in Figure 5.7). Consequently, the perturbation amplitude decreases, which is evident from the reduction in the envelope (as shown in Figure 5.6).

5.1 LST automatization

5.1.1 Grid independence study

Before performing any optimization, fine-tuning of the grid parameters is needed in order to achieve both accuracy and speed. The relevance of this operation can be understood by looking at it from an optimization loop perspective, where the same calculations are repeated thousands of times. Saving a small amount of time for each iteration translates into saving hours during the entire optimization process. To provide a perspective, let's assume that, at the end of this tuning process, we manage to reduce the solver computation time by 20 seconds. Considering that the optimization evaluations are in the order of 1000, this translates into saving 20,000 seconds, approximately 5 hours, that would have been otherwise wasted.

MATLAB code is primarily divided into two solvers: BLES and LST. BLES generates velocity profiles that serve as the initial inputs for the LST solver, which performs stability calculations. As a result, the following analysis will also be split into two parts, corresponding to the functionality

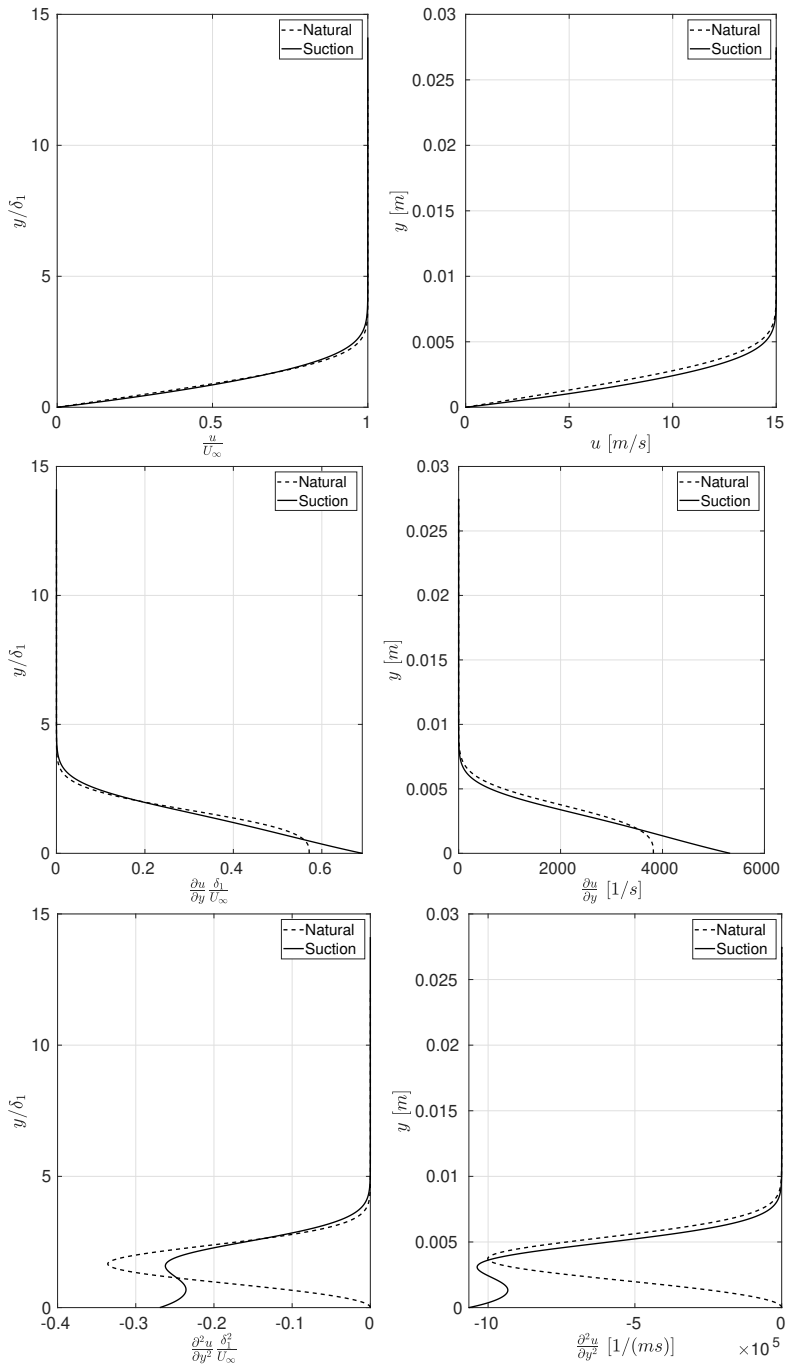

Figure 5.5: Comparison between the enforced laminar flow (dotted lines) and LFC with suction(continuous line) at $x = 1.7\ [m]$.Suction configuration: $x_s = 1.2\ [m]$, $x_e = 1.8\ [m]$ $v_w/U_\infty = -0.02/100$. In the left columns dimensionless quantities are shown while in the right there are the corresponding dimensional variables.

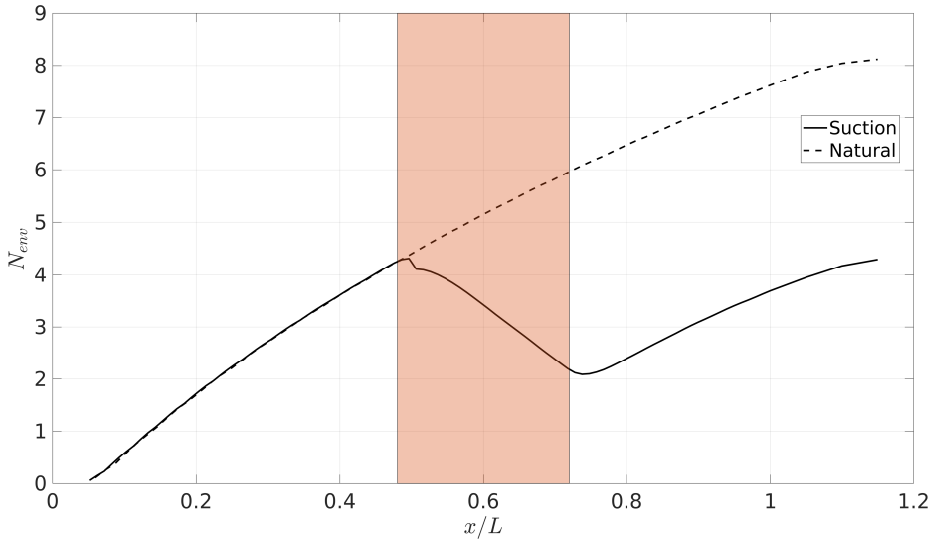

Figure 5.6: Comparison between the envelope of the enforced laminar flow (dotted lines) and LFC with suction(continuous line).Suction configuration: $x_s = 1.2$ $[m]$, $x_e = 1.8$ $[m]$ $v_w/U_\infty = -0.02/100$.

of these solvers.
To assess the independence of BLES from the grid, we start defining two different grids which will be involved in the next paragraphs, referred to as computational and sampling grid. The former pertains to the grid employed for solving the BL equation, whereas the latter pertains to its utilization in the assessment of convergence rate. The reason for their introduction will be clarified later.
The BLES requires some kind of discretization of the continuum physical domain to solve the boundary layer equation. As was already mentioned in the designated section, the plate length L is divided into N_x equally spaced points, while, along the y coordinate, the total number of points N_y that discretize the height H, obey a Chebyshev distribution. The reason for the name "computational grid" now becomes clear since it is the grid used in the first place to compute the velocity profiles.
Changing the number of discretization points has different effects in terms of cost and accuracy that we wish to obtain. The cost to run a simulation is easily measured in terms of the time required by the solver to complete the calculation, therefore it is easy to get an estimation. On the other hand, measuring the accuracy, under the involved circumstances, is not trivial. Usually, the convergence study is performed on some target integral quantity we are most of the time interested in. Changing of the target quantities with the grid are tracked and when no substantial changes are spotted, the numerical solution can be regarded as independent from the discretization.

When BLES is involved, our interest lies in the velocity profiles and their curvature since these two are the main inputs for the following solver that deals with the OS equation, therefore they are selected as target quantities. Opting for this particular choice gives rise to numerous challenges. For start, the points in space where the solution is computed change as the computational grid

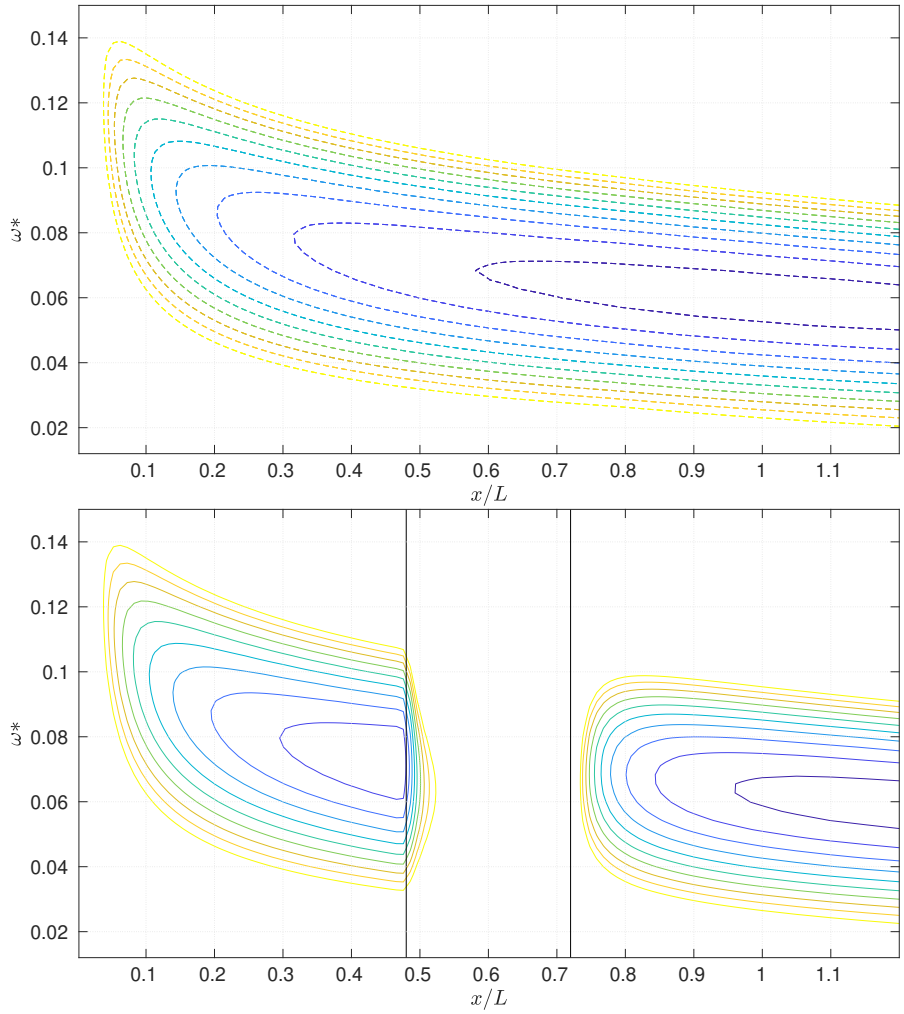

Figure 5.7: Iso-curves of constant amplification factor $\alpha_i \leq 0$. The above figure refers to the natural case, while the bottom figure represents the stability diagram in the case of LFC with suction. The suction region here is bounded by the two black vertical lines

changes, therefore it is impossible to directly compare the solution coming from BLES without doing some operation first. A workaround is to map the velocity field from the computational grid to another grid, fixed in the physical space and therefore independent from the discretization grid. At this juncture, a second grid comes in handy. This grid is introduced to collect information on the velocity field consistently at the same position, an operation commonly referred to as sampling. Given that the primary objective of this grid is to sample the velocity field, it is appropriately named the *sampling grid*.

Several simulations were conducted by progressively increasing the number of discretization points in the x and y directions of the computational grid. We refer with n_x and n_y as the total number of sets of N_x and N_y under investigation.

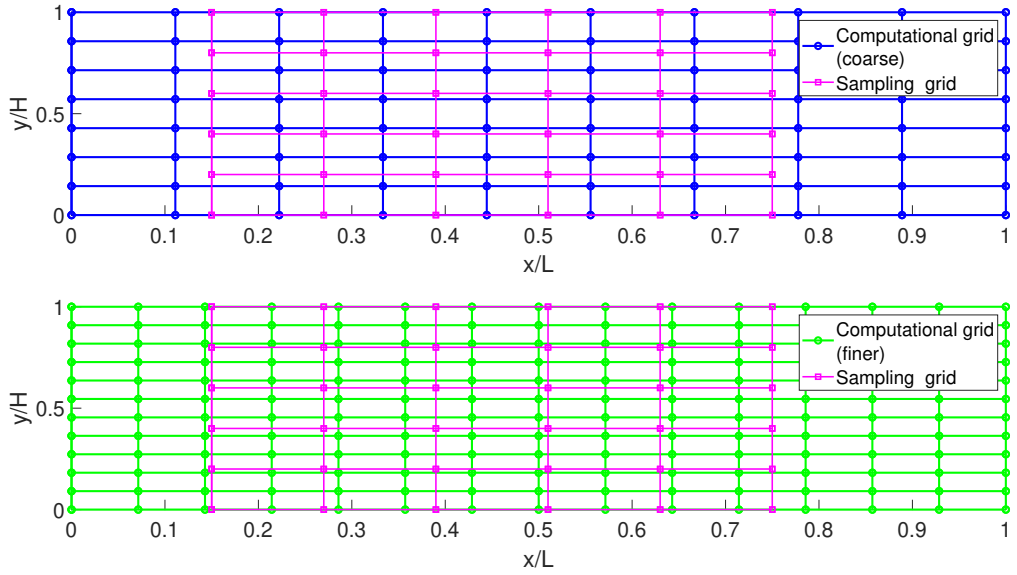

Figure 5.8: Schematic representation, not to scale, of computational and sampling grid

$$k = 1, 2, ..., n_x - 1, n_x$$
$$h = 1, 2, ..., n_y - 1, n_y$$
$$N_x^{k+1} > N_x^k$$
$$N_y^{h+1} > N_y^h$$

The time required to solve the boundary layer equations is computed by using the combination of the MATLAB commands tic and toc, giving the information on the computational cost in terms of seconds. From figure 5.10 we can infer that the dependency of the time respect N_x and N_y is completely different. A small change in the number of N_y nodes is responsible for a significant increase in the computational time while the dependence on N_x is far milder.

Unfortunately, the available data are insufficient to draw any conclusions regarding the computational grid, as the determination of the number of nodes required for convergence is still pending. To address the question, an operator referred to as 'δ' needs to be introduced. For a given computational grid defined by the parameters (k, h), a matrix is constructed containing the x component of the velocity vector evaluated at the sampled grid points. This matrix is a 4th-order tensor denoted by four indices $U_{i,j,k,h}$.

$$U_{i,j,k,h}$$

- i: x sampling grid point
- j: y sampling grid point
- k: x-computational grid index (N_x^k nodes along x)
- h: y-computational grid index (N_y^h nodes along y)

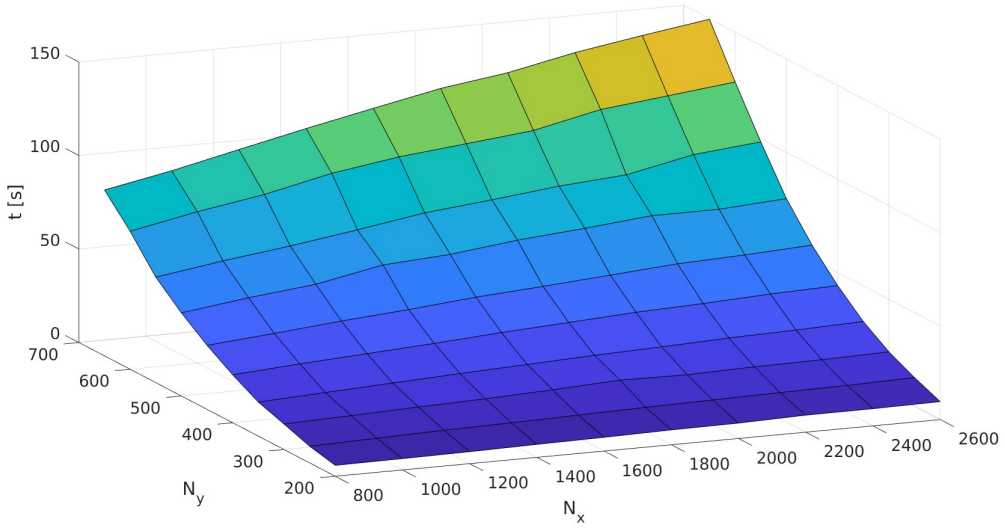

Figure 5.9: BLES solution time as a function of the nodes along x and y.

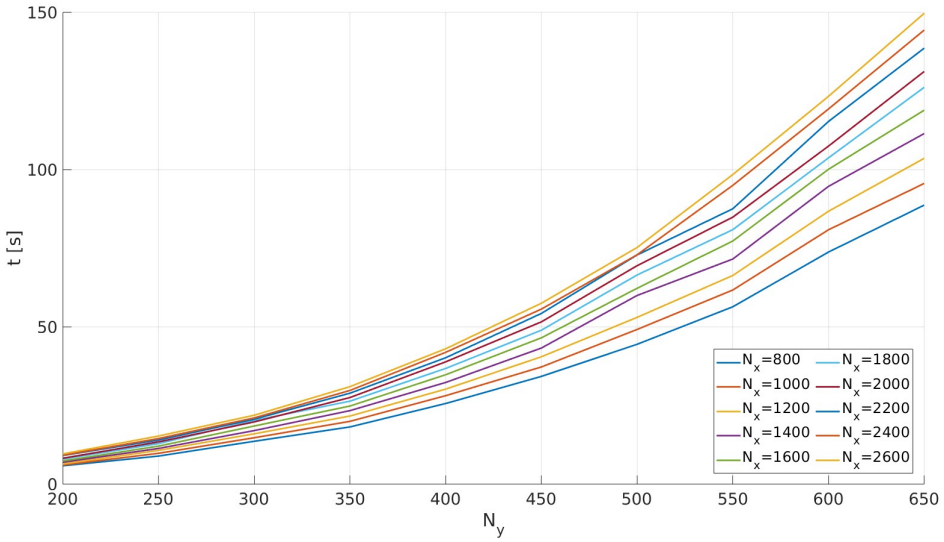

Figure 5.10: BLES solution time as function N_y and N_x, here introduced as curves parameter.

Using this matrix, we can assess the rate of variation of $U_{i,j,k,h}$ respect to h and k, which indicates how the field at the sampled grid points is influenced by the computational grid.

$$(\delta_y U)_{h,k} = \frac{\mid U_{:,:,k,h+1} - U_{:,:,k,h} \mid_2}{\mid U_{:,:,k,h+1} \mid_2} \tag{5.2}$$

$$(\delta_x U)_{h,k} = \frac{\mid U_{:,:,k+1,h} - U_{:,:,k,h} \mid_2}{\mid U_{:,:,k+1,h} \mid_2} \tag{5.3}$$

The same operator δ is also applied to the curvature of the velocity profile, represented by the matrix $\left(\frac{\partial^2 U}{\partial y^2}\right)_{i,j,k,h}$. To simplify the notation, we refer to $\left(\frac{\partial^2 U}{\partial y^2}\right)_{i,j,k,h}$ as $\left(\partial_y^2 U\right)_{i,j,k,h}$.
The near-perfect overlap of curves across all four graphs suggests that studying the convergence of the grid along the x and y directions can be done independently, given their lack of correlation.

Beginning with the nodes N_x, it is noticeable that the change in the U solution remains quite small, around the order of 1e-4, as shown in figure 5.11. However, the curvature $\partial_y^2 U$ exhibits a larger error, nearly plateauing for N_x values exceeding 1600. Given the relatively mild impact of simulation time concerning x discretization, the choice of N_x is guided by considerations regarding the smallest element utilized in the optimization loop. As elucidated in the subsequent paragraph, defining the optimization environment, the minimum slot length permissible within the optimization loop is 1 cm. Thus, the intention to allocate at least 10 nodes along the slot dictates a spacing of 1mm between consecutive nodes, resulting in 2500 discretization nodes, as further detailed.

Ny was chosen to be 350 because it is the minimum value, for which $\partial_y^2 U$ reaches the lowest value without requiring long computational time. In conclusion, the average amount of time required for IBL to run, with $N_x = 2500$ and $N_y = 350$ is about 30s.

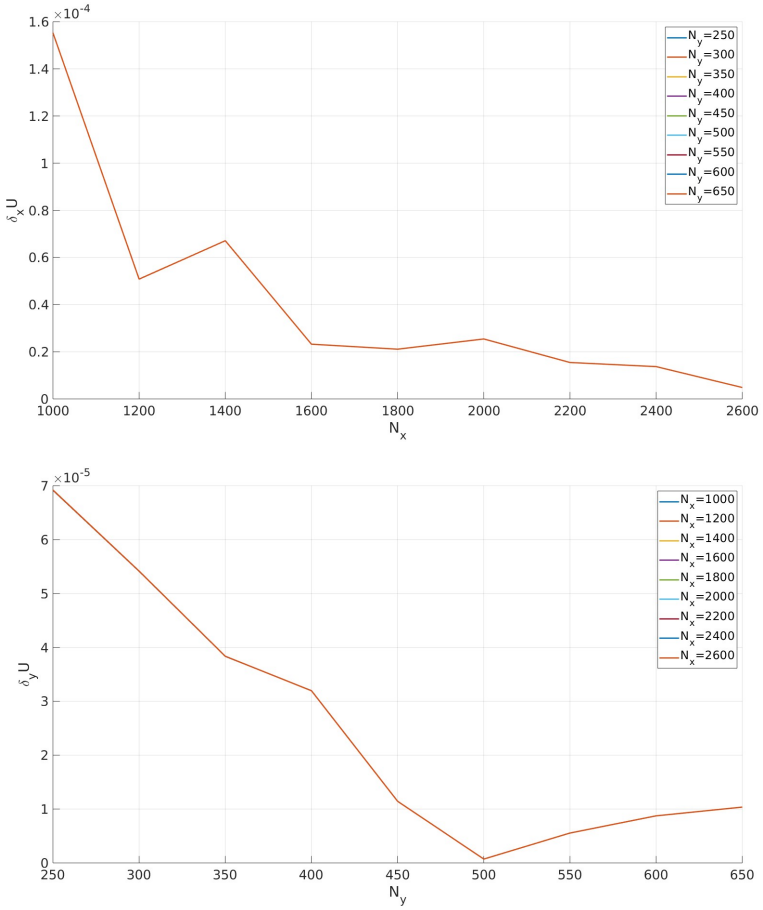

Figure 5.11: Relative rate of variation of U with respect N_x and N_y

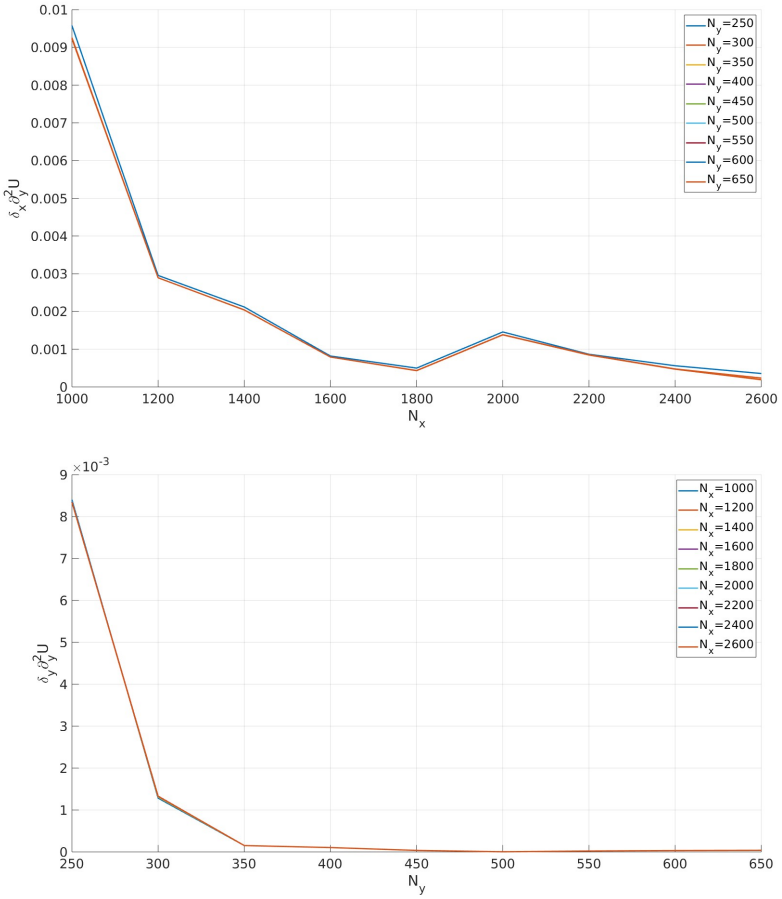

Figure 5.12: Relative rate of variation of $\partial_y^2 U$ with respect N_x and N_y

However, the entire process is mostly dominated by the LST computational time. Given the velocity profiles and their curvature, the LST takes in the order of many minutes to perform a simulation. This elapsed time is given by the product between two elements:

$$\Delta t_{elapsed} = \Delta t_{OS}\, N_{pairs} \tag{5.4}$$

- The time required to obtain one LST solution (composed by N_c pairs of eigenvalues and eigenfunctions) by solving the Orr-Sommerfeld equation, denoted as Δt_{OS}, involves solving a linear system using the MATLAB backslash command (mldivide), which has a time complexity of $\mathrm{O}(N_c^3)$.

  Within the LST solver, both the velocity and its second derivative are interpolated on a Chebyshev grid consisting of N_c nodes. This operation offers several advantages. Firstly, it is possible to disengage the number of nodes through which the profiles are provided from the nodes used to perform the OS calculation. For instance, while the BLES outputs U and $\partial^2 U/\partial y^2$ represented across 350 nodes, performing LST calculations with such a large quantity of nodes would be impractical.

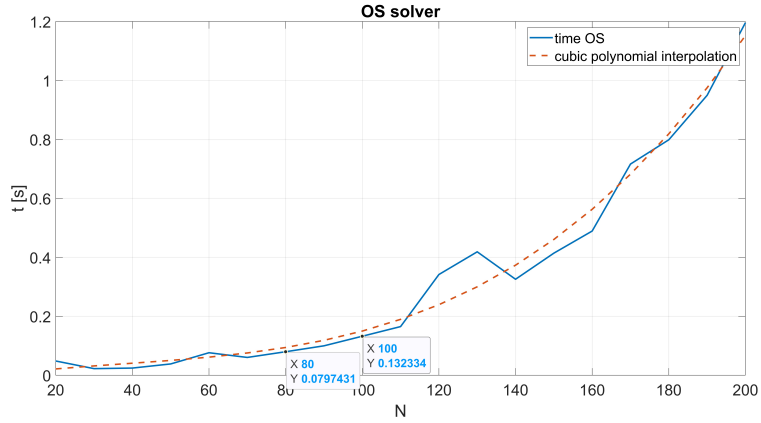

(a) LST solution time versus N_c

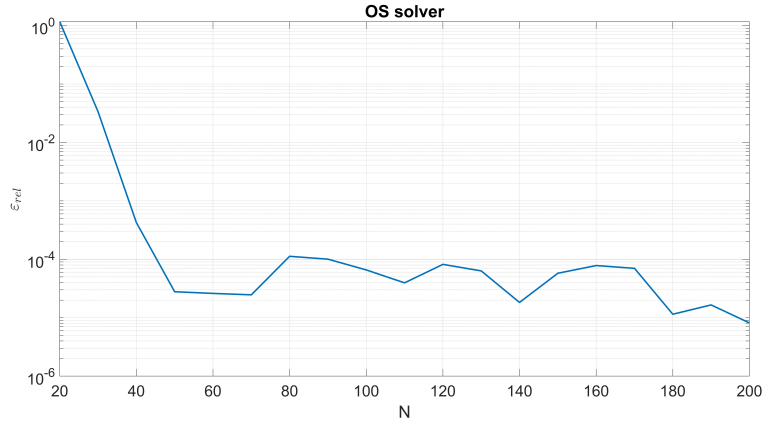

(b) Relative error related to the imaginary part of the dominant root versus N_c

Figure 5.13

The second, and perhaps more critical, reason is that the algorithm involved in the LST solution requires a Chebyshev distribution to perform the calculation. Therefore, even in scenarios where the velocity is computed on a uniform or any other grid, a remapping is necessary for the solver to work.

In the wake of what we have done above, the purpose of this paragraph will be to choose the appropriate value of N_c such that the desired compromise between velocity and accuracy is achieved. $N_c = 80$ was the ultimate choice.

- The final check left concerns what is called N_{pairs}, given by the product of the number of x-stations where the stability is calculated and the number of points that discretize the frequency range.
  As evident from the figures 6.12, the differences in N_{env} are not substantial. Therefore, in this final case, an attempt was made to expedite the computation time by choosing $N_x = 60$ and $N_y = 40$.

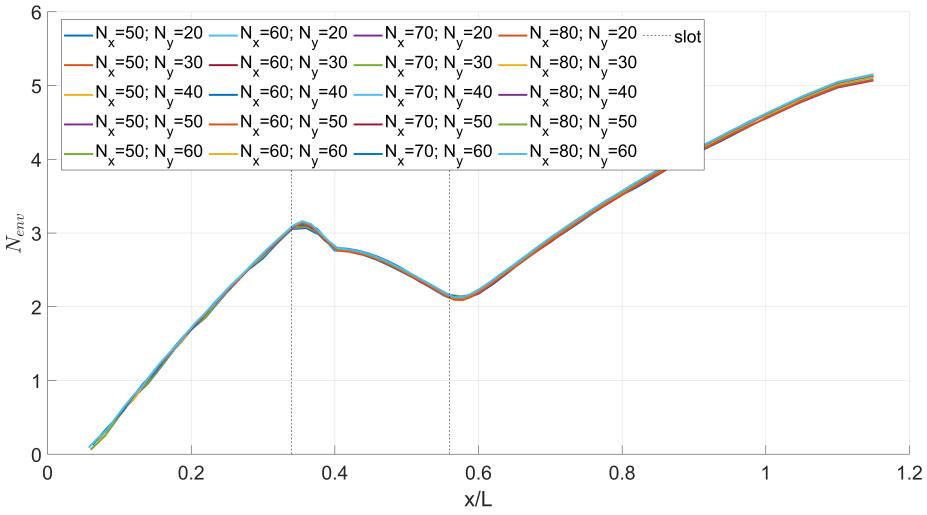

Figure 5.14: N_x number of profiles evaluated N_y total number of frequency ω^* tested

Based on what has been discussed, it is now possible to estimate the time required to carry out a single simulation.

$$\Delta t_{tot} = \Delta t_{IBL} + \Delta t_{OS}\, N_{pairs} \sim 30 + 2400 * 0.08 = 222s$$

5.2 Optimization environment

All the instruments presented so far have been designed to be incorporated into an optimization algorithm; the aim of which is to identify the optimal suction variables, i.e. the best position and flow rate to delay the transition of the flow into a turbulent and hence maximize the extension of the laminar region as efficiently as possible. While the general definition of an optimality problem has a standard form, it is important to state the conventions adopted in this study, as they can vary depending on the author or the literature. It is worth noting that some algorithms require the optimal configuration to be the one that maximizes an objective function f(x), while others prefer to formulate the optimization in terms of finding a minimum assumed by the function q(x). It is possible to switch between the two forms by declaring q(x)=-f(x) or q(x)=1/f(x). Another integral part of the optimization problem definition relates to the sign assumed by the inequality constraints for the definition of the feasible regions.

It is crucial, therefore, to explicitly declare the conventions about the standard form for a continuous optimization problem:

$$\begin{cases} \min_x f(\boldsymbol{x}) & s.t. \\ g_i(\boldsymbol{x}) \leq 0 & i = 1, 2, \ldots m \\ h_i(\boldsymbol{x}) = 0 & i = 1, 2, \ldots p \end{cases}$$

f(x) represents the function subject to the optimization process, while g(x) and h(x) denote the inequality and equality constraints that have to be fulfilled by the design variables x. To

enable the effective application of any readily available optimization algorithm, it is imperative to transform any problem into this standard formulation. This section will address the objective function definition, according to our goals, as well as the constraints, providing reasoning for their selection.

Delaying transition essentially involves shifting the location where the transition occurs x_t as close as possible to the trailing edge of the flat plate, which in mathematical terms literally traduces into minimizing the quantity $(L - x_t)/L$, where the physical distance is rescaled with the plate length L to have a non-dimensional quantity. This non-dimensionalization helps mitigate the influence of experiment-dependent parameters, such as the length of the simulated plate aiming for results that are more universal and independent from the specific experimental conditions.

Given that, the function to optimize is defined by:

$$f(\boldsymbol{x}) : \Omega \subseteq \mathbb{R}^3 \to \mathbb{R} \tag{5.5}$$

$$f(\boldsymbol{x}) = \frac{L - x_t(\boldsymbol{x})}{L} \tag{5.6}$$

The $\boldsymbol{x}$ vector has, as components, the optimization variables.

$$\boldsymbol{x} = (x_1, x_2, x_3) = (x_s, x_e, v_w) \in \Omega \subseteq \mathbb{R}^3 \tag{5.7}$$

$$x_i^{lb} < x_i < x_i^{ib}$$

Or in a vectorial formulation

$$\boldsymbol{x}^{lb} < \boldsymbol{x} < \boldsymbol{x}^{ib}$$

As the suction configuration becomes more favorable, the objective function progressively decreases.

$$x_t(\boldsymbol{x}) \to L, \quad f(\boldsymbol{x}) \to 0^+ \tag{5.8}$$

In turn, x_t can be seen as a function:

$$x_t(\boldsymbol{x}) : \Omega \subseteq \mathbb{R}^3 \to \mathbb{R} \tag{5.9}$$

Basically, for every configuration in terms of slot position, width, and suction velocity, there will be a corresponding shift in the transition position along the x-axis, as depicted in figure 5.15. Finally, the objective is a composite function of

$$f(x_t(\boldsymbol{x})) = f(\boldsymbol{x}) \tag{5.10}$$

Breaking down the components of the $\boldsymbol{x}$ vector to define the variable bounds:

- x_1 denotes the point where suction starts x_s. The lower boundary x_s^{lb} is determined by the location of the indifference Reynolds number. In the realm of the LST approach, applying suction before this point is meaningless since the profile is already stable. The upper boundary of the suction starting location is influenced by the mathematical nature of the boundary layer equations. It is commonly known that the BL equations exhibit a parabolic nature, indicating that events at position x^* only affect downstream ($x > x^*$) evolution and have no impact on upstream development. Our thorough theoretical and numerical analysis indicates that applying suction beyond the natural transition point has little to no effect on boundary layer transition. This means that utilizing suction control on a flow that

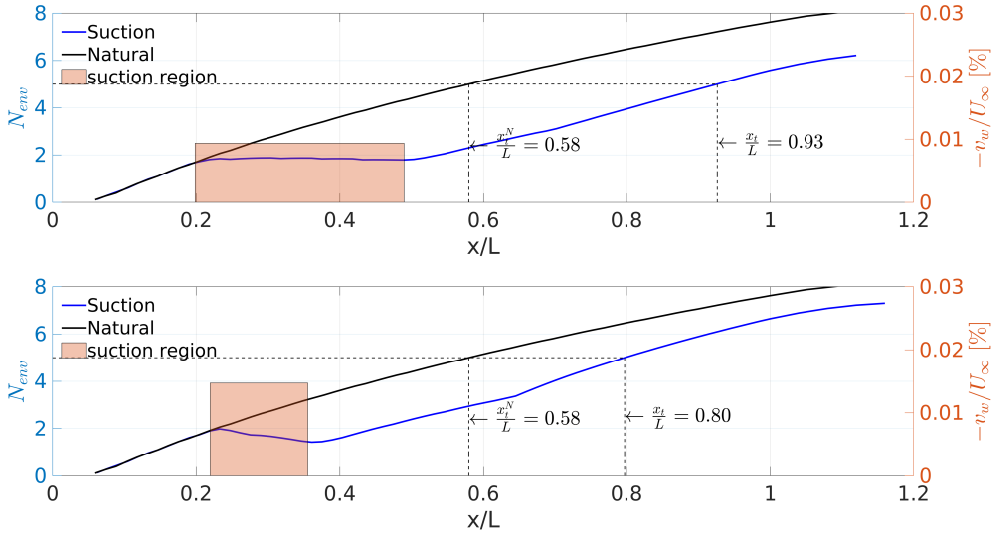

Figure 5.15: The two figures illustrate the evolution of the maximum amplification factor as a function of the normalized streamwise coordinate x/L. The suction region's position is delineated by the orange rectangle, wherein its height states the suction velocity v_w. Notably, alterations in the suction variables, manifested through shifting or stretching of the rectangle, induce corresponding changes in the transition position x_t. To demonstrate the benefits induced by suction, the evolution of N_{env} without suction control, alongside the abscissa of natural transition x_t^N/L, is also illustrated.

has already transitioned will not change the transition position in comparison to a natural transition scenario. Delaying transition can only occur by operating the control on laminar flow. It is important to note that this assertion holds true employing BLES to compute the velocity field, LST for stability computations and the e^N method for transition prediction. x_s is upper and lower bounded by:

$$0.037 < \frac{x_s}{L} < 0.58 \tag{5.11}$$

Where $x_s^{ub} = x_t^N/L = 0.58$ is the point of natural transition while

$$x_s^{lb} = x_{ind} = \left(\frac{(Re_{\delta_1})_{ind}}{1.72}\right)^2 \frac{\nu}{U_\infty} = 0.037$$

$U_\infty = 15\ [m/s]$, $(Re_{\delta_1})_{ind} = 520$

- $x_2 = x_e$ is the last point where suction is implemented. The reasons leading to its boundaries are moved by easy motivations.

$$0.041 < \frac{x_e}{L} < 0.92 \tag{5.12}$$

Since $x_e = x_s + d$, chosen the minimum slot width to be $d/L = 0.004$ follows $x_e/L = 0.041$. The upper boundary is moved by the necessity of ending the suction before reaching the trailing edge for obvious reasons.

- x_3 is the wall suction velocity, defined with the symbol v_w.

$$-0.0267 < \frac{v_w}{U_\infty} < 0 \tag{5.13}$$

The reason for this value will be made clearer when the constraints about the mass flow rate will be introduced.

Ω is therefore a cube, setting the range through which each design variable will span.

$$\Omega = [0.037,\ 0.5800] \times [0.041,\ 0.9200] \times [-0.0267,\ 0] \tag{5.14}$$

Besides these elementary boundaries, one can set other relations among the variables, representing the real problem constraints.

$$g_1(\boldsymbol{x}) = \frac{x_e - x_s}{L} - 0.4 \tag{5.15}$$

$$g_2(\boldsymbol{x}) = \frac{x_e - x_s}{L} - 0.004 \tag{5.16}$$

$$g_3(\boldsymbol{x}) = \frac{x_e - x_s}{L}\frac{v_w}{U_\infty} - 1.06 \times 10^{-4} \tag{5.17}$$

$$\boldsymbol{g(x)} \leq 0 \tag{5.18}$$

- $g_1(\boldsymbol{x})$ prescribes the maximum porous panel width;
- $g_2(\boldsymbol{x})$ prescribes the minimum porous panel width;
- $g_3(\boldsymbol{x})$ prescribes the maximum volume mass flow allowed.

  The selected value 1.06×10^{-4} was chosen as a reference based on existing literature. Corelli et al. [7] employed a volume flow rate on the order of 10^{-2} $[m^3/s]$, while Reynolds & Saric [28] and Meter et al. [25] utilized a mass volume flow rate of 10^{-3} $[m^3/s]$. To strike a balance between these disparate values, an intermediate value of 4×10^{-3} $[m^3/s]$ was selected. Consequently, scaling this value with the plate length $L = 2.5$ $[m]$ and the free stream velocity $U_\infty = 15$ $[m/s]$ yields:

$$\frac{4 \times 10^{-3}}{15 \cdot 2.5} = 1.06 \times 10^{-4} \tag{5.19}$$

  From this constraint follows the lower boundary on the velocity v_w

$$v_w^{lb} = \frac{1.06 \times 10^{-4}}{\left(\frac{x_s - x_e}{L}\right)_{min}} = \frac{1.06 \times 10^{-4}}{0.004} = 0.0267 \tag{5.20}$$

To help the optimization algorithm find the optimal combination of suction variables, an extended plate $L + \Delta L$ was simulated.

It is easier to explain the motivation that led to this choice starting with an example: consider a configuration, $\boldsymbol{x'}$, where the critical N_{env} value is attained at $x/L = 1$, implying that the numerical framework predicts transition at the trailing edge (TE) for the suction variable $\boldsymbol{x'}$.

The algorithm is looking for the optimum, yet it operates without prior knowledge of the optimal configuration $\boldsymbol{x'}$. During its exploration, the algorithm may venture close to $\boldsymbol{x'}$, represented as $\boldsymbol{x} = \boldsymbol{x'} + \boldsymbol{\delta x}$, where $||\boldsymbol{\delta x}||/||\boldsymbol{x'}|| \ll 1$. Two cases now unfold: $x_t(\boldsymbol{x}) > L$ or $x_t(\boldsymbol{x}) < L$. Suppose

a plate of length L is simulated; the corresponding objective function is illustrated on the right of Figure 5.16. When $x_t(\boldsymbol{x}) < L$, the actual objective function value can be determined by computing the abscissa x_t at which $N_{\text{env}}(x_t(\boldsymbol{x})) = N_{\text{env}}^{\text{crit}}$. Conversely, if $x_t(\boldsymbol{x}) > L$ with the plate length L, the envelope curve ceases at $x = L$. At this juncture, $N_{\text{env}}(L) < N_{\text{env}}^{\text{crit}}$, signifying that the envelope never attains the critical value, thereby precluding the estimation of the transition point. Consequently, no useful transition prediction can be made. Meanwhile, the Bayesian Optimization (BO) algorithm requires a value of $f(\boldsymbol{x})$ to associate with $\boldsymbol{x}$.

Based on our analysis, it appears that the level of suction in the current configuration is excessive, as evidenced by the transition point extending beyond the plate. Although the precise value of the objective function for this suboptimal scenario cannot be determined, we have assigned a discouragingly high value to prevent future attempts. However, this approach poses a challenge as the objective function experiences a discontinuity at the optimal configuration $x_t = L$, which is not conducive to BO's ability to work well with continuous functions. Additionally, the algorithm loses its sensitivity about the distance between the configuration tested $\boldsymbol{x}$ and the optimum $\boldsymbol{x}'$.

A solution to restore continuity and sensitivity consists of simulating a plate with length $L + \Delta L$. The new objective function is shown in figure 5.16 on the left. For $x_t(\boldsymbol{x}) < L$ the same considerations did before apply. Now, if $x_t(\boldsymbol{x}) > L$, the envelope extends ΔL after plate TE. This allows us to compute the actual $x_t(\boldsymbol{x}) > L$.

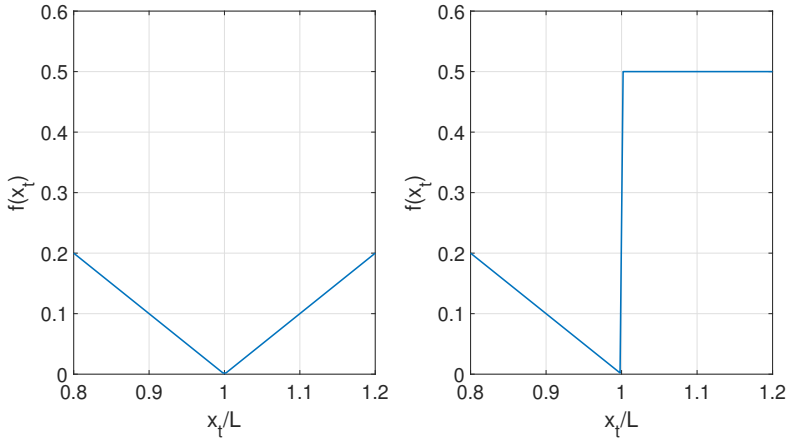

Figure 5.16: Objective function representation. On the left is the case where a plate of length $L+\Delta L$, whereas on the right, for a plate of length L, the objective function shows a discontinuity at $x_t/L = 1$.

Choosing $\Delta L/L = 0.2$ allows us to collect information on the transition position beyond the trailing edge, thereby introducing small increments in the objective function for slight departures from the optimal configuration. The new definition of the objective function is as follows.

$$f(\boldsymbol{x}) = \begin{cases} \frac{L-x_t}{L}, & x_t \leq L \\ -\frac{L-x_t}{L}, & L < x_t \leq L + \Delta L \\ 0.5 & \textit{Non valid case} \end{cases}$$

$f(\boldsymbol{x}) = 0.5$ pertains to the sub-optimal scenarios characterized by excessive mass flow, leading to negative maximum amplification factors (Figure 5.17) or transition occurring beyond the TE of the extended plate $x_t(\boldsymbol{x}) > L + \Delta L$, as depicted in Figure 5.18.

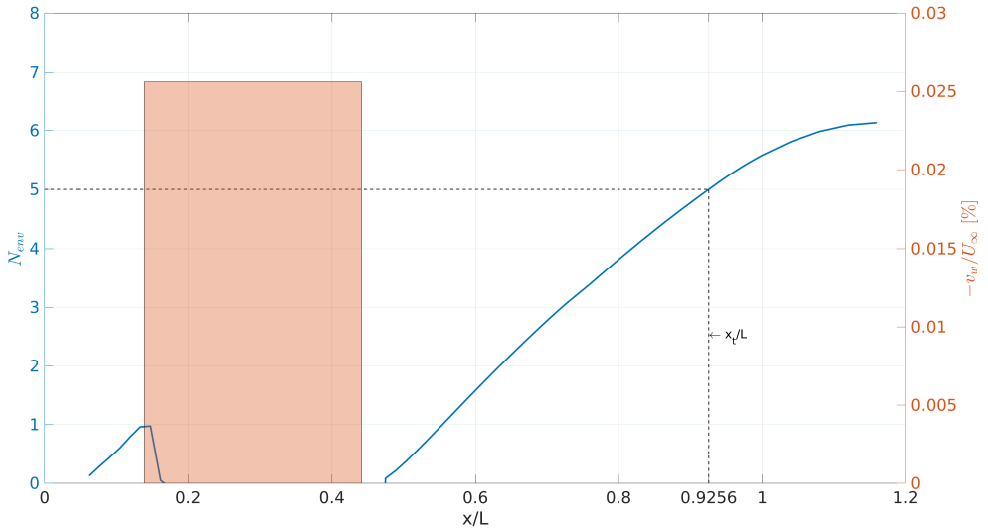

Figure 5.17: N_{env} as function of x/L for a sub-optimal case: the envelope goes below zero; no-physical meaning.

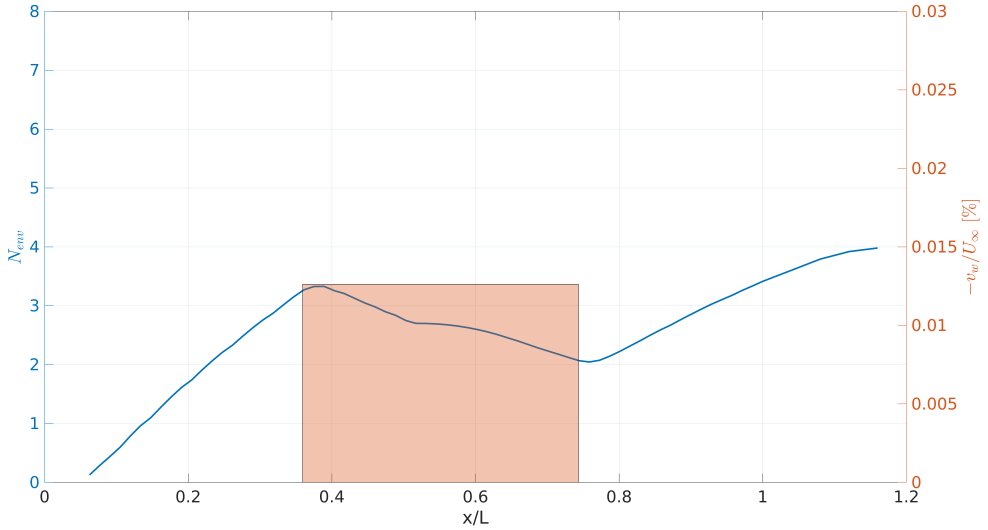

Figure 5.18: N_{env} as function of x/L for a sub-optimal case: transition doesn't happen at all within $L + \Delta L$; some energy employed to do suction is wasted.

Chapter 6

Results

6.1 Bayesian optimization: results and comments

The optimization was conducted in MATLAB® utilizing the bayesopt MATLAB® routine, which is part of the Statistics and Machine Learning Toolbox™. The simulation was initiated with 170 valid values selected from the initially generated set of 400 random configurations created to cover the design space comprehensively, taking care that this set of initial solutions, as neutral as possible, wouldn't introduce any bias. The initial configurations were externally solved to filter out non-valid configurations before providing the whole pool of initial solutions to the Bayesian algorithm.
Expected-improvement-plus was chosen as acquisition function, coupled with an exploration ratio of 0.8 to guarantee the appropriate balance between exploration and exploitation.

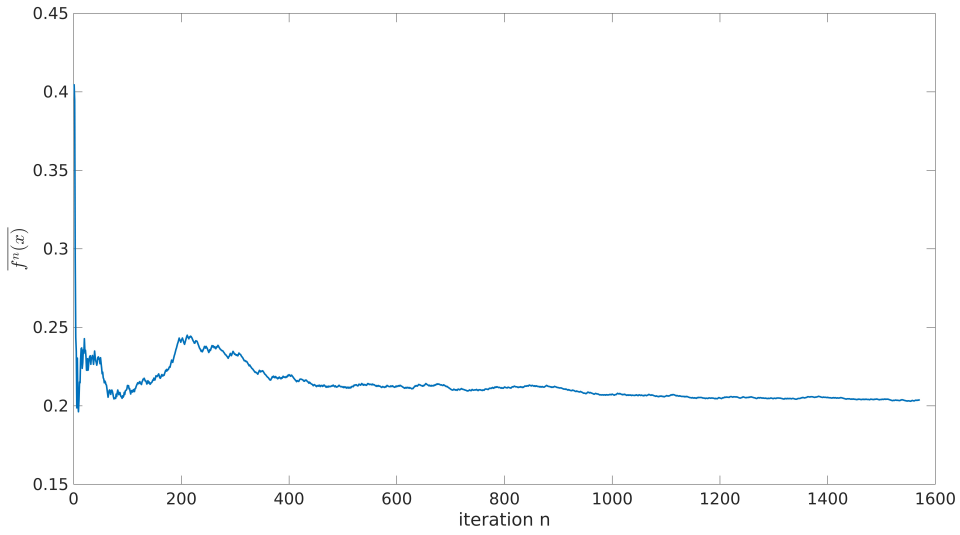

Figure 6.1: Cumulative average of the fitness values throughout the optimization process

After nearly 600 iterations without any improvement (no better global solution is found since

1000^{th} iteration), the decision was made to conclude the optimization, having explored about 1600 configurations. The fitness value cumulative average, defined in Eq. 6.1, is shown in Figure 6.1.

$$\overline{f^n(\boldsymbol{x})} = \frac{1}{n}\sum_{i=1}^{n} f(\boldsymbol{x}_i) \tag{6.1}$$

An attempt to summarize the exploration history is presented in figure 6.2, featuring the suction length (d), the slot center position (x_m), and the volume flow rate (q). It is important to note that these three variables differ from those used within the optimization, and the reason behind this replacement will soon become clear.

The inspection capabilities of the BO algorithm are visible from Figure 6.2, where each optimization variable spans the entire available range. The amount of data produced out of the optimization process is overwhelming and what is left to us is to interpret, verify the correctness and in the end, explain them.

In figure 6.3a, the cloud of points are color-coded based on their associated fitness value,

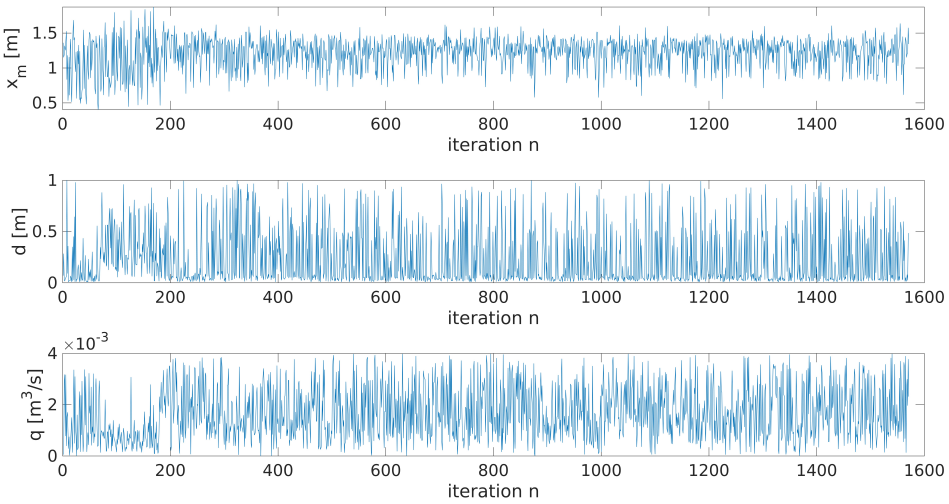

Figure 6.2: Explored design points during the optimization process expressed as slot center location (top figure), slot width (at the center) and volumetric flow rate (bottom figure)

with the color spectrum ranging from red (indicating poor performance configurations, with values near 0.5) to blue (representing optimal solutions with values near 0). The blue points are uniformly spread throughout the feasible domain, suggesting the presence of multiple optimal configurations. While it's difficult to determine what these optimal solutions have in common, considering variables such as slot width and volume flow rate may offer a new perspective.

$$d = x_e - x_s \tag{6.2}$$

$$q = -v(x_s - x_e) \tag{6.3}$$

$$x_m = \frac{x_e + x_s}{2} \tag{6.4}$$

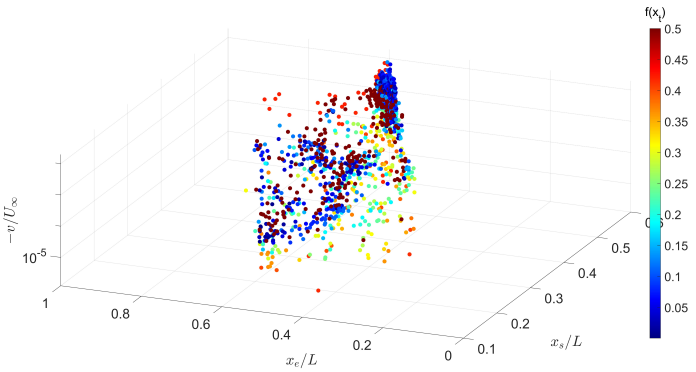

(a) 3D view of the design space

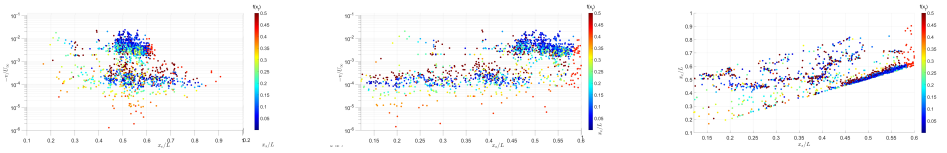

(b) Projection on v-x_e plane (c) Projection on v-x_s plane (d) Projection on $x_s - x_e$ plane

Figure 6.3: The design space is represented by a scatter plot, with each point color-coded according to its fitness value. Each point on the plot represents a combination of suction variables attempted during the optimization process.

Making use of the Multi-Dimensional Scaling (MDS) technique makes it easier to identify regions or clusters of points [37]. This is achieved by visualizing the pairwise dissimilarities or similarities between a set of objects in a lower-dimensional space, typically 2D.
Before delving further, it is imperative to mention that the variables used as input in MDS are rescaled to range between 0 and 1. This rescaling is crucial to prevent issues that may arise when variables have different orders of magnitude.
Upon implementing this change, the difference becomes readily visible, as does the optimization

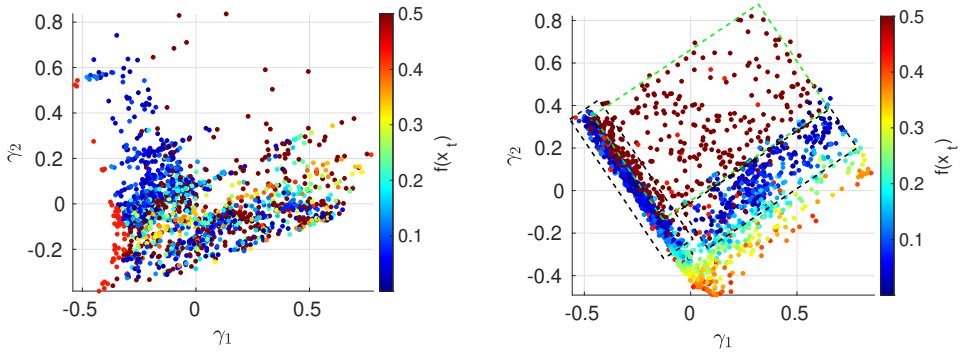

(a) MDS with primitive variables (x_s, x_e, v_w)

(b) MDS with LFC embedded variables (x_m, d, q)

Figure 6.4: Suction configuration in a 2D space with point color coded according to the fitness function value $f(\boldsymbol{x})$. The dimension reduction is obtained through MDS

output shown in figure 6.4. Two regions, indicated by the black dashed rectangles in figure 6.4 b, emerge. In these regions the fitness values are lower than in the surrounding areas. Additionally, the non-valid values (to reiterate, representing cases where no intersection or envelope curves go negative) are clustered, within the green dashed rectangle, in the top-right corner of figure 6.4 (b).

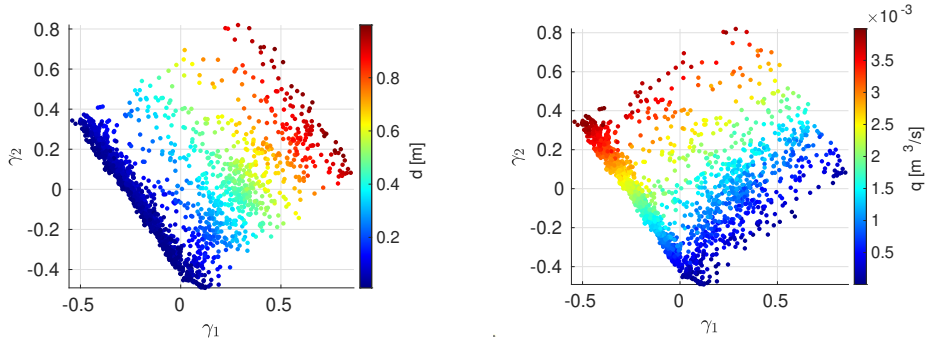

(a) MDS color-coded according to the extension of the suction region.

(b) MDS color-coded according to volumic mass flow rate

Figure 6.5: Multi dimensional scaling representation

After a closer examination, it becomes evident that the plane defined by γ_1 and γ_2 is essentially a rotation of the *q-d* plane, as illustrated in Figure 6.5. Therefore, it is more convenient to represent the optimization output on a *q-d* plane (Figure 6.6). For the sake of clarity, only the best solutions are retained in the representation of Figure 6.6, meaning all solutions with a fitness value below 2% are included, while the remaining configurations are filtered out.

$$f(\boldsymbol{x}_{opt}) \leq 0.02 \tag{6.5}$$

The reasons for this choice are manifold, starting with considerations about the physics and the model employed to estimate the transition.

Even though the transition prediction method identifies the point where the flow trips to turbulent, it has been emphasized in the section 2.3 and 2.4 that transition occurs over a region, typically referred to as a transition region. To account for this and acknowledge that transition is not abrupt, but rather develops along an interval Δx_t, it is possible to adopt a more flexible approach regarding the optimal values. Instead of strictly considering the optimum as the point where $x_t = L$ and $f(x_t = L) = 0$, we can introduce an optimal range of transition points where $|x_t - L| < 2L/100$ and the fitness function $f(x) < 2\%$. By adopting this approach, we try to make amend for the approximation it was made by reducing the transition region to a single transition point x_t.

Secondly, it is crucial to remember that the e^N method is merely a means to model the transition position, and like any estimation, it involves some level of approximation. Consequently, it is illogical to disregard solutions that predict transitions within the range of accuracy of the model [7].

As a final consideration, even if the transition location computed by the model was correct, we can accept transitions within $|x_t - L|/L < 2\%$.

As previously mentioned, the filtered solutions are now depicted in a q-d plane, shown in Figure 6.6. The color scale, which maps data values into the colormap, has been adjusted, with the color red now indicating a fitness value of 2%.

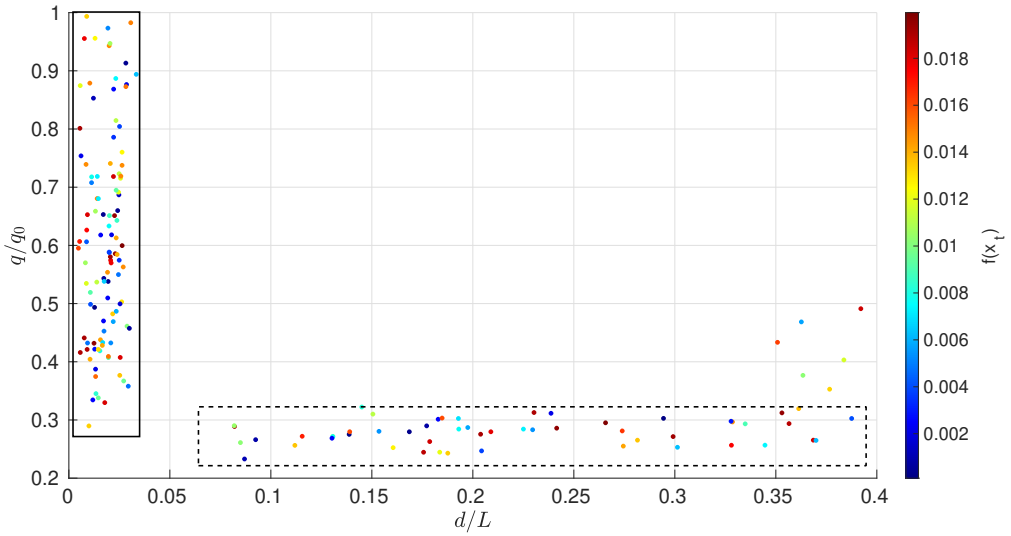

Figure 6.6: Optimal configurations ($f(\boldsymbol{x}) < 0.02$) in q-d plane. Here two groups of configurations are visible, and highlighted by the rectangles. $q_0 = 4 \times 10^{-3}$ $[m^3/s]$ is the maximum mass flow rate allowed

Crucial insights can be drawn from figure 6.6. All the points depicted in the figure allow for a transition very close to the trailing edge (TE). However, in delaying transition, some configurations demonstrate greater efficiency than others.
While for suction slot widths d/L in the range between 0.08 and 0.32, the points are densely clustered around the mean value $q/q_0 \sim 0.25$ (dotted rectangle in figure 6.6), for d/L less than 0.05 (solutions inside the solid rectangle), the mass flow q/q_0 associated with the best-performing configuration can range from 0.3 to 1. Relying on the physical intuition that energy consumption is a monotonic growing function of mass flow, configurations with $d/L < 0.05$ delay transition at the cost of higher power consumption.

A legitimate objection that someone could raise is that the sudden increments of mass flow requested by suction configuration with $d/L < 0.05$ may be due to the no longer validity of the boundary layer assumptions.

According to Schlichting [30], the validity of the boundary layer hypothesis extends until the suction velocity, relative to the undisturbed flow velocity U_∞, reaches approximately $1/\sqrt{Re} \sim 6 \times 10^{-4}$.

$$\frac{d}{L} \sim 0.2 \rightarrow \frac{v}{U_\infty} = \frac{q_0}{dU_\infty} \sim \frac{10^{-3}}{0.5\,15} = 1.3 \times 10^{-4} \tag{6.6}$$

$$\frac{d}{L} \sim 0.02 \rightarrow \frac{v}{U_\infty} = \frac{q_0}{dU_\infty} \sim \frac{10^{-3}}{0.05\,15} = 1.3 \times 10^{-3} \tag{6.7}$$

By employing the first-order estimations provided in equations 6.6 and 6.7, it becomes apparent that reliance on the results for suction over regions of length $d/L \sim 0.2$ is justified, as they adhere to the boundary layer hypothesis outlined above. However, when suction configurations possess a value of $d/L \sim 0.02$, the boundary layer hypothesis is no longer valid. Consequently, doubts may arise regarding the validity of the flow field provided by the BLES in such scenarios.

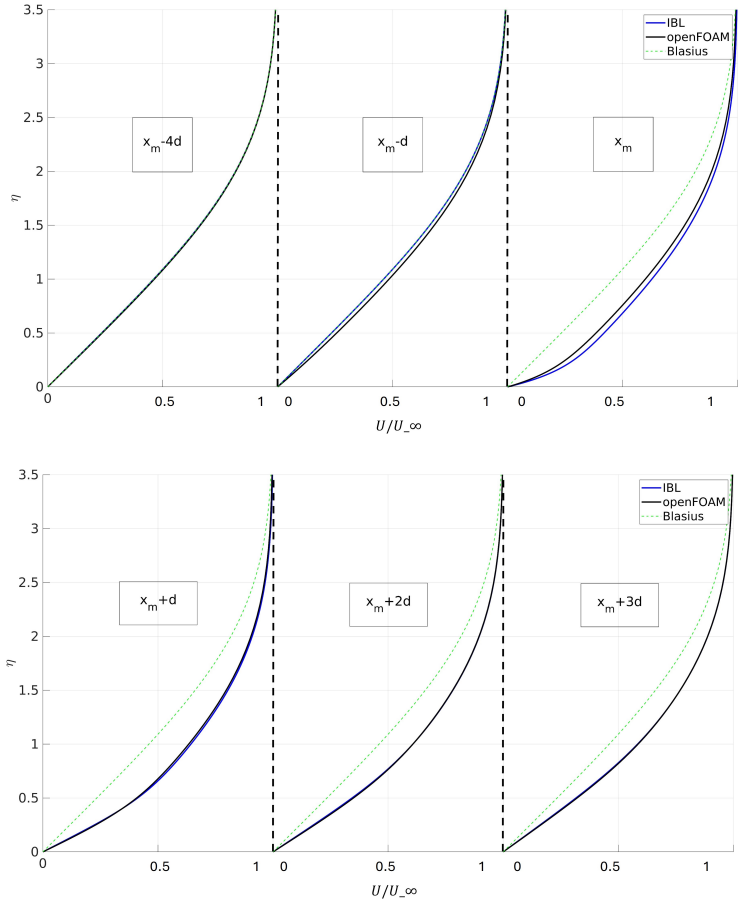

Figure 6.7: Comparison between BLES velocity profile and openFOAM profiles, at 6 different locations both upstream and downstream suction locations. On the x axis the normalized velocity, while η represents the non dimensional wall normal distance according to Blasius normalization.

In essence, the question to be addressed pertains to why the mass flow remains constant for almost all slot widths except for the low-amplitude slot. Hence, it is plausible that deviations from the BL hypothesis could lead to incorrect computations of the velocity profile. It is conceivable that the BLES velocity profiles may be less stable than the real velocity profiles under the same suction conditions, thereby necessitating more mass flow to compensate for these inaccuracies.

By solving the Navier-Stokes equation, could we achieve the same effect in terms of the transition with $d/L \sim 0.02$ and $q/q_0 \sim 0.25$?
To verify this hypothesis, a comparison between the velocity profiles provided by BLES and openFOAM was performed. Specifically, a single case was selected from all configurations with $d/L < 0.05$.

Far from the suction slot location(x_m-4d), the non-dimensional velocity profiles, normalized according to Blasius, exhibit good agreement with each other and align well with the analytical

Blasius profile. As we approach the slot (x_m-d) the two profiles start differing from each other. While the effect of the suction is felt only downstream the location of start suction for BLES, in OF the suction also affects the edge pressure distribution ahead of the suction location resulting in a favorable pressure gradient

Now, it is worth asking why the best results are consistently obtained with almost a fixed value of mass flow and whether this statement can be reversed. For example, do all configurations within the optimal mass flow rate, regardless of the suction location, lead to a transition at the end of the plate? Proceeding step by step, let's examine the effect of constant mass flow over the stability curves, selecting among the 1600 configurations provided by the optimization process the ones that have the optimal mass flow rate of $q/q_0 \sim 0.25$. The envelope curves are shown in figure 6.8 leading to two important considerations. First, a direct answer to the above question is provided. Among the envelopes shown in the figure 6.8 and associated with configurations with optimal mass flow, only a few allow transition close to the TE. Therefore *all optimal solutions for transition control have a mass flow around* $q/q_0 \sim 0.25$*, but not all the configurations with* $q/q_0 \sim 0.25$ *are optimal.*

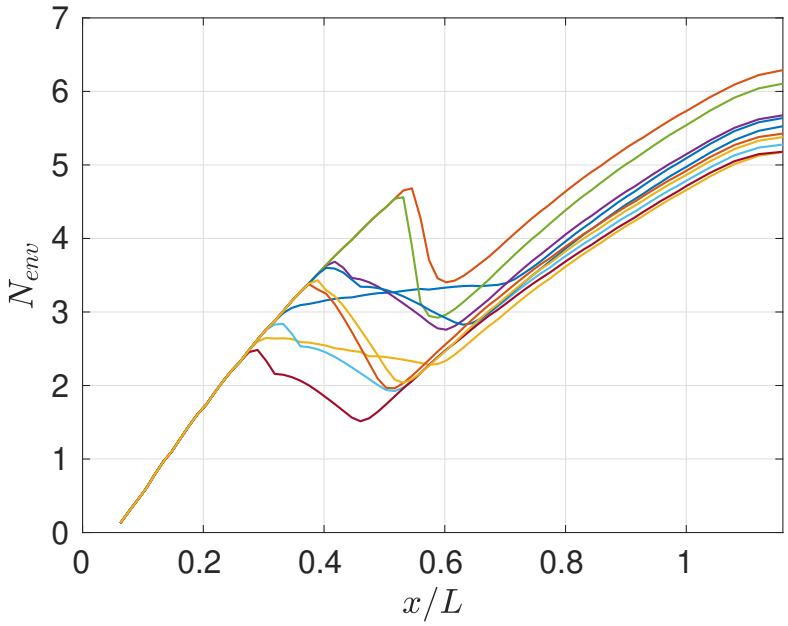

Figure 6.8: Some of the N_{env} at $q/q_0 \sim 0.25$ selected from the data set produced by the optimization.

More importantly, it is clear that, at constant mass flow, the portion of the N envelope curves downstream the suction location, has the same development regardless of the suction configuration. This appears evident looking figure 6.8, where the last growing portion of the envelopes run parallel, without crossing each other. In mathematical words, let's define a curve N*(x/L).

$$\{\forall \boldsymbol{x_k} \in \Omega_f \mid q_k = const \; \exists \; \delta_k \; s.t. \; N\left(\frac{x}{L}\right) = -\int_{\frac{x-e+dx}{L}}^{\frac{x}{L}} \alpha_i d\left(\frac{x}{L}\right) - \delta_k \in \left[\frac{x}{L}, N^*\left(\frac{x}{L}\right)\right], \; x > x_e\} \tag{6.8}$$

Carefully analyzing the implications, stating that the N_{env} curves have the same evolution essentially means they feature integrands of similar magnitude. This is because the curves are obtained by taking the envelope of the integral of the imaginary part of the eigenvalue dominant root (DR) over the length x.

$$N_{env}(x) = \max_{\omega} - \int_{x_0}^{x} \alpha_i(x, \omega) dx \tag{6.9}$$

Since the DRs are obtained solving the OS equation that depends on ω, Re_{δ_1}, $(U(x,y)/U_e(x))$, $(\partial^2 U(x,y)/\partial y^2)(\delta_1^2/U_e(x))$, to obtain the same DRs the OS equation should possess the same input values. Thus, for a fixed mass flow, we should expect the dimensionless velocity and its second derivative to be independent of the suction location sufficiently downstream from the slot.

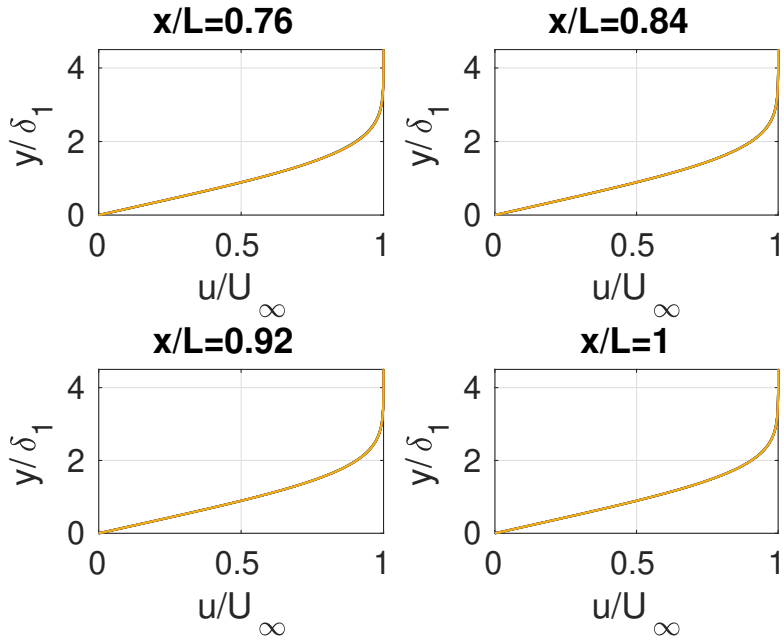

Figure 6.9: Normalized velocity at four different locations for $q/q_0 \sim 0.25$. Same amount of curves as in figure 6.8. The configurations associated with each curve vary in suction slot location and extension.

The intuition was confirmed by data shown in figures 6.9, 6.10, 6.11.

Let's consider 2 different values of mass flow of $q/q_0 \sim 0.25$ and $q/q_0 \sim 0.375$. We expect that the curves that feature the same mass-flow value will have the same slopes (DRs) at the same point. On the contrary, those featuring different mass-flow values will have different slopes (see Figure 6.12). Therefore, envelopes that belong to the same mass flow family never bump into each other, while taking two envelopes from the two mass flow groups it is probable that they may intersect at some point.

The last and, maybe, more valuable evidence that we bring to support the thesis about the dependence of the N envelopes on the mass flow is depicted in figure 6.13. On the left there are the envelopes associated with each point of figure 6.6. On the right only the one with a mass

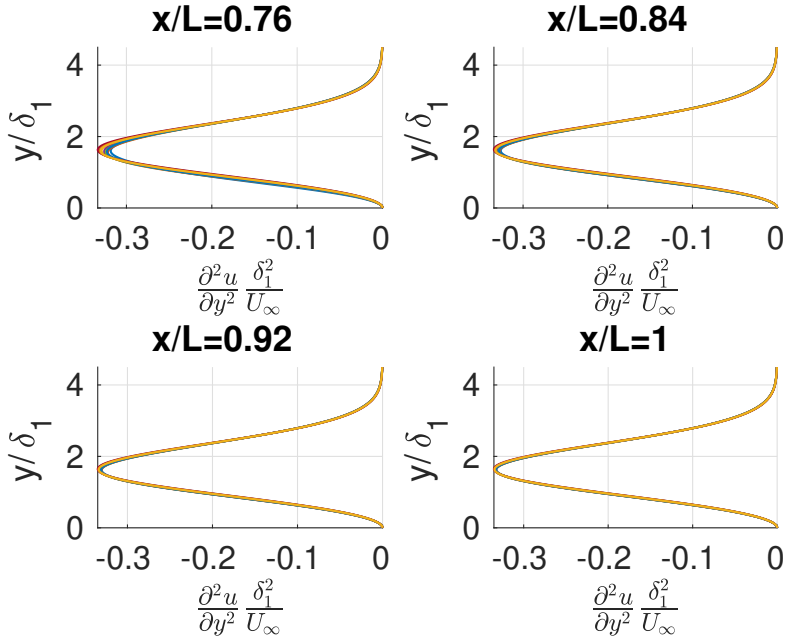

Figure 6.10: Normalized velocity second derivatives profiles at four different locations for $q/q_0 \sim 0.25$. Same amount of N_{env} curves as in figure 6.8. The configurations associated with each curve vary in suction slot location and extension.

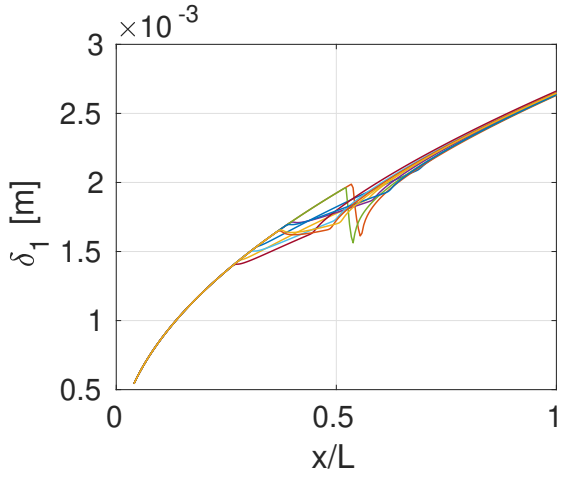

Figure 6.11: Displacement thickness along the plate for $q/q_0 \sim 0.25$ is depicted, with the same number of N_{env} curves as in Figure 6.8. The configurations associated with each curve vary in suction slot location and extension.

flow:

$$\frac{q^* - \Delta q}{q_0} \leq \frac{q}{q_0} \leq \frac{q^* + \Delta q}{q_0} \tag{6.10}$$

With $\frac{q^*}{q_0} = 0.275$ and $\frac{\Delta q}{q_0} = 0.1250$. While on the left side the evolution of the envelope looks

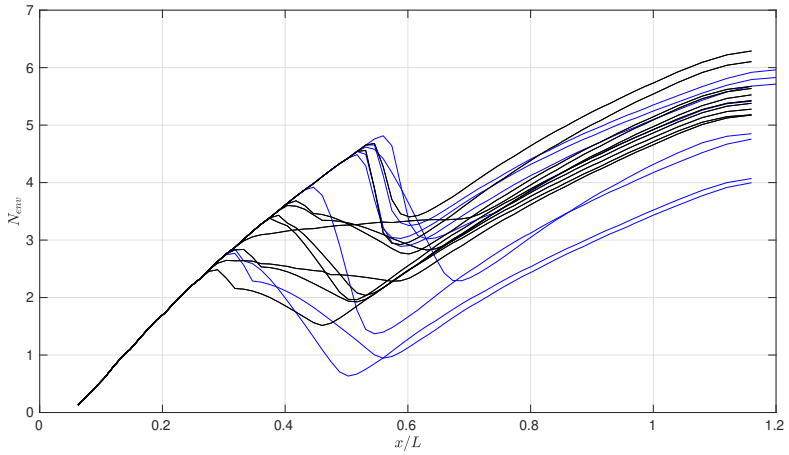

Figure 6.12: N_{env} of two different families of curves. The blues are associated with $q/q_0 \sim 0.375$ while the black ones to $q/q_0 \sim 0.25$

chaotic, upon retaining only the envelopes that satisfy the above relation, it can be seen that the envelopes collapse into a tight bundle(figure 6.13 (b)).

Taking into account everything that has been previously stated it is possible to conclude:

- There are theoretically an infinite number of combination that can lead transition to happen in a desired point, like the TE;
- Among these infinite configurations, the ones that are energetically advantageous feature large slot width.
- Being aware of the optimal flow rate value to apply is not exhaustive for achieving effective transition control. An incorrect coupling of this value with an unsuitable geometry can undermine the efficiency of active flow control(AFC).

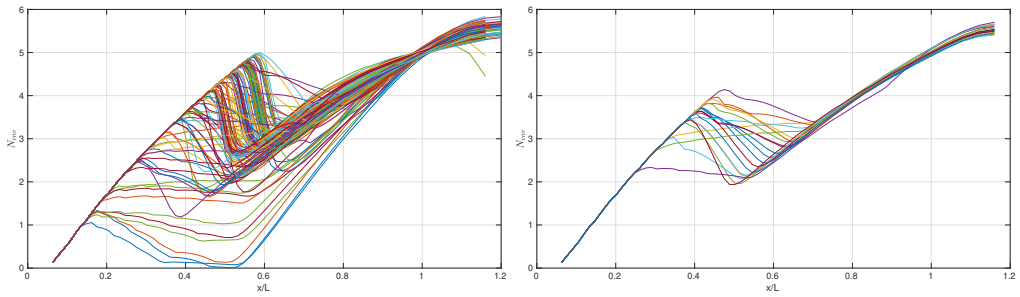

(a) Optimal envelope given by the optimization (b) Optimal envelope with the same mass flow

Figure 6.13: Comparison between the optimal envelope and the envelope obtained with a constant mass flow spillage.

6.2 AFC effects on friction drag

6.2.1 Drag increments?

Whenever boundary layer control is applied through suction, a local increase in skin friction coefficient is observed (already pointed out in Figure 5.4), leading to an overall rise in drag force. The drag, defined per unit depth, is given by the equation:

$$D = \int_0^L \mu \frac{\partial u(x, y = 0)}{\partial y} dx \tag{6.11}$$

Here, the parameter Drag Increment (DI) represents the increment in skin friction drag compared to the enforced laminar flow:

$$DI = \frac{D_{act} - D_{base}}{D_{base}} \tag{6.12}$$

Despite the highest value of mass flow rate is only $q_0 = 4 \times 10^{-3}$ $[m^3/s]$, the maximum drag increments that can be reached is in the order 20%, as figure 6.14 testifies. Keeping in mind the ultimate goal of reducing the drag force on the flat plate, observing drag growth seems to contradict the initial intentions. To avoid confusion, it is wise to provide the proper interpretation of the phenomenon.

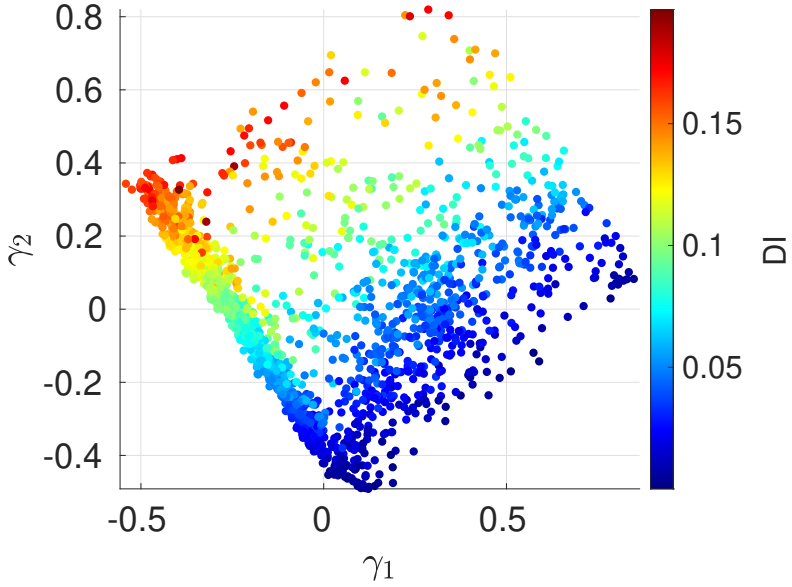

Figure 6.14: DI is shown for each point computed during the optimization.

Linear stability analysis requires a base laminar flow to perform stability calculations. The solution we have seen so far like BL thickness, friction coefficients or wall shear stresses, mainly presented in section 5.0.1, refers to an enforced laminar solutions. We call it enforced because BLES is **only** able to provide to us laminar solutions. For instance, when considering a flat plate of length L exposed to a free stream velocity U_∞, BLES computes a laminar flow from the leading edge (LE) to the trailing edge (TE). However, departing momentarily from numerical considerations and delving into the physics, it is recognized that over a sufficiently long flat plate,

the flow initiates as laminar and transitions to turbulence at a certain point x_t. While BLES models flow characteristics within the laminar regime, it cannot encapsulate turbulent flow over the final portion of the flat plate. Consequently, if transition occurs, the distributions depicted in the figures 5.2, 5.3 and 5.4 are inaccurate beyond the transition point. Furthermore, the observed increments in total friction drag (DI) stem from the comparison with a hypothetical baseline laminar solution, which does not exist in reality. It is imperative for the author to emphasize this concept, as a cursory examination of the above listed figure might lead to erroneous conclusions.

6.2.2 Drag Reduction

By setting the critical N factor to 5, the transition is located about at $x_t/L = 0.58$. This results in a laminar flow that extends from the leading edge up to the transition point, beyond which a turbulent flow follows.

The coexistence of these two flow states requires different approaches. In the laminar region, the friction coefficient is a direct consequence of the BLES velocity profile, which is known by solving the boundary layer equations.

$$\tau(x) = \mu \frac{\partial u}{\partial y}\bigg|_w \tag{6.13}$$

$$c_f = \frac{\tau(x)}{\frac{1}{2}\rho U_\infty^2} \tag{6.14}$$

When the flow transitions to turbulence, it is possible to rely on empirical expressions that connect c_f to Re_x [1].

$$c_f = 0.0576\left(\frac{\nu}{U_\infty x}\right)^{\frac{1}{5}}, \quad x > x_t \tag{6.15}$$

Figure 6.15 shows the comparison between the friction coefficient of a laminar flow that abruptly

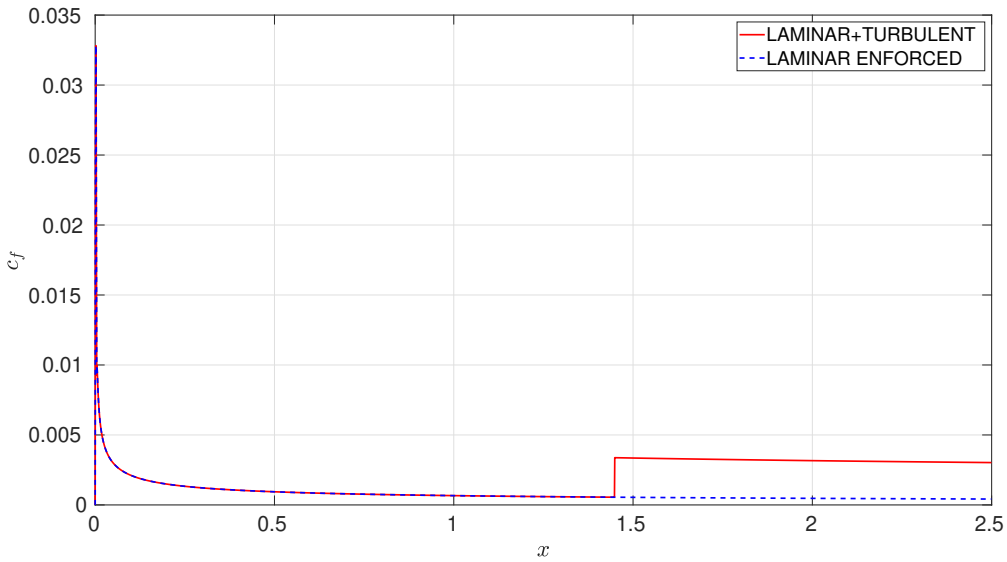

Figure 6.15: Friction coefficient of the laminar profile vs friction coeffient of the laminar + turbulent

turns into turbulent flow and the friction coefficient associated with the enforced laminar. From the point where turbulence starts, friction coefficient goes up by six to seven times compared to the laminar case.

Another parameter, called drag reduction is now introduced to estimate the benefits of the suction on the friction drag force:

$$DR = \frac{D_n - D_s}{D_n} \tag{6.16}$$

Where D_n stands for drag in natural transition scenario, estimated by the area below the red line in figure 6.15, previously multiplied by the free stream dynamic pressure $1/2\rho U_\infty^2$. D_s is the drag force when suction control is applied defined by:

$$D_s = \frac{1}{2}\rho U_\infty^2 \int_0^L c_f^s(x)dx \tag{6.17}$$

$$c_f^s(x) = \begin{cases} \frac{\tau_{BLES}(x)}{1/2\rho U_\infty^2} & x \leq x_t \\ c_f = 0.0576\left(\frac{\nu}{U_\infty x}\right)^{\frac{1}{5}} & x > x_t \end{cases} \tag{6.18}$$

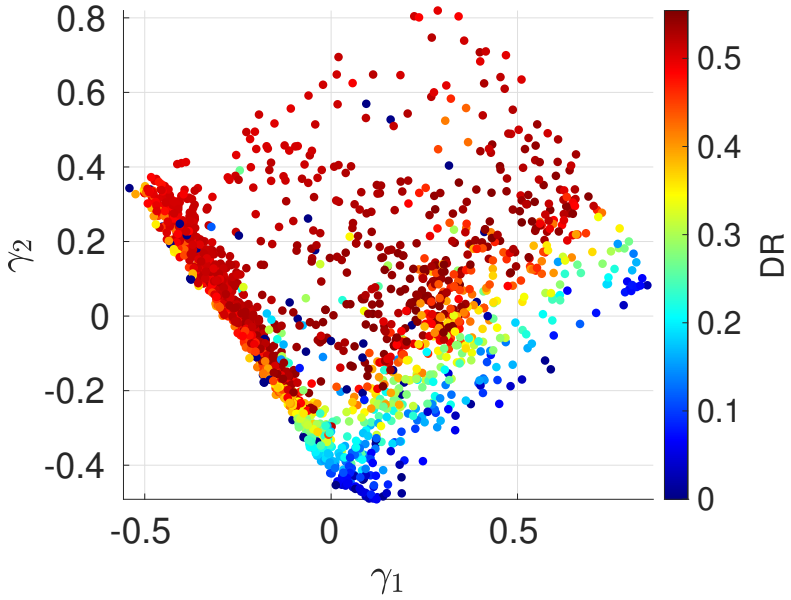

Figure 6.16: DR is shown for each point computed during the optimization.

In many cases,the application of Active Flow Control (AFC) leads to a noteworthy reduction in friction drag, as illustrated in Figure 6.16. The maximum achieved value of Drag Reduction (DR) peaks at approximately 55.4%, with the majority of suction configurations yielding DR values above 40%. Hence, even when employing non-optimal control over the transition position, a substantial reduction in drag is still realized.

It is beneficial to summarize the findings thus far, particularly regarding the criteria by which a suction configuration is deemed favorable. To achieve this, the dataset generated during the optimization process is partitioned into 10 groups based on the suction extension d. A suction

configuration i is assigned to the k-th group if:

$$\frac{k-1}{10}\frac{d_m}{L} < \frac{d_i}{L} \leq \frac{k}{10}\frac{d_m}{L} \tag{6.19}$$

$k = 1, ..., 10$ and $\frac{d_m}{L} = 0.4$. Each group has been filtered based on three criteria:

1. Transition location
$$\left|\frac{x_t - L}{L}\right| < \frac{2}{100}$$
2. Mass flow rate q
$$\frac{q}{q_0} \leq 0.375$$
3. DR
$$DR \geq 0.53$$

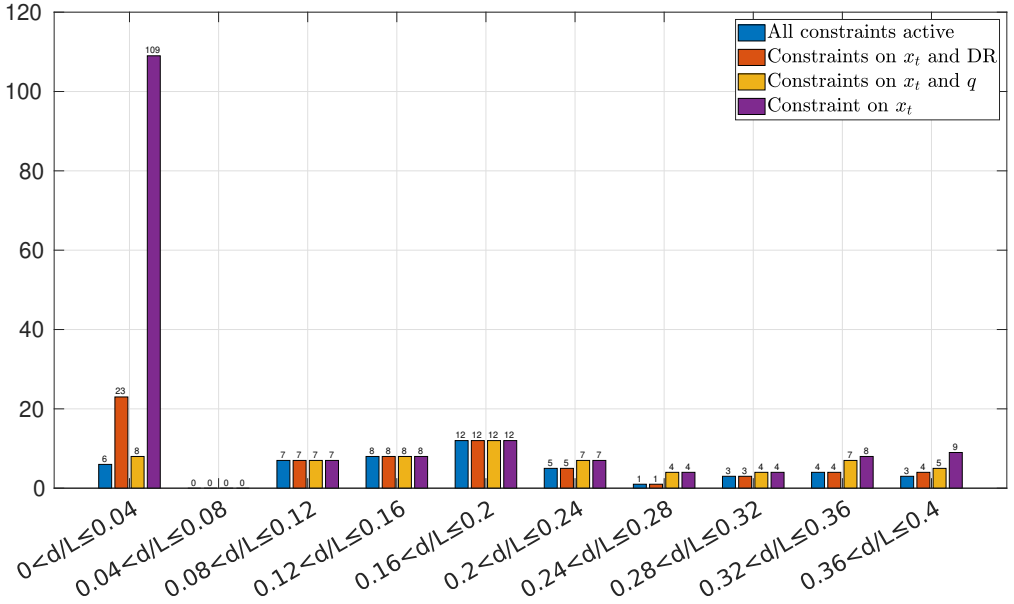

Figure 6.17: Within each group, the bar indicates the number of solutions that fulfill the constraints specified in the legend.

Figure 6.17 illustrates all the configurations that fulfill the above constraints. The most crucial constraint, always applied, is the one prescribing the transition location.

Although suction configurations belonging to the first group, as depicted in Figure 6.17, readily enable optimal transition control (with 109 valid cases), these configurations also exhibit the most disadvantageous mass flow rates. Indeed, Drag Reduction (DR) is closely related to x_t, but optimizing one does not necessarily optimize the other. This concept is particularly highlighted for the first group ($k = 1$), where 109 configurations satisfy the x_t constraint, deemed optimal for transition delay, but only 23 of them also permit a consistent DR.

Optimization hasn't produced any solution belonging to the second group. From the same graph, it can be observed that groups 3, 4, and 5 achieve a rate of success of 100%. All

configurations within these groups are optimal for transitions and adhere to the constraints regarding drag and mass flow. Without getting caught up in the excitement but rather being cautious, it doesn't imply that all the configurations within the 3-th, 4-th, and 5-th groups satisfy the above statement.

Constraint for the mass flow is always satisfied from the 3rd to the 8th group, but not for the last two groups.

6.3 Model for optimal LFC

The cumulative insights gathered from the preceding discussions indicate a potential avenue for creating a model capable of guiding the choice of the optimal suction parameters, given some initial information, without necessitating stability calculations.

When focusing specifically on the envelope, the curve can be deconstructed into three distinct segments, N^I_{env}, N^{II}_{env} and N^{III}_{env} shown in figure 6.18:

- The monotonic growth until the slot starting point:N^I_{env}
- A decreasing segment :N^{II}_{env}
- The second monotonic growth:N^{III}_{env}

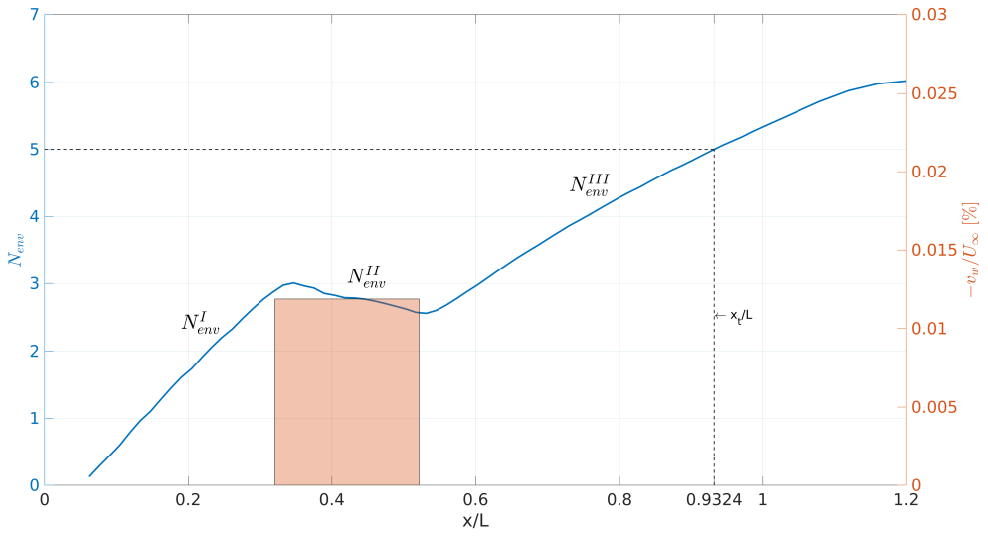

Figure 6.18: An example of an envelope curve provided to visually correlate each of the three segments with their respective names: N^I_{env}, N^{II}_{env}, and N^{III}_{env}.

6.3.1 Envelope modeling

The modeling of first the segment N^I_{env} is straightforward, as it remains the same as the envelope associated with the natural flow until the point where suction is applied.

The modeling process initiates by attempting to predict the effect of suction on the N envelope. Upon careful examination of Figure 6.13, three key observations emerge:

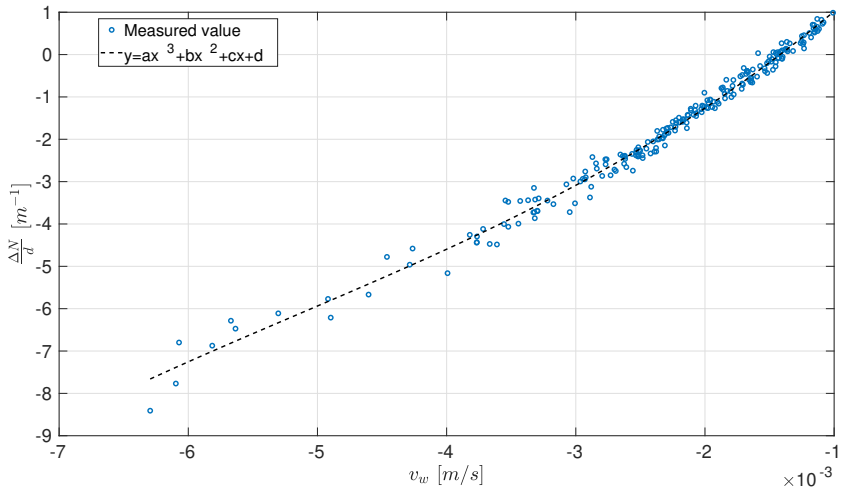

Figure 6.19: The slope of the N_{env}^{II} segment, denoted as $\frac{\Delta N}{d}$, is plotted as a function of the suction velocity v_w. The blue points on the graph signify the slopes computed from the optimization dataset, while the black line represents the the data points fitting curve.

- The decreasing part N_{env}^{II} can be reasonably approximated as a segment.
- The slope of this segment appears to be correlated with the suction velocity v_w. The segment slope increases alongside velocity.
- The final jump ΔN, for a fixed velocity, is primarily influenced by the slot width.

Figure 6.19 visually captures the relationship between $\Delta N/d$ and v_w, showing a cluster of data points that closely aligns with a curve well fitted by a cubic polynomial.

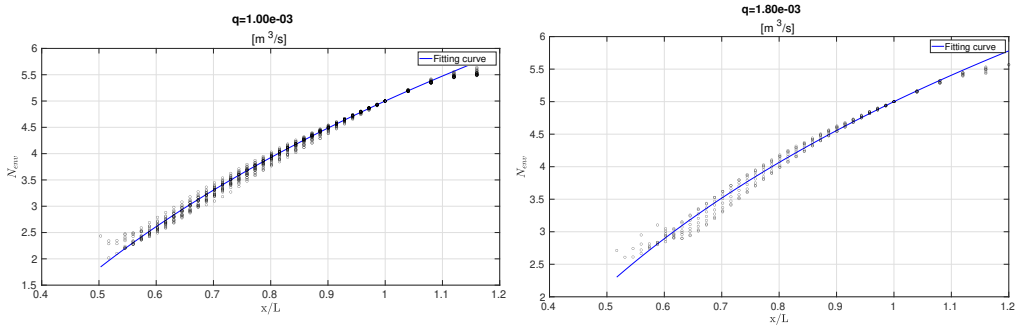

(a) $q/q_0 = 0.45$ (b) $q/q_0 = 0.25$

Figure 6.20: N_{env}^{III} evolution for two different groups of mass flow. The points are picked up from the data set produced by the optimization. Fitting curve expression is expressed by the equation 6.21.

The next step consists of modeling the last part N_{env}^{III}. It was highly stressed in the previous section how the evolution of the curve downstream of the suction slot is mainly dictated by the

mass flow rate. Given all the envelopes generated after the optimization process, it is possible to interpolate them to obtain a relation between the volumetric flow rate q and N_{env}. All the envelopes resemble the shape of

$$y \propto x^n \quad 0 \leq n \leq 1 \tag{6.20}$$

The curves are divided into different groups based on the mass flow. Subsequently, they are vertically translated such that the point $[x/L,\ N_{env}] = [1,\ 5]$ belongs to each curve. Finally, the curves are truncated to retain only the region between the ending of the suction slot and the flat plate trailing edge. With this post-processing, it becomes possible to fit each group of curves using a base function:

$$y = 5 + a(x^n - 1) \tag{6.21}$$

The point $[x, y] = [1,\ 5]$ also belongs to the base function.

As a result, a dependence of a and n on q is obtained. q is discretized from $q/q_0 = 0.25$ to $q/q_0 = 0.45$ with a step of $\Delta q/q_0 = 0.125$. Figure 6.21 displays the curve that fits the N_{env}^{III} for the different mass flow parameters q.

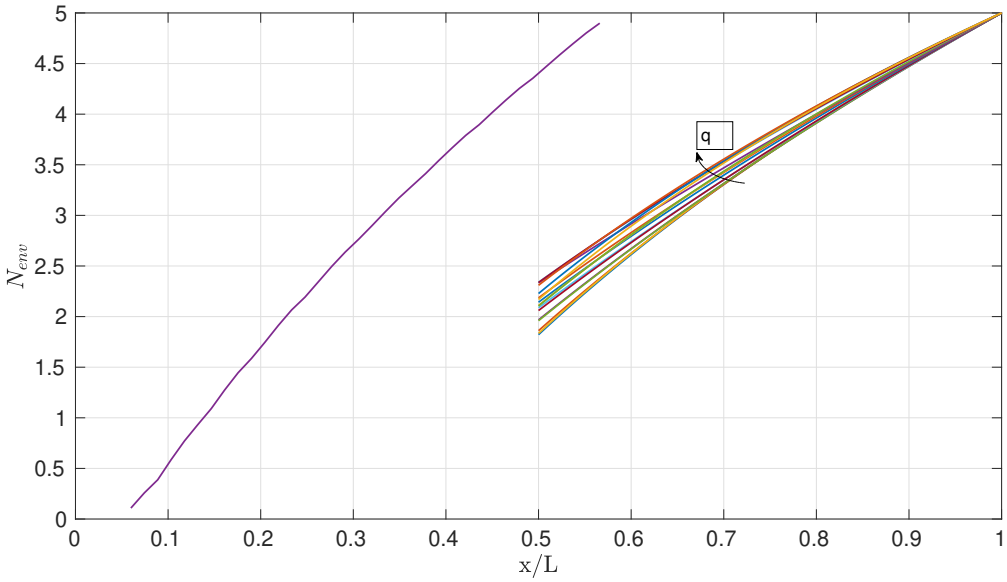

Figure 6.21: Ray of N_{env}^{III} curves for all mass flow analyzed

6.3.2 Application of the model

The benefits of using a low-fidelity model to predict the evolution of the envelope when suction control is applied are manifold. One immediate advantage is the ability to expedite the identification of optimal suction configurations without the need for an extensive optimization process. For instance, if two out of the three suction variables are known, the model can be utilized to determine the value that the unknown variable must assume to achieve optimal control.

To clarify the employment of the model for this task, it is advantageous to further simplify the representation by approximating the curves N_{env}^{III}, in Figure 6.21, as straight lines with a slope directly correlated the mass flow called q_2.

In a situation where we need to determine the optimal slot dimension based on the slot's starting position x_s and suction velocity v_w, the initial step involves identifying the point that

corresponds to the suction starting location on the N^I_{env} curve. Figure 6.22 visually depicts this point using a red square superimposed on the blue curve N^I_{env}.

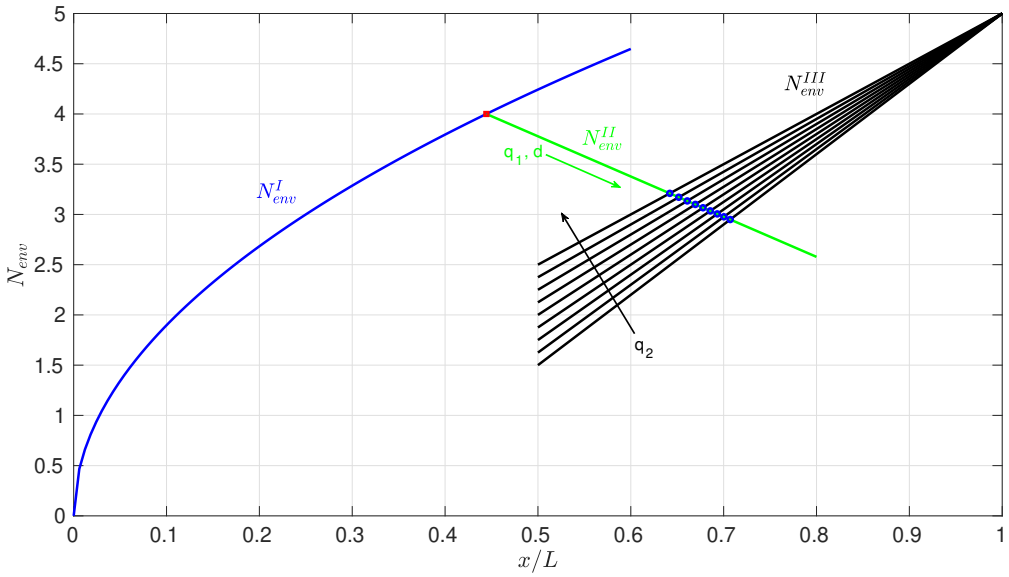

Figure 6.22: Sketch, not to scale and for demonstration purpose, of the envelope segments N^I_{env}, N^{II}_{env} and N^{III}_{env}. The blue line represents N^I_{env}. The red square the suction starting location. The green half-line the curve N^{II}_{env}, while the blue points different value of x_e/L. The black lines illustrates the optimal curves with the mass flow q_2 that allows to joint the blue points with $[x/L,\ N_{env}] = [1,\ 5]$.

Information about v_w immediately translate in the slope of the decreasing segment N^{II}_{env}. Knowing the slope of a line and the point that belongs to the line, the line is uniquely defined. These calculations will enable us to plot the green half-line in the figure 6.22. It is noteworthy that each point along the green line corresponds to a particular slot width and, consequently, a specific value of mass flow q_1.

$$q_1 = -v_w d \tag{6.22}$$

By selecting a point along the green line N^{II}_{env}, a curve N^{III}_{env} starting from that point can be drawn (the dotted green line in figure 6.23), which is characterized by the mass flow q_1. However, not all points on this curve pass through $[x/L,\ N_{env}] = [1,\ 5]$, as only one value of d can make the combination of (x_s, d, v_w) optimal.

Furthermore, it is possible to connect each point along the N^{II}_{env} with the point $[x/L,\ N_{env}] = [1,\ 5]$ and determine the mass flow q_2 that would have to be sucked to achieve the critical N^{crit}_{env} on the trailing edge. The black lines in figure 6.22 depict this scenario. Therefore, the optimal d value is the one that allows a proper connection between the blue line N^I_{env} and one of the black lines N^{III}_{env} through the green line N^{II}_{env}.

In essence, each blue point on the green line N^{II}_{env} corresponds to two N^{III}_{env} lines or two mass flows (refer to figure 6.24). The first is the green dotted N^{III}_{env} with $q = q_1$, which is followed in practice when x_e/L coincides to the blue point, while the second is the black N^{III}_{env} with $q = q_2$, which we strive to achieve. In the optimal configuration, these lines would coincide, as demonstrated in figure 6.24.

$$d_{opt} = \min_d(|\ q_1 - q_2\ |) \tag{6.23}$$

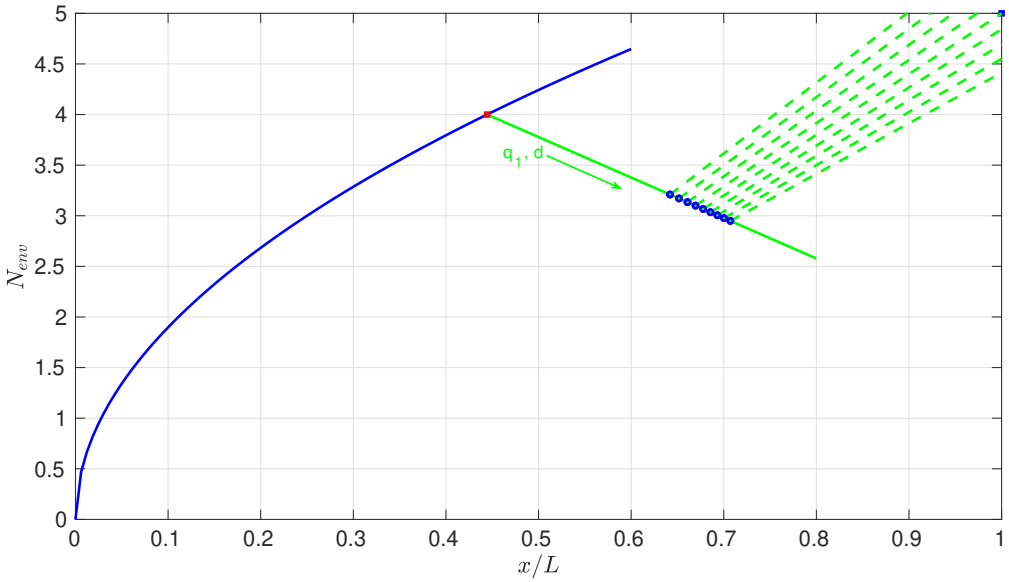

Figure 6.23: For demonstration purposes, a sketch (not to scale) of the envelope segments N^I_{env}, N^{II}_{env}, and N^{III}_{env} is provided. The blue line represents N^I_{env}. The red square denotes the suction starting location. The green half-line represents the curve N^{II}_{env}, while the blue points denote different values of x_e/L. The green dotted lines illustrate the evolution of N^{III}_{env} associated with a mass flow $q = q_1 = -v_w d$.

The algorithm that leads to the estimate of the third unknown parameter starts with finding the intersection between the black curve N^{III}_{env} and the green line N^{II}_{env}. This intersection is highlighted by blue points in figure 6.22. Each point is characterized by two mass flows q_1 and q_2. The point that minimizes the absolute difference among q_1 and q_2 is the optimum.

6.3.3 Model Validation

The created model was subsequently tested on 400 randomly generated configurations, divided into 4 groups of 100 cases each. The only imposed limits concern the slot width, $0.08 \leq d/L \leq 0.32$, and also regarding the upper bound of x_s/L, by imposing $x_s/L < x_t^N$. To validate the model the two suction variables (x_s, v_w) are given as input to the model which provides in output the third missing variable d in order to have $x_t^{model} = L$. Given d, x_e is a consequence since $x_e = x_s + d$. Then, using the same numerical framework we employed in the optimization (BLES + LST + FILTER + e^N), we compute more accurately the transition position x_t and we take that as ground truth.

The validation metric used to estimate the error is the following:

$$\varepsilon = \frac{\mid x_t^{model} - x_t \mid}{L} = \frac{\mid L - x_t \mid}{L} = f(x_t) \tag{6.24}$$

The fitness value from the numerical framework is therefore a good metric to estimate the quality of the model predictions.

The validation results summarized in table 6.1 are promising. The average error $\varepsilon \simeq 1\%$, below the thresholds of 2% imposed to distinguish the best solutions from the others. Also the standard deviation of the 4 groups is low, showing that most of the solutions predicted have a

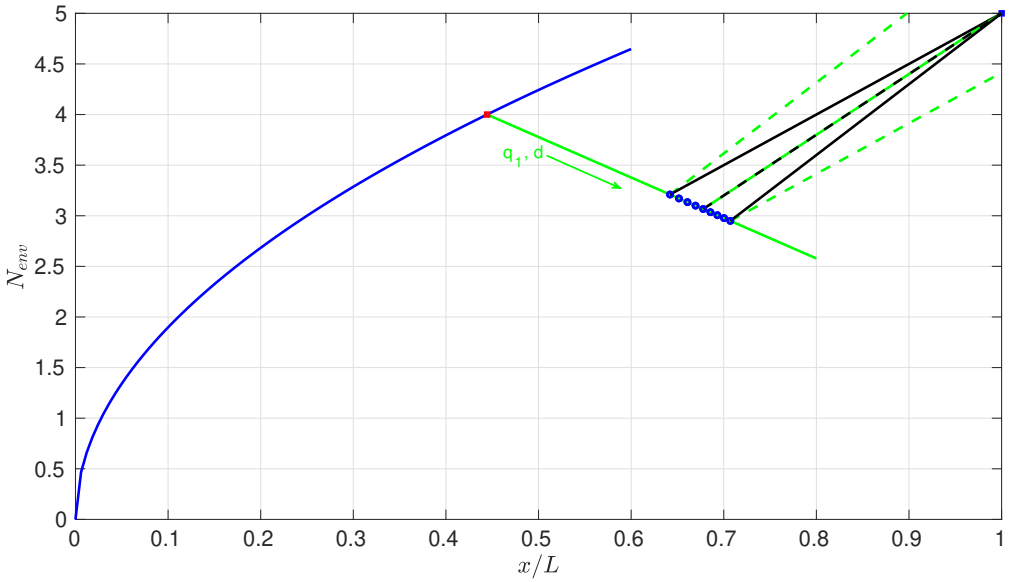

Figure 6.24: Sketch, not to scale, for demostration purpose, of the envelope segments N^I_{env}, N^{II}_{env} and N^{III}_{env}. The blue line represents N^I_{env}. The red square the suction starting location. The green half-line the curve N^{II}_{env}, while the blue points different value of x_e/L. The green dotted lines model the evolution of the N^{III}_{env} associated with a mass flow $q = q_1 = -v_w d$. The black lines illustrates the optimal curves with the mass flow q_2 that allows to joint the blue points with $[x/L,\ N_{env}] = [1,\ 5]$.

fitness value close to the mean. The maximum error found was around 2.5%, slightly above the aforementioned 2%.

	$\overline{\varepsilon}$	σ	$max(\varepsilon)$	$min(\varepsilon)$
pool 1	9.3069e-03	6.8146e-03	2.5327e-02	5.5417e-04
pool 2	9.0666e-03	6.2794e-03	2.4918e-02	2.5499e-04
pool 3	9.4706e-03	5.6639e-03	2.4993e-02	5.9267e-04
pool 4	1.0519e-02	7.1232e-03	2.5820e-02	2.2950e-05

Table 6.1: The average, standard deviation, maximum and minimum value of the error defined by the eq. 6.24 is shown from columns two to five. The rows refer to the group under investigations

To show the variety of suction configuration tested, in terms of position, slot amplitude and velocity, some of them are shown in figure 6.25 .

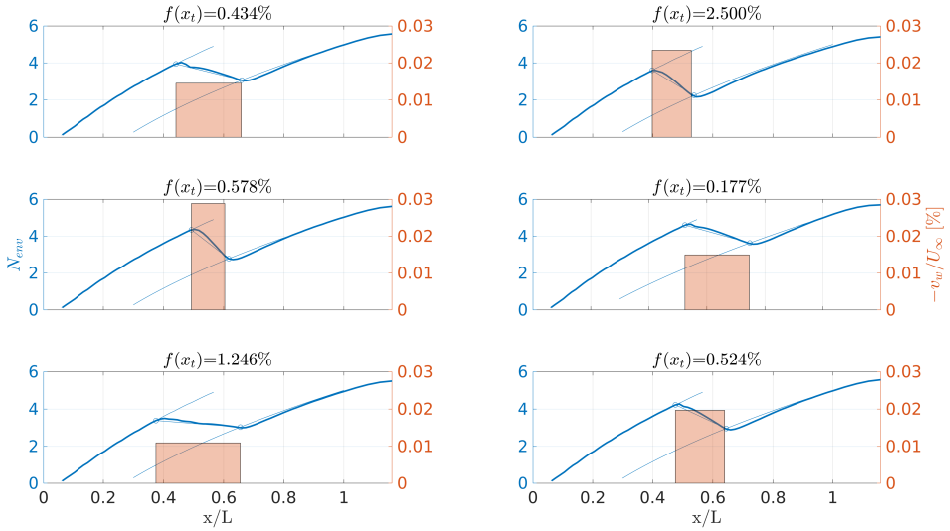

Figure 6.25: 6 comparison between the envelope produced through the model(thin magenta lines) and the numerical framework (blu curves) are shown. Each sub-figure shows different suction configurations, expressed by the orange rectangle. The vertical edge of the rectangle express the suction boundaries while the height of the rectangle is related to the suction velocity. The number above the figures $f(x_t)$ indicates the error committed by the model.

Chapter 7

Conclusion and outlooks

In order to maximize the achievable transition delay, an optimization of 3 flow control parameters (suction velocity v_w and upstream x_s and downstream x_e boundaries of the LFC region) was carried out by means of the Bayesian optimization approach. More than 1600 different permutations of the control parameters were evaluated. To distill the effect of the considered LFC parameters on the transition position, a multi-dimensional scaling of the input parameters was performed. Results indicate the existence of multiple optimal configurations, that can be further divided into two groups. In one group, suction is applied in a small region, that can be identified by $d/L < 0.05$. Solutions that belong to the second group are characterized by mass flow values similar to each other.

It was also observed that the evolution of the envelope downstream of the suction locations is mainly dependent on the mass flow spilled by the suction, and almost independent from the suction location or extension. Closer observations of the results showed that in the regions where suction is performed, the envelope decreases almost linearly, with a slope that is function of the suction velocity, uniform inside the suction regions. The combination of the above discoveries led to the proposal of a model that allows for accounting directly for the suction effect on the envelope. Given two out of three suction parameters, the model was used to estimate the value of the missing one to have the best suction control. The model was validated against the same numerical framework used during the optimization. The validation showed promising accuracy of the model predictions. The utility of the proposed model is to estimate, in a first analysis, a good starting point for either the design of a LFC setup or for a LFC optimization process.

Drag analyses performed using empirical correlations showed that a small amount of suction can produce up to 55% of drag reduction DR, compared to the case of natural transitions.

The influence of the slot dimension on different variables such as transition point x_t, mass flow q, and DR was studied. Even though for the transition, all slot dimensions were revealed as suitable, when analyzing the mass flow it is evident that the small slots require a larger mass flow to delay the transition, while to have a good drag reduction, it is better to employ suction over a width between $8\% \leq d/L \leq 20\%$.

Future work about the influence of suction on transition could involve the investigation of nonuniform suction velocity on stability and therefore transition. Validation of the numerical framework also to the case of the Falkner-Skan velocity profile allows the numerical framework to analyze the airfoil BL stability, where favorable and adverse pressure gradients are present. Moreover, validation of the results with advanced numerical techniques, specifically RANS with γ-Re_θ closure model, is still ongoing.

Bibliography

[1] Renzo Arina. *Fondamenti di aerodinamica*. Levrotto & Bella, 2015.

[2] S Bake, DGW Meyer, and U Rist. Turbulence mechanism in klebanoff transition: a quantitative comparison of experiment and direct numerical simulation. *Journal of Fluid Mechanics*, 459:217–243, 2002.

[3] AL Braslow. History of suction-type laminar-flow control with emphasis on flight resrearch: Monographs in aerospace history number 13. Technical report, 1999.

[4] Guy P Brasseur, Mohan Gupta, Bruce E Anderson, Sathya Balasubramanian, Steven Barrett, David Duda, Gregg Fleming, Piers M Forster, Jan Fuglestvedt, Andrew Gettelman, et al. Impact of aviation on climate: Faa's aviation climate change research initiative (accri) phase ii. *Bulletin of the American Meteorological Society*, 97(4):561–583, 2016.

[5] TJ Bridges and Philip John Morris. Differential eigenvalue problems in which the parameter appears nonlinearly. *Journal of Computational Physics*, 55(3):437–460, 1984.

[6] Dan Chen, Minghua Hu, Ke Han, Honghai Zhang, and Jianan Yin. Short/medium-term prediction for the aviation emissions in the en route airspace considering the fluctuation in air traffic demand. *Transportation Research Part D: Transport and Environment*, 48:46–62, 2016.

[7] Michelangelo Corelli Grappadelli, Stephan Sattler, Peter Scholz, Rolf Radespiel, and Camli Badrya. Experimental investigations of boundary layer transition on a flat plate with suction. In *AIAA Scitech 2021 Forum*, page 1452, 2021.

[8] William O Criminale, Thomas Luther Jackson, and Ronald Douglas Joslin. *Theory and computation in hydrodynamic stability*. Cambridge University Press, 2018.

[9] Gökhan Danabasoglu and Sedat Biringen. A chebyshev matrix method for the spatial modes of the orr–sommerfeld equation. *International journal for numerical methods in fluids*, 11(7):1033–1037, 1990.

[10] Dimitris Fouskakis and David Draper. Stochastic optimization: a review. *International Statistical Review*, 70(3):315–349, 2002.

[11] Jens HM Fransson. *Flow control of boundary lagers and wakes*. PhD thesis, KTH, 2003.

[12] Peter I Frazier. A tutorial on bayesian optimization. *arXiv preprint arXiv:1807.02811*, 2018.

[13] Roman Garnett. *Bayesian optimization*. Cambridge University Press, 2023.

[14] Hui Guo, Qi Xiang Lian, Yan Li, and Hai Wen Wang. A visual study on complex flow structures and flow breakdown in a boundary layer transition. *Experiments in Fluids*, 37:311–322, 2004.

[15] ZhangFeng Huang and Xuesong Wu. The effect of local steady suction on the stability and transition of boundary layer on a flat plate. In *8th AIAA Flow Control Conference*, page 3471, 2016.

[16] Ronald D Joslin. Aircraft laminar flow control. *Annual review of fluid mechanics*, 30(1):1–29, 1998.

[17] Iu S Kachanov, VV Kozlov, and V Ia Levchenko. Occurrence of tollmien-schlichting waves in the boundary layer under the effect of external perturbations. *Akademiia Nauk SSSR Izvestiia Mekhanika Zhidkosti i Gaza*, 13:85–94, 1978.

[18] Yury S Kachanov. Physical mechanisms of laminar-boundary-layer transition. *Annual review of fluid mechanics*, 26(1):411–482, 1994.

[19] HB Keller. Numerical methods for two-point boundary value problems. *Blaisdell*, 1968.

[20] VV Kozlov, VIA LEVCHENKO, VP Maksimov, AL Rudnitskii, and VA Shcherbakov. Investigation of viscous fluid flow at a suction slit. *TsAGI, Uchenye Zapiski*, 8(1):130–135, 1977.

[21] KSG Krishnan, O Bertram, and O Seibel. Review of hybrid laminar flow control systems. *Progress in Aerospace Sciences*, 93:24–52, 2017.

[22] John Laufer and Thomas Vrebalovich. Stability and transition of a supersonic laminar boundary layer on an insulated flat plate. *Journal of Fluid Mechanics*, 9(2):257–299, 1960.

[23] Sunhyuk Lim and Facundo Memoli. Classical multidimensional scaling on metric measure spaces. *arXiv preprint arXiv:2201.09385*, 2022.

[24] Jean-Pierre Marec. Drag reduction: a major task for research. pages 17–27, 01 2001.

[25] Jeanne Methel, Maxime Forte, Olivier Vermeersch, and Grégoire Casalis. An experimental study on the effects of two-dimensional positive surface defects on the laminar–turbulent transition of a sucked boundary layer. *Experiments in Fluids*, 60:1–18, 2019.

[26] Sandile Motsa and Zodwa Makukula. On spectral relaxation method approach for steady von karman flow of a reiner-rivlin fluid with joule heating, viscous dissipation and suction/injection. *Open Physics*, 11(3):363–374, 2013.

[27] Stephen B Pope. Turbulent flows. *Measurement Science and Technology*, 12(11):2020–2021, 2001.

[28] Gregory A Reynolds and WS Saric. Experiments on the stability of the flat-plate boundary layer with suction. *AIAA journal*, 24(2):202–207, 1986.

[29] Hannah Ritchie. Climate change and flying: what share of global co2 emissions come from aviation? *Our World in Data*, 2020. https://ourworldindata.org/co2-emissions-from-aviation.

[30] Hermann Schlichting and Joseph Kestin. *Boundary layer theory*, volume 121. Springer, 1961.

[31] L-U Schrader, Luca Brandt, Catherine Mavriplis, and Dan S Henningson. Receptivity to free-stream vorticity of flow past a flat plate with elliptic leading edge. *Journal of Fluid Mechanics*, 653:245–271, 2010.

[32] Apollo Milton Olin Smith. Transition, pressure gradient and stability theory. *Douglas Aircraft Co., Report ES 26388*, 1956.

[33] Jelena Svorcan, Jonathan M Wang, and Kevin Patrick Griffin. Current state and future trends in boundary layer control on lifting surfaces. *Advances in Mechanical Engineering*, 14(7):16878132221112161, 2022.

[34] David J Tritton. *Physical fluid dynamics*. Springer Science & Business Media, 2012.

[35] J Van Ingen. The en method for transition prediction. historical review of work at tu delft. In *38th Fluid Dynamics Conference and Exhibit*, page 3830, 2008.

[36] JL Van Ingen. A suggested semi-empirical method for the calculation of the boundary layer transition region. *Technische Hogeschool Delft, Vliegtuigbouwkunde, Rapport VTH-74*, 1956.

[37] Jianzhong Wang and Jianzhong Wang. *Geometric structure of high-dimensional data*. Springer, 2012.

[38] AR Wazzan, TT Okamura, and AMO Smith. Spatial and temporal stability charts for the falkner-skan boundary-layer profiles. *REPORT NO. DAC-67086, McDonnell Douglas Astronautics Company-Huntington Beach*, 1968.

[39] Jerry Westerweel, Bendiks J Boersma, and Frans TM Nieuwstadt. *Turbulence: Introduction to Theory and Applications of Turbulent Flows*. Springer International Publishing, 2016.

[40] Xuesong Wu and Ming Dong. A local scattering theory for the effects of isolated roughness on boundary-layer instability and transition: transmission coefficient as an eigenvalue. *Journal of Fluid Mechanics*, 794:68–108, 2016.

[41] Xuesong Wu and Linda W Hogg. Acoustic radiation of tollmien–schlichting waves as they undergo rapid distortion. *Journal of Fluid Mechanics*, 550:307–347, 2006.